Max-Planck-Institut für Metallforschung
Stuttgart

Microstructural and Film Thickness Effects on the Thermomechanical Behavior of Thin Au Films

Linda Sauter

Dissertation
an der
Universität Stuttgart

Bericht Nr. 195
November 2006

Microstructural and Film Thickness Effects on the Thermomechanical Behavior of Thin Au Films

Von der Fakultät Chemie der Universität Stuttgart
zur Erlangung der Würde eines Doktors der Naturwissenschaften
(Dr. rer. nat.) genehmigte Abhandlung

Vorgelegt von

Linda Xenia Sauter

aus Freudenstadt

Hauptberichter:	Prof. Dr. phil. Eduard Arzt
Mitberichter:	Prof. Dr. rer. nat. Gerhard Dehm
Tag der mündlichen Prüfung:	16.11.2006

Max-Planck-Institut für Metallforschung
und
Institut für Metallkunde der Universität Stuttgart
2006

“Our ancestors killed, and even destroyed entire civilizations for gold and silver – not because these metals were of any real use to them, but for their rarity and beauty. “

Stephen L. Sass
„The Substance of Civilization“,
Arcade Publishing, New York 1998

Linda Sauter

Microstructural and film thickness effects on the thermomechanical behavior of thin Au films

145 pages, 55 figures, 7 tables

Abstract

The thermomechanical behavior of thin metal films depends strongly on the film thickness, the film microstructure and the surface state. The latter becomes important at elevated temperatures, where diffusion controls the stress evolution. Au provides the unique opportunity to investigate this effect because of its chemical inertness. Au films between 57 and 1738 nm with two different microstructures: (i) typically columnar grained films with grain sizes on the order of the film thickness and (ii) atypical films with non-columnar grains exhibiting thermally stable fine grain sizes (100 to 200 nm) were sputter-deposited and examined. Thus, film thickness and grain size effects on the mechanical properties could be separated, which is normally not possible and has been hardly studied. Room temperature plasticity was accomplished by dislocation glide and, as expected, the finer grained films exhibited more hardening and higher total stresses. The smallest dimension was found to determine the strength of the material. At elevated temperatures, all films relaxed by diffusional creep. For columnar Au films, parallel glide dislocations were observed the first time by transmission electron microscopy. Consequently, the thermomechanical behavior of these films was discussed in light of constrained diffusional creep. Non-columnar films could additionally relax local compressive stresses by hillock formation. The requirements to form hillocks were analyzed with respect to the unusual microstructure. The network of interconnected horizontal grain boundaries providing for the necessary long-range diffusive material transport was found to be the major precondition.

Linda Sauter

Der Einfluss der Mikrostruktur und der Schichtdicke auf das thermomechanische Verhalten dünner Au Schichten

145 Seiten, 55 Abbildungen, 7 Tabellen

Kurzzusammenfassung

Das thermomechanische Verhalten dünner Metallschichten hängt sehr stark von der Schichtdicke, der Schichtmikrostruktur und der Oberfläche ab. Die Beschaffenheit letzterer ist vor allem für diffusionskontrollierte Verformung wichtig. Au bietet die einzigartige Möglichkeit dies zu untersuchten, da es chemisch inert ist. Au Schichten zwischen 57 und 1738 nm wurden mit zwei verschiedenen Mikrostrukturen hergestellt: (i) typische, kolumnare Schichten, deren Korngröße ungefähr der Schichtdicke entsprach und (ii) untypische, nicht kolumnare Schichten, deren kleine Körner (100 bis 200 nm) thermisch stabil waren. Die Schichtdicken- und Korngrößeneffekte auf das thermomechanische Verhalten konnten somit getrennt betrachtet werden. Dies ist normalerweise nicht möglich und wurde daher auch noch kaum untersucht. Bei Raumtemperatur ist Versetzungsgleiten der dominierende Verformungsmechanismus. Daher zeigten die feinkörnigen Schichten wie erwartet mehr Verfestigung und höhere Spannungen. Es konnte außerdem gezeigt werden, dass die kleinste Dimension festigkeitsbestimmend ist Bei höheren Temperaturen haben sich allen Schichten durch Diffusionskriechen verformt. Im Falle kolumnarer Au Schichten konnten erstmals parallele Gleitversetzungen im Transmissionselektronenmikroskop gefunden werden. Folglich wurde das thermomechanische Verhalten dieser Schichten mit Hinblick auf eingeengtes Diffusionskriechen diskutiert. In den nicht kolumnaren Schichten wurden die Spannungen zusätzlich lokal durch Hügelbildung relaxiert. Die Voraussetzungen für Hügelbildung wurden unter Einbeziehung der ungewöhnlichen Mikrostruktur diskutiert. Ein Netzwerk horizontaler Korngrenzen parallel zur Schichtebene war die wesentliche Voraussetzung für weit reichenden Materialtransport.

Danksagung

Die Arbeit wurde zwischen Juli 2003 und August 2006 in der Abteilung von Prof. Arzt am Max-Planck-Institut für Metallforschung und dem Institut für Metallkunde der Universität Stuttgart angefertigt. Der International Max Planck Research School for Advanced Materials danke ich dabei für die finanzielle Unterstützung.

Herrn Prof. Arzt danke ich für die Möglichkeit diese Arbeit in seiner Abteilung durchzuführen, sowie für wertvolle Anregung und Diskussionen.

Vielen Dank an Herrn Prof. Gerhard Dehm für die Übernahme des Mitberichts, sowie für seine stete Gesprächsbereitschaft und viele hilfreiche Kommentare.

Herrn Prof. John Balk danke ich für die anfängliche Betreuung der Arbeit, aber auch dass er nach seinem Weggang aus Stuttgart immer für Fragen zur Verfügung stand. Frau Dr. Julie Nucci möchte ich herzlich danken, dass sie die Arbeit in der letzten Phase mit sehr viel Engagement betreut hat.

Ohne verschiedene Serviceeinrichtungen und Techniker wäre diese Arbeit nicht möglich gewesen: Herzlichen Dank an das Dünnschichtlabor für die Herstellung der Goldschichten, dem Zentrum für Elektronenmikroskopie, dass ich die Transmissionselektronenmikroskope benutzen durfte und der ZWE „Röntgenbeugung.“ Natascha Sauer stand mir bei Fragen der TEM Präparation immer mit Rat und Tat zur Seite.

Bei mathematischen Fragen und den Simulationen hat mich mein Bruder Martin unterstützen. Vielen Dank.

Allen Kollegen in der Abteilung Arzt danke ich für die angenehme Arbeitsatmosphäre, sowie interessante und bereichernde Diskussionen.

Allen Freunden und Bekannten, die mich in den letzten drei Jahren immer wieder ermutigt haben, gilt mein herzlicher Dank.

Meinen Eltern danke ich, dass sie mich während meines Studiums und der Promotion in jeglicher Hinsicht immer unterstützt haben.

Table of Contents

1 Introduction 13
2 Literature review and motivation 15
2.1 Dislocation plasticity in thin metal films 15
2.2 Diffusion in thin films 19
2.2.1 Constrained diffusional creep 20
2.2.2 Surface evolution due to diffusive processes 24
2.3 Mechanical and thermomechanical behavior of Au in small dimensions 26
2.3.1 Films on substrates 26
2.3.2 Free-standing Au films 29
2.3.3 Gold pillars 30
2.3.4 Hillock formation in Au films 31
2.4 Summary of the literature and motivation 32
3 The thermomechanical behavior of Au films with different microstructures 35
3.1 Introduction 35
3.2 Experimental 36
3.2.1 Film deposition and characterization 36
3.2.2 Stress-temperature measurements 39
3.3 Results 40
3.3.1 Film characterization 40
3.3.1.1 Films sputtered at 300 °C 40
3.3.1.2 Films sputtered at ambient temperatures 43
3.3.1.3 Summary of the different types of films 46
3.3.2 Stress-temperature behavior 48
3.3.2.1 Stress-temperature behavior of non-columnar films (type NC) 49
3.3.2.2 Stress-temperature behavior of columnar films (type CH) 50
3.3.2.3 Stress-temperature behavior of the ultra-thin columnar films (type CL) 52
3.3.2.4 Stress relaxation at 500 °C 53
3.3.2.5 Summary of the stress-temperature experiments 54
3.3.3 Stress at 50 °C 56
3.3.4 TEM observations 58
3.4 Discussion 60

3.4.1 Stress-temperature behavior 60
3.4.1.1 Constrained diffusional creep in thin columnar Au films 60
3.4.1.2 Stress-temperature behavior of non-columnar Au films 69
3.4.1.3 Comparison the stress-temperature behavior of other metal films 70
3.4.2 Stresses at 50 °C as function of film thickness and grain size 70
3.4.3 Comparison to other studies of Au in small dimensions....73
3.5 Summary and Conclusion 74
4 Hillock formation in non-columnar Au films 77
4.1 Introduction 77
4.2 Film deposition and methods 78
4.3 Au microstructure and thermal stresses 80
4.3.1 Film microstructure 80
4.3.2 Stress-temperature behavior....83
4.4 Hillocks 86
4.4.1 Hillock microstructure....88
4.4.2 Hillocks statistics....90
4.4.3 Hillock growth during thermal cycling 94
4.4.4 Hillock growth during isothermal annealing....94
4.5 Discussion of hillock formation 97
4.5.1 Hillock formation mechanisms 97
4.5.2 Hillocks and stress....100
4.6 Summary and Conclusion 104
5 Summary 105
6 Appendix 109
6.1 Film thickness 109
6.2 Texture 111
6.3 Stress-temperature measurements 111
6.3.1 Experimental error of the wafer curvature measurements 111
6.3.2 Stress-temperature curves 115
6.3.2.1 Stress-temperature curves of type CH....115
6.3.2.2 Stress-temperature curves of type NC....119
6.3.2.3 Stress-temperature curves of type CL 126
7 Deutsche Zusammenfassung 131
8 References 141

Symbols

b	Burgers vector [nm]
d	grain size [nm]
D_s	surface diffusivity [m^2/s]
E	Young's modulus [GPa]
G_f	shear modulus of the film [GPa]
G_s	shear modulus of the substrate [GPa]
h_f	film thickness [nm]
k	Boltzmann constant [eV/K]
M_{111}	biaxial module for a (111)-fiber textured film [GPa]
N_{disl}	number of dislocations [-]
R	correlation factor of a least square fit/ linear regression [-]
s	Schmid factor
S	surface area [µm^2]
s_d	size of a dislocation source [nm]
T	absolute temperature [K]
t	time [min]
t_0	characteristic time [min]
V_{hill}	hillock volume [µm^3]
W_{gb}	energy of a misfit dislocation segment at the grain boundary [J]
W_i	energy of a misfit dislocation segment at the interface [J]
α	coefficient of thermal expansion [K^{-1}]
	also: numerical constant (in the source model)
β_1, β_1	numerical constant that describes the cutoff radius of a dislocation [-]
γ_b	grain boundary energy [mJ/m^2]
γ_s	surface energy [mJ/m^2]
δD_{gb}	grain boundary diffusivity [m^3/s]
$\dot{\varepsilon}$	strain rate [s^{-1}]
ε_{th}	thermal strain [-]
λ	angle between the normal vector of the sample and the Burgers vector [°]

	also: geometrical constant
ν_f	Poisson's ratio of the film [-]
ρ_{disl}	dislocation density [m^{-2}]
ρ_{hill}	areal hillock density [$1/\mu m^2$]
σ_0	intragranular stress [MPa]
σ_f	stress in the film [MPa]
σ_{gb}	grain boundary traction [MPa]
σ_y	flow stress [MPa]
τ_s	shear stress to activate a dislocation source
ϕ	angle between the normal vector of the sample and the glide plane [°]
Ω	atomic volume [$Å^3$]

1 Introduction

The rapid development in microelectromechanical systems (MEMS) brings new challenges for material science, because a wide range and combination of materials is already and will be used in the future in small dimensions. A review on “Materials issues in MEMS“ [1], published in 2000, named the understanding of size-effects a major issue for the success of the MEMS technology. Thin metal films, e.g. exhibit extraordinarily high strengths, which even increase further with decreasing thicknesses [2]. This can have negative and positive implications for device performance and reliability. On the one hand, processing often involves several heat treatment steps at various temperatures, which can result in substantial thermal stresses in thin metal films caused by the different thermal expansion coefficients of different materials. These stresses may relax by creep during device operation and ultimately affect device performance. As a further consequence of the heat treatment, the film surface may be altered by diffusional processes, which can lead to increased roughness via material protrusion or void formation. On the other hand, the capability of sustaining large stresses can be exploited for force transmission. To improve the processing and reliability and/or to tailor the performance of MEMS devices, it is crucial to understand the fundamental mechanisms of thin film mechanics. Material selection, design and processing can then be chosen adequately.

For many MEMS applications gold is a very advantageous material. It is an excellent electrical conductor, has a high reflectivity for visible light, which is important for optical devices, and it is chemically inert to most etch solutions used during processing. Lastly, its biocompatibility provides a key advantage in the fast evolving field of BioMEMS [3]. Besides its technological applications, Au is also an excellent material from the view point of basic research because of its noble character. Since it is inert to reactions with the surrounding atmosphere even at elevated temperatures, it is ideally suited for studying temperature dependent mechanical properties, such as creep and surface morphology evolution.

Motivated by semiconductor interconnects, many Al and Cu thin film studies were performed over the past 15 years and significantly higher strength was found than for bulk material, e.g. [4-7]. Generally, the extraordinarily high strength and its increase with decreasing film thickness were attributed to constraints in dislocation motion. For

single-crystalline films it is the finite film thicknesses [8], while for polycrystalline films, the grain size [9] is an additional constraint. Dislocation nucleation was also discussed to be plasticity-limiting [10]. In recent years, the attention was also drawn to the impact of surface and grain boundary diffusion on stress relaxation at elevated temperatures. This was particularly triggered by the rigorous theoretical analysis of Gao *et al.* [11]. Subsequent experiments in Cu [4, 12] provided substantial evidence for the proposed mechanism that grain boundary stresses are relaxed by diffusion of material into or out of the grain boundaries in response to tensile or compressive stresses, respectively.

Au was chosen for this study, since the results of Al and Cu showed that the surface state can severely affect thin film plasticity. The noble character of Au guarantees a bare surface even at elevated temperatures in an ambient atmosphere. The thermomechanical behavior of thin Au films on Si substrates was studied by wafer curvature measurements. The first main topic explores the influence of microstructural parameters on stress evolution at room temperature, where plasticity is mediated by dislocations, and at elevated temperatures, where diffusive behavior dominates. After the literature review in chapter 2, the results of the stress-temperature behavior of films with different microstructures and the same film thicknesses is presented in chapter 3, as well as the stress as a function of film thickness. The second main topic examines the evolution of the film surface morphology during thermal cycling. Possible reasons and mechanisms for hillock formation under compressive stress conditions are discussed in chapter 4. Lastly, chapter 5 summarizes this study on diffusion and dislocation plasticity in thin Au films.

2 Literature review and motivation

The outstanding mechanical properties of thin metal films on substrates have been studied for various materials [13, 14] over the past 15 years. Compared to their bulk counterparts, thin metal films exhibit remarkably high flow stresses. The experimental results were explained by different models which are reviewed in this chapter. Furthermore, during thermal cycling diffusion at elevated temperatures plays an important role. Stresses were found to relax by creep and/or the surface morphology changed.

2.1 Dislocation plasticity in thin metal films

Inspired by experimental observations of increasing film strength with decreasing dimension, i.e. film thickness and/or grain size [6, 7], analytical models and simulations were developed to explain the observed behavior. They will be reviewed in this section and compared with experimental results. Dislocation motion in a thin single-crystalline film is confined by the finite film thickness. For polycrystalline films, the small grain sizes that are typically on the order of the film thickness are an additional barrier to dislocation motion. The idea of a lack of mobile dislocations is also considered as a mechanism to explain the increased stresses sustained by thin metal films.

Nix [8] and Freund [15] worked out an analytical expression for a threading dislocation moving through a single-crystalline film on a substrate. The threading dislocation has to deposit a misfit segment at the film/substrate interface which exacts an energetic cost (Fig. 2.1).

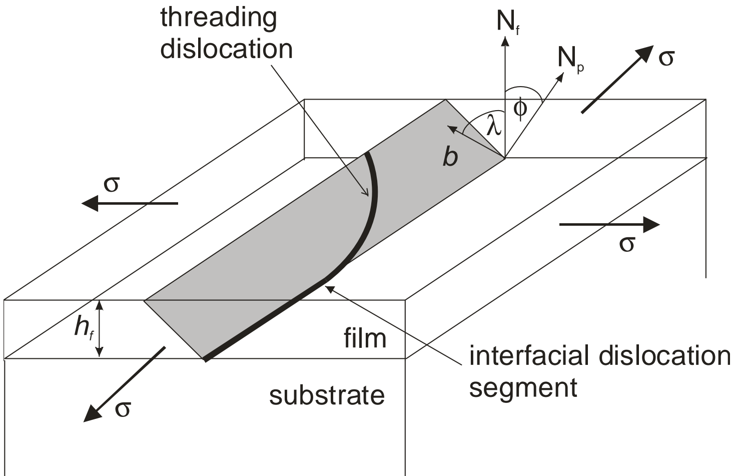

Fig. 2.1: A threading dislocation in a thin film on a substrate. A misfit dislocation segment is deposited at the film/substrate interface when the dislocation moves on an inclined glide plane due to the biaxial stress state σ of the film. ϕ denotes the angle between the glide plane normal, N_p, and the film normal, N_f, and λ is the angle between the Burgers vector, b, and the film normal, N_f, modified after [8].

An energy balance dictates that the work done by the external stress field must be equivalent to the line energy stored in the misfit dislocation segment. Thus the yield stress is expected to be:

$$\sigma_y^{Nix/Freund} = \frac{\sin\phi}{\cos\phi\cos\lambda}\frac{b}{h_f}\frac{G_f}{2\pi(1-\nu_f)}\left[\frac{G_s}{G_f+G_s}\ln\left(\frac{\beta_1 h_f}{b}\right)\right] \qquad (2.1)$$

where ϕ and λ are the angles between the normal vector of the sample and the glide plane, and between the normal vector of the sample and the Burgers vector, b, respectively, G_f is the shear modulus of the film and G_s the shear modulus of the substrate. ν_f is the Poisson's ratio of the film. β_1 is a numerical constant that prescribes the outer cut-off radius of the dislocation. An important impact of this prediction is that the flow stress increases with the reciprocal of the film thickness as a first approximation.

Stress-temperature measurements of thin epitaxial Al and Cu films on single-crystalline Al_2O_3 substrates revealed flow stresses predicted by the Nix-Freund model [5]. *In situ* transmission electron microscopy (TEM) of these Cu [5, 16] and Al [17, 18] films further supported the model, because threading dislocations with misfit segments

at the heteroepitaxial interface were observed. Polycrystalline Al and Cu films on Si with amorphous SiO_x and SiN_x interlayers and polycrystalline Cu on Al_2O_3, however, exhibit significantly larger stresses than predicted by the Nix-Freund model, but still follow the trend of higher stresses for thinner films. *In situ* TEM showed that the film/substrate interface observed during thermal cycling acted as a dislocation sink and no stable misfit segments were found [5, 19]. Grain boundaries were also found to emit and absorb dislocations.

To account for the grain boundaries as obstacles to dislocation motion in the film, Thompson [9, 20] extended the Nix-Freund model by adding misfit segments at the grain boundaries (Fig. 2.2) and a grain size term to the expression of the flow stress for thin films.

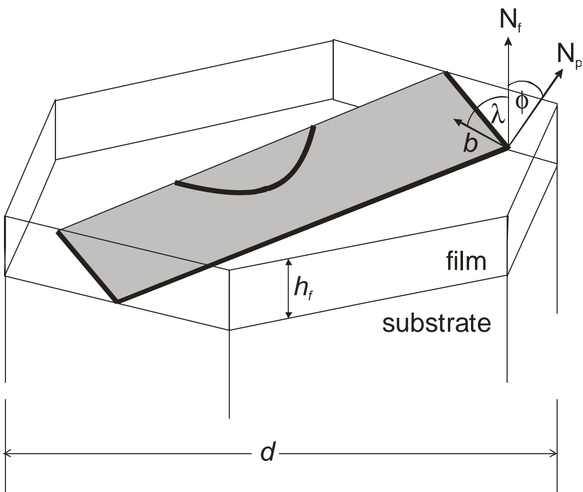

Fig. 2.2: Schematic of a dislocation moving through a grain with misfit segments deposited at the grain boundaries and the film/substrate interface. ϕ denotes the angle between the glide plane normal, N_p, and the film normal, N_f, and λ is the angle between the Burgers vector, *b,* and the film normal, N_f, modified after [20].

Consequently, the flow stress of the film does not only increase with decreasing film thickness, but also with decreasing grain size according to the following equation:

$$\sigma_y^{Thompson} = \frac{\sin\phi}{b\cos\phi\cos\lambda}\left(\frac{2W_{gb}}{d\sin\phi} + \frac{W_i}{h_f}\right) \tag{2.2}$$

in which d is the grain size, W_i is the energy of the misfit dislocation at the film/substrate interface:

$$W_i = \frac{b^2}{4\pi(1-\nu_f)} \cdot \frac{G_f G_s}{G_f + G_s} \cdot \ln\left(\frac{\beta_1 h_f}{b}\right) \tag{2.3}$$

This term is identical to the one used in the Nix-model. W_{gb} is the additional energy for misfit dislocation segments at the grain boundary given by:

$$W_{gb} = \frac{b^2 G_f}{4\pi(1-\nu_f)} \ln\left(\frac{\beta_2 d}{b}\right) \tag{2.4}$$

β_2 is a constant describing the outer cut-off radius of the dislocation at the grain boundary.

Flow stresses of polycrystalline Al films were reported to follow this behavior [7], i.e. the film thickness and the grain size contribution add. An analysis of polycrystalline Cu films favored a Hall-Petch type dependence, where the flow stress is proportional to the inverse square root of the grain size [6].

For the Cu films mentioned above [6], film thickness and grain size contributions were still too low to satisfactorily model the experimental results. Dislocation interactions, which were included to obtain quantitative agreement with the experimental stress value, were also analyzed theoretically by Nix [21], and simulated by Schwarz and Tersoff [22] and by Pant *et al.* [23]. Nix considered interactions between advancing threading dislocations and obstacle dislocations (e.g. misfit dislocations). The interaction of an advancing threading dislocation with one misfit obstacle dislocation increased the flow stress by a factor of 2.6 for a film thickness of 1 µm. The nature of the dislocation interaction (attractive or repulse) was, however, not taken into account and all dislocation interactions were considered repulsive and thus this analysis gives an upper limit. Discrete dislocation dynamics simulations of dislocation interactions [22, 23] yielded smaller stress increases, and pointed out that a full 3-D simulation is necessary to describe thin film behavior. Furthermore, since TEM observations of polycrystalline thin Cu films revealed decreasing dislocation density with decreasing film thickness [5], strain hardening does not seem to be responsible for the higher flow stresses at small film thicknesses. These observations and considerations lead to a third approach to explain the increase in flow stress with decreasing film thickness. The critical parameter was not considered to be dislocation

motion, but dislocation generation. Von Blanckenhagen simulated thin film plasticity with respect to the activation of dislocation sources [10, 24], using an Orowan equation to relate the shear stress and the size of the dislocation source :

$$\tau_s = \frac{G_f b}{2\pi} \cdot \frac{1}{s_d} \ln\left(\frac{\alpha s_d}{b}\right) \tag{2.5}$$

where α a numerical constant and s_d the size of the dislocation source. The source configuration was chosen such that the activation energy was minimized [10]. A dislocation source was found to be most active if its size comprises one third of the film thickness h_f or grain size d, whichever is smaller. By locating the source in the middle of the grain, the back stress of previously deposited dislocations upon multiple operation of the source was minimized. For $d > h_f$ the yield stress of a films was given by dividing by the Schmid factor, s:

$$\sigma_y^{source} = \frac{1}{s} \cdot \frac{3G_f b}{2\pi} \cdot \frac{1}{h_f} \ln\left(\frac{\alpha h_f}{3b}\right) \tag{2.6}$$

As seen from equation (2.6), the stress in the source model (as it will be called in the following) also depends on $(\ln h_f)/h_f$ like the Nix-Freund model. However, the absolute stress values are larger. By employing the source model, the stress in thin polycrystalline Cu films can be reproduced reasonably well for films thicker than 400 nm [25]. As will be discussed later, below this film thickness, the stress becomes independent of film thickness [4], which is probably due to a change in deformation mechanism.

2.2 Diffusion in thin films

In addition to being barriers for dislocation motion, the high volume fraction of the interfaces, and the grain boundaries and also the surface provide many fast diffusion pathways in thin films as compared to bulk materials. This, of course, will affect mechanical properties at elevated temperatures and the evolution of surface morphology. In the following, mechanisms for stress relaxation by diffusional creep and for void and hillock formation will be reviewed.

2.2.1 Constrained diffusional creep

The availability of fast diffusion pathways is essential for stress relaxation by diffusional creep mechanisms. For bulk materials, stress relaxation at elevated temperatures often involves grain boundary diffusion such as for Coble creep [26]. For thin polycrystalline films on substrates, surface and interfacial diffusion must be taken into account as well because of the large surface to volume ratio. The diffusion constants and activation energies for surface and the interface diffusion are different, which has a major impact on the stress relaxation. Gao *et al.* [11] treated this scenario theoretically by not allowing interfacial diffusion or sliding, in contrast to previous analyses [27-29]. In the Gao model, the surface and the grain boundaries are considered major diffusive pathways, i.e. a free surface is an essential precondition for this analysis. For a film under tensile stress at elevated temperature, atoms diffuse from the surface into the grain boundaries, where they accumulate and form a wedge to locally relax the tensile stresses. This configuration is thought be equivalent to the insertion of an array of climb edge dislocation into the grain boundary. The stress singularity at the wedge tip was treated as a mode I crack tip. Hence, shear stresses act also on planes parallel to the film/substrate interface, while for a homogenous biaxial stress state these planes are free of shear stresses. Indeed, Balk *et al.* [4] frequently observed dislocation motion in Cu films thinner than 400 nm on (111) lattice planes parallel to the substrate during *in situ* thermal cycling in the TEM. Fig. 2.3 shows these parallel glide dislocations in a 200 nm thick Cu film after thermal cycling.

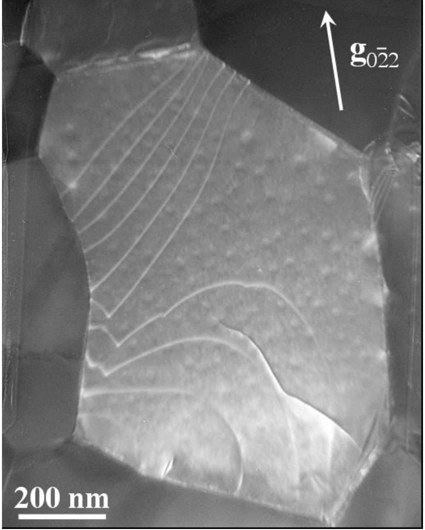

Fig. 2.3: Parallel glide dislocations in a (111)-oriented grain in a 200 nm thick Cu film [4]. Figure by courtesy of J. T. Balk.

Parallel glide dislocations accounted for most of the plastic deformation in ultra-thin films, while the number of threading dislocations observed decreases with decreasing film thickness. This was attributed to the fact that the activation of threading dislocation sources required higher stresses for thinner films [10]. Finally the activation energy became too high for threading dislocations to move in the ultra-thin films [4].

To simulate stress-temperature curves for unpassivated Cu films, Weiss [12] incorporated an expression by Xia and Hutchinson [30] for a periodic array of cracks into the theoretical calculations and obtained the following expression for the average stress σ_f in the film:

$$\sigma_f = \sigma_0 - (\sigma_0 - \sigma_{gb})\left(\frac{4h_f}{d}\tanh\left[\frac{d}{4h_f}\right]\right) \tag{2.7}$$

where σ_0 is the intragranular stress. The grain boundary traction σ_{gb} is [12]:

$$\sigma_{gb}(t) = \sigma_0 \exp\left(-\frac{\lambda t}{t_0}\right) \tag{2.8}$$

where t_o is a characteristic time. λ is a geometry-dependent parameter involving the aspect ratio [12]:

$$\lambda = 8.10 + 30.65\frac{h_f}{d} \tag{2.9}$$

The characteristic time is [12]:

$$t_0 = \frac{4\pi(1-\nu_f^2)kTh_f^3}{E_f \Omega \delta D_{gb}} \tag{2.10}$$

where ν_f is the Poisson's ratio of the film, E_f is the Young's modulus of the film, Ω is the atomic volume, δD_{gb} is the grain boundary diffusivity, T is the temperature and k is Boltzmann's constant.

Equations (2.8) to (2.10) state that the grain boundary traction in thinner films relaxes faster. However, for the final film stress, when the grain boundaries are totally relaxed, it is obvious from equation (2.7) that neither the film thickness nor the grain size alone, but rather the ratio of grain size to film thickness, determine the final film

stress. Films with large d/h_f ratio will exhibit stresses that are closer to the intragranular stress values, whereas films with small ratios will have lower stress values, since the grain boundary stress relaxed by constrained diffusional creep, is a larger portion of the total film stress. Considering stress-temperature behavior, this means that films with the same aspect ratio, but thinner

When modeling the experimental stress-temperature curves of Cu at elevated temperatures, it was necessary to also include thermally activated dislocation glide for the relaxation of the intragranular stress [12]. As an example, the stress-temperature measurement for a 500 nm thick Cu film (open circles) is shown in Fig. 2.4 together with simulations for the grain boundary traction (dotted line), thermally activated dislocation glide (dashed line), and the simulation including both constrained diffusional creep and thermally activated dislocation glide (solid line) [12]. The stress-drop around 250 °C during the first heating cycle is characteristic for constrained diffusional creep. Note that the value for the grain size in the simulation is a factor of three larger than the experimentally measured grain size. It was argued [12] that low angle grain boundaries might not be relaxed, because their diffusion coefficients are expected to be lower. This can also be considered as a larger effective grain size.

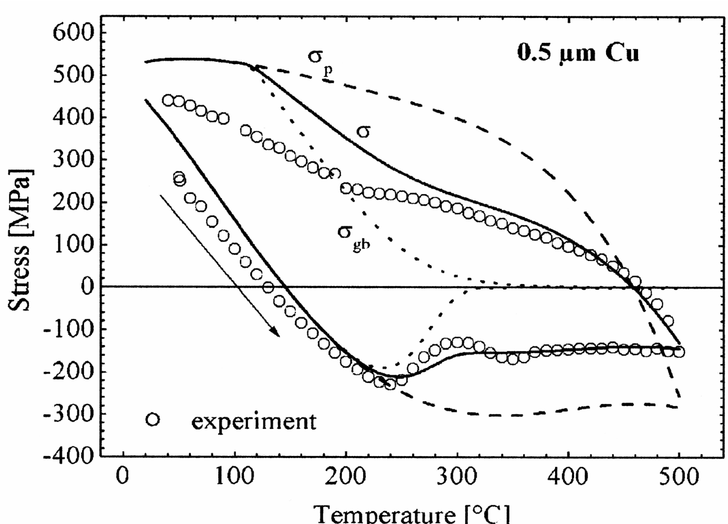

Fig. 2.4: A simulation (solid line) of the experimentally measured stress-temperature behavior (open circles) for a 500 nm thick Cu film, which considers both constrained diffusional creep (dotted line) and thermally activated dislocation glide (dashed line) provides a good fit for the experimental data [12]. Used with permission from Elsevier [31].

A different approach to better reproduce the behavior at elevated temperatures was the inclusion of a threshold stress by Bühler *et al.* [32]. This was in turn motivated by discrete dislocation dynamics simulation, which associated the onset of constrained diffusional creep with the nucleation of a climb dislocation in the grain boundary. The comparison of the model with the experiment can be seen in Fig. 2.5 for a 600 nm thick Cu film. Above 620 K during heating and thermoelastic unloading during cooling can be reproduced with this model. At lower temperatures, however, it fails to predict the experimental observations. Here, consideration of thermally activated dislocation glide by Weiss [12] yields better agreement.

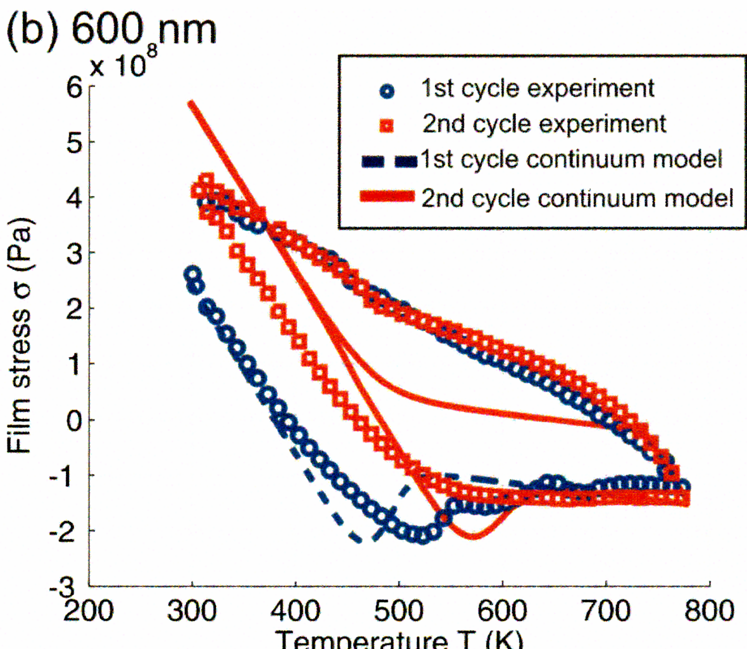

Fig. 2.5: Experimental and simulated stress-temperature curves for a 600 nm thick Cu film. For the simulation constrained diffusional creep with a threshold stress was applied [33] Figure created by M. Bühler and used with permission from the Materials Research Society.

If surface diffusion is hindered by a passivation layer, which can be a native oxide as for Al or a very thin film deposited on top of the metal layer, then no constrained diffusional creep is expected. Stress-temperature curves of self-passivated Cu- 1at.% Al [34] could be modeled by simply assuming thermally activated dislocation glide. Au films that were passivated with silicone nitride also showed a different stress-temperature behavior than bare Au films [35] and their behavior could also be explained exclusively by dislocation glide processes.

2.2.2 Surface evolution due to diffusive processes

The mechanical properties of thin metal films on substrates are often measured by thermal cycling. At elevated temperatures the surface morphologies of the films can be altered by diffusional processes. The most prominent, namely grain boundary grooving, void and hillock formation, are presented in the following.

Grain boundary grooving is a well studied phenomenon that was first analytically described by Mullins in 1957 [36]. For thin films with columnar grains, the maximum grain size for normal grain growth is limited by the radius of curvature that the grain boundary groove can exhibit. The exact value depends on the ratio of grain boundary to surface energy, but for thin films once to twice the film thickness is expected, according to the following equation [37]:

$$d_{\max} = \frac{3\gamma_s}{m\gamma_b} \cdot h_f \qquad (2.11)$$

where γ_s is the surface energy, γ_b is the grain boundary energy, m is a constant (~5). The resulting maximum grain size for thin films is usually 1 to 2 times the film thickness [4, 7, 12, 38, 39].

The surface morphology for thin films on substrates at elevated temperature can change beyond grain growth and grain boundary grooving, when the film is subjected to high stresses due to different thermal expansion coefficients of the metal film and the substrate. Tensile stresses can be relaxed by void and hole formation and compressive stresses by hillock formation. These phenomena were theoretically analyzed [29, 40, 41] and experimentally observed [42-47]. Génin [28, 29, 48] conducted a comprehensive theoretical study of the surface evolution at triple junctions and grain boundaries. In his analysis, grain boundary diffusion was assumed to be the most important material transport mechanism. Some additional assumptions were made: large grains, which is equivalent to the absence of long-range interactions, isotropy, no volume diffusion and small surface slopes. Initially, grain growth was not allowed [29], but later the model was extended to allow grain boundary motion [28, 48]. Pits were expected at triple junctions, from where they grow along grain boundaries resulting in grain boundary voids. The distribution of voids or grain boundary pits will most likely be non-uniform, because their formation depends on grain boundary diffusivities which in turn depend on the grain boundary energy and the grain boundary angle. Studies in Cu showed that void formation critically depends on the grain boundary orientations.

Nucci *et al.* [49] could relate high angle grain boundaries to voids in passivated Cu lines. Weiss [50] found a similar behavior for self-passivated Cu-1at% Al films. Park [51] extended the experiments to Cu films with different grain sizes and found that larger grains exhibited less grain boundary voiding and that grain boundary orientation controlled whether grooves or triple junction voids formed.

For hillock formation, the microstructure, especially the grain boundary orientation and triple junctions, also played an important role as observed in post-mortem TEM investigations of hillocks in Al films [44, 46]. For Al it was also shown that a stronger (111)-texture leads to fewer hillocks than a weaker texture [45].

Many different approaches were made to explain experimental observations of hillock formation. All considered hillock formation as the predominant compressive stress relaxation mechanism at elevated temperatures [44, 52-54]. However, the mechanisms for hillock nucleation and growth are controversial. Chaudhari [40] developed a model starting from experimental observations in Sn and Pb films that assumed that atoms diffuse along the film/substrate interface from regions of higher stress to regions that have been locally relaxed, e.g. by dislocation slip or twinning. The atoms accumulate such that the hillocks grow out of the film with new material being provided to the base of the hillocks by interfacial diffusion. Hence, hillock formation requires large diffusion distances along the film/substrate interface. Stress relaxation by creep, however, would be much faster due to the shorter diffusion paths. Chaudhari [40] conjectures that creep is suppressed in favor of hillock formation, if grain boundary diffusion coefficients are smaller than interfacial diffusion coefficients. However, annealing experiments of Al films showed two regimes of stress relaxation [47]: First, the stresses decreased rapidly with time and no hillocks were formed, and second a slower relaxation occurred and hillock formation could be observed. The reasons for this transition still remain unclear, since it seems very unlikely that grain boundary diffusivity changes with time. Furthermore, no thorough microstructural analysis with respect to the grain boundary orientations, which may shed some more light on the diffusivities, was conducted in this study. Other experiments of fine-grained Al films [53] showed that hillocks form at the film/substrate interface, as predicted by Chaudhari [40]. Results for Al films with larger grains [43], on the other hand could be described using Génin's extended model [48] in which grain boundary motion is allowed. Grain growth is equivalent to the inclusion of long-range material transport by the moving grain boundaries. Lateral diffusion in fine-grained films was also proposed [55] as

mechanism. A further mechanism to incorporate long-range material transport would be plastic deformation by dislocation motion [41]. Hillocks form by diffusion of atoms from the grain boundary to the surface and hence the stress at the grain boundary is relaxed, while the stress in the grain interior can only be relaxed by plastic deformation, i.e. dislocation motion, which then brings new atoms to the grain boundary. As a fourth mechanism, grain boundary sliding is assumed to provide for material for hillock growth [40, 52].

The different explanations for void and hillock formation show that the underlying mechanisms seem to be very complex and thus are not fully identified. However, it is agreed that voids and hillocks form to relax tensile or compressive stresses at elevated temperatures, respectively, and that diffusive processes play a crucial role. The nature of the primary or limiting diffusion mechanism (interfacial, grain boundary or surface diffusion) differs in the various models and material systems studied. The need for long-range material transport was emphasized, but again it is controversial how it is achieved ranging from interfacial sliding [40, 52], to dislocation plasticity [41], or diffusion along lateral grain boundaries [55], or grain boundary motion [28, 43]. The interplay between relaxation by diffusional creep and hillock formation is also not resolved [40].

2.3 Mechanical and thermomechanical behavior of Au in small dimensions

In recent years, increasing attention has been drawn to the mechanical behavior of Au in small dimensions. Au provides several advantages, since it does not oxidize and serves as a model system for a free surface. Due to its noble character it is also resistant to many chemicals; this becomes important for more elaborate sample preparation and testing involving MEMS technologies. This section reports on the literature of Au films on substrate and free-standing films and additionally on compression tests of nano-sized single-crystalline Au pillars.

2.3.1 Films on substrates

Studies of thin Au films on substrates were conducted employing different experimental techniques, e.g. wafer curvature method [35], micro-tensile testing [32], nanoindentation [56] and TEM [57, 58].

The thermomechanical behavior of unpassivated and passivated thin polycrystalline Au films on silicon with a 10 nm W or Ti adhesion layer was investigated during thermal cycling by Leung *et al.* [38]. Fig. 2.6 shows the stress-temperature behavior of a passivated and an unpassivated 500 nm thick Au film. The curves differ significantly at elevated temperatures.

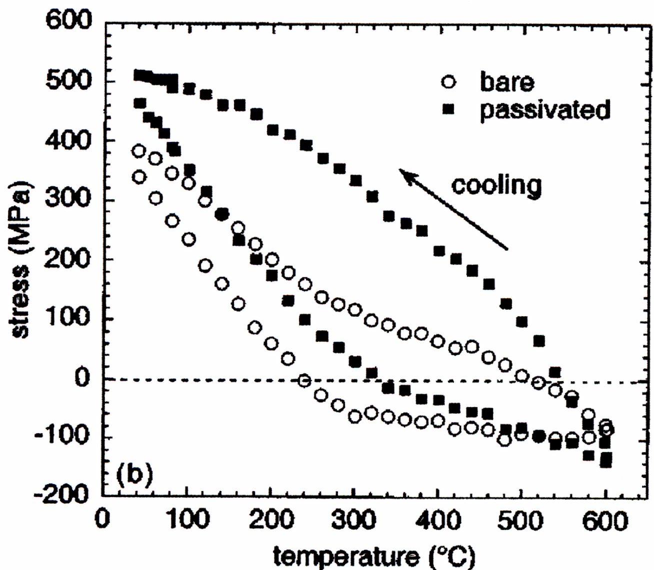

Fig. 2.6: Thermal cycles of passivated and unpassivated 500 nm thick Au films [38]. The passivated film exhibits the larger hysteresis, which can be explained by kinematic hardening of dislocation glide. In the unpassivated film, constrained diffusional creep is thought be active. Reprinted with permission from AIP [59].

In their work, Leung *et al.* could model the curve for the passivated film by using kinematic hardening of dislocations. For unpassivated films, constrained diffusional creep was assumed to be active due to the free surface, but the experimental curves could not be reproduced. However, unpassivated films thicker than 1 µm exhibit the same stress-temperature behavior as passivated films. This led to the conclusion that a mechanism change from creep to only dislocation glide occurs between 1 and 2.5µm. If the stresses at room temperature are plotted vs. the inverse film thickness as shown in Fig. 2.7, a deviation from the linear behavior is found only below about 500 nm [35, 38]. The reasons for this were not further discussed. Nonetheless, a transition from dislocation- to diffusion-dominated plasticity, however, is also reported in TEM investigations of Cu films [4]. At a transition state both mechanisms are perhaps equally active.

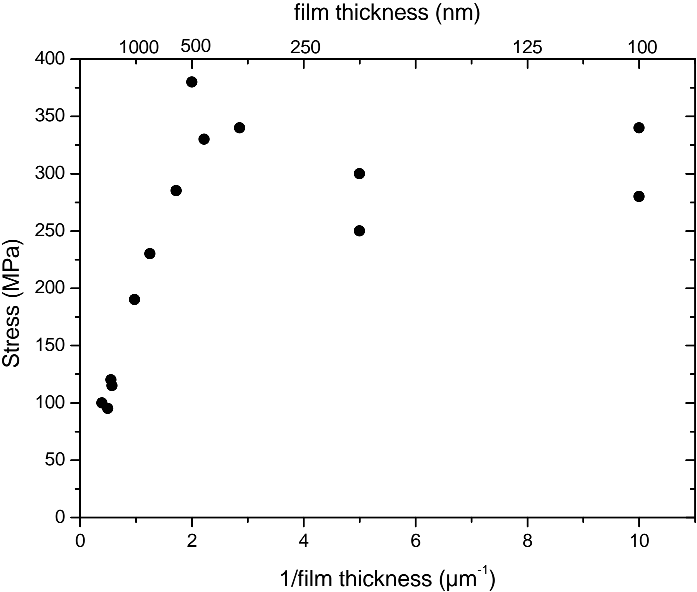

Fig. 2.7: Flow stress vs. inverse film thickness for Au films on Si with 10 nm W or T interlayer [38]. At about 500 nm the stress dependence on the inverse film thickness changes from linear to a plateau indicating a change in primary deformation mechanism.

Legros *et al.* [57] investigated the samples of Leung *et al.* using cross-sectional TEM. It was shown that the Au films contain many twins parallel to the film/substrate interface, which may also be an obstacle for moving dislocations. Since this was not considered in the analysis of the stress temperature measurements by Leung *et al.* [35], the effective thickness for dislocations may be smaller than the film thickness. Furthermore, the contribution of the interlayer to the measured curvature is not discussed. Especially for thinner Au films, this could be significant, since the stresses in the interlayer are not known.

Tensile tests of very fine-grained Au films on polyimide substrates did not show any dependence of flow stress on film thickness [32] indicating that the fine Au grains determined the onset of plasticity.

Nanoidentation, a further well-established technique, which allows measuring thin film properties locally, was employed to examine coarse-grained and fine-grained Au films on Si and silica by Lilleodden and Nix [56]. The coarse-grained films were indented in the grain interior and near the grain boundaries. Load-displacement from the

grain boundary region showed pop-ins at lower loads than the grain interior. Pop-ins are associated with the onset of dislocation motion by dislocation emission and the grain boundaries were thought to acted as dislocation sources. The finer grains were softer during initial indentation. This counterintuitive fact was explained by the larger number of grain boundaries and consequently the larger number of potential dislocation sources. If, however, several grains in the fine-grained films were indented simultaneously, hardening was observed. Overall, the explanations of these experimental results also point to dislocation nucleation as critical parameter for the flow stress of thin Au films

Post mortem TEM observations of Au films annealed on NaCl substrates [58] showed only a few grains containing dislocations. It was concluded that this were early stages of yielding where only few grains were plastically deformed. The presence of dislocations in a grain, interestingly, did not depend on grain orientation, film thickness or grain size, but rather on glide plane geometry. The glide plane had to intersect with a triple junction and both adjacent grain boundaries. This, however, is relatively rare and therefore, these observations can also be interpreted as pointing to dislocation source-limited plasticity.

2.3.2 Free-standing Au films

The flow stress of free-standing Au films is not expected to depend on the film thickness, because dislocations are attracted to the free surface and will run out of the films. Tensile test of free-standing Au films [60] between 0.8 and 2.1 µm where the grain sizes were about twice the film thicknesses yielded the well-known Hall-Petch behavior ($\sigma_y \propto d^{-0.5}$). If, however, the grain size was between 100 and 500 nm and always smaller than the film thicknesses (between 200 nm and 2 µm), no dependence of the flow stress on the grain size could be found anymore [61], but the stress depended on the strain rate. From these observations it was concluded that even at room temperature mechanisms involving diffusion are active. The fit of a power-law equation to the data yielded a stress exponent similar to that for the diffusion of vacancies along dislocation cores, so that it was assumed that climb of dislocations is most likely. Smaller grains provide more grain boundary area and hence more fast diffusion paths, shorter diffusion distances and more grain boundaries as potential dislocation sources and sinks. Haque and Saif [62] investigated the effect of much smaller grain sizes.

Thicker films (350 nm) with fine grains (15 nm) and thinner films (200 nm) with larger grains (75 nm) were tensile tested and compared. Note that in both cases the grain size was significantly smaller than the film thickness and especially the first sample was in the nano-crystalline regime. The very fine grains resulted in nonlinear elasticity upon unloading, whereas the films with the larger grains exhibited plasticity. From this can be concluded that no dislocation activity can occur in the very fine grains.

Membrane deflection experiments on samples with different membrane widths and membrane thicknesses by Espinosa *et al.* [63] revealed the significance of the number of grains across the film thickness and/or the membrane width. In particular, if the number of grains through the film thickness became small (e.g. 2 grains for 300 nm membrane thickness), then an increase in stress was observed. This was explained by the reduction of grain boundaries, which are potential dislocation sources.

2.3.3 Gold pillars

Uchic *et al.* [64] developed and realized the idea of cutting small pillars with a focused ion beam microscope and performing nano-compression test in 2004. This new test geometry has some advantages to conventional nanoindentation tests: No strain gradients are introduced in the specimen during testing and no impact of an underlying rigid substrate has to be taken into account. Since the pillars are single-crystalline, microstructural effects can be excluded. Following the experiments of Uchic *et al.* [64], Greer *et al.* [65, 66] and Volkert and Lilleodden [67] prepared single-crystalline Au pillars. Diameters between 180 and 8000 nm were tested and the flow stresses in both publications are amazingly similar (Fig. 2.8) and exhibit a Hall-Petch type dependence of the flow stress on the pillar diameter. Volkert and Lilleodden [67] report a power law with an exponent of -0.61. Furthermore, both research groups assumed that a lack of mobile dislocations determined the high strength of the pillars. Dislocations escape the pillar via the free surface so that no dislocation multiplication or interaction is possible and the stress to activate new dislocation sources is high.

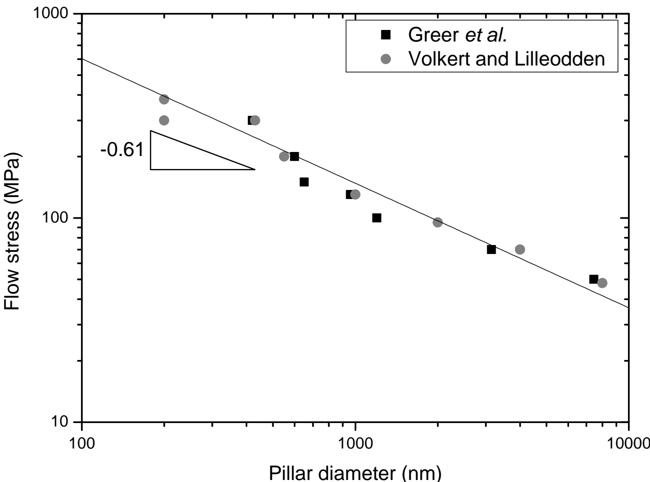

Fig. 2.8: The flow stress of single-crystalline Au pillars from nano-compression tests exhibit a power law exponent of -0.61, which is similar to the Hall-Petch coefficient. Data are taken from Greer *et al.* [65, 66] and Volkert and Lilleodden [67].

2.3.4 Hillock formation in Au films

During annealing and thermal cycling, the surface of Au films was found to undergo morphological changes including void and hillock formation. This section will mainly report on the hillock formation.

Au on silicon dioxide needs a metallic interlayer to adhere to the substrate [68, 69]. Many different metals were used as adhesion layers and their influence on the surface evolution during annealing was investigated. Kim and Hummel [69] conducted experiments with Ti, V, Cu, Sn, Ni, and In interlayers by annealing the films between 300 and 500 °C. It was found that all these metals diffused through the Au film to the surface, where they oxidized; V, Cu, Sn, Ni, and In additionally segregated at the grain boundaries, where they also partly oxidized. Using Cr as interlayer material, surface segregation was also observed by Hieber *et al*. [68] and Miller *et al.* [70] after heat treatments of 350 and 225 °C, respectively. The presence of the oxides at the surface and at the grain boundary significantly influences surface and in the grain boundary diffusion, so that hillock and void formation more closely reflects the interaction of Au with the interlayer metal rather than the properties of pure Au films. Pennebaker [54] chose Mo, which is essentially immiscible in Au to observe hillock formation dependent on the inherent properties of the in 800 nm thick Au films. These Au films were isothermally annealed at 500 °C for 24 h and hillock growth was followed with an

optical microscope when the hillock diameter exceeded 1 μm. The initial stages of hillock nucleation and growth were therefore missed, due to the limited resolution of the optical microscope. Hillocks were found to grow irregular. Not all boundary of the hillock moved with the same velocity. Pennebaker modeled the lateral hillock growth, so that the hillock diameter could be predicted as a function of time. The formalism of secondary grain growth as proposed [71] was applied, motivated by the observation that the hillocks were larger than the surrounding grains. Pennebaker made additional assumptions: different crystallographic orientation of hillocks and film, different stress states of the hillocks, a homogeneous stress in the film, and complete compressive stress relaxation in the film by hillock formation. These assumptions could not be experimentally verified by the measurement techniques available at the time of the study, which was conducted 1969.

2.4 Summary of the literature and motivation

The thermomechanical behavior of thin Al and Cu films has been studied extensively, and the room temperature flow stresses could be reasonably explained by theoretical models. Epitaxial Al and Cu films follow the Nix Freund model. The source model provided a better fit to the experimental data for polycrystalline Cu films thicker than 400 nm.

The stress evolution at elevated temperatures in Cu films was explained by the constrained diffusional creep model. *In situ* TEM experiments of ultra-thin Cu films supported this explanation, because parallel glide dislocations were found as predicted. However, to better describe the stress-temperature curves at elevated temperatures, it was necessary to include either a threshold for grain boundary diffusion or thermally activated dislocation glide as an additional deformation mechanism. It is not yet clear, which mechanism is active. Whether or not the Cu oxidized at elevated temperatures during thermal cycling is still an open issue. Also, the first wafer curvature experiment of Au on Si pointed to constrained diffusional creep, although no comprehensive analysis was conducted.

Hillock formation as a second diffusional mechanism was found to relax compressive stresses at elevated temperatures for various material systems. The mechanisms are different for different material systems, but they all involve long-range material transport, where the microstructure, in particular grain boundary orientation

was found to be crucial. Since, the Au films investigated reacted with the adhesion layer material, the evolution of hillocks on free Au surfaces could hardly be investigated.

The mechanical behavior of Au in small dimensions was studied with several different samples and geometries, from films on substrates, to free-standing films and pillars. A variety of testing methods were employed; wafer curvature, nanoindentation, micro-tensile testing, membrane deflection measurements and nano-compression testing. Mostly, smaller feature sizes (film thickness, grain size, pillar diameter depending on the experiment) exhibited higher stresses, but contradicting explanations are given for the role of grain boundaries as possible dislocation sources. High stresses measured were often attributed to a lack of mobile dislocations [56, 63, 67, 72], but grain boundaries were also sometimes regarded as dislocation sources [56, 60, 63], which implies that smaller grained samples are weaker.

The Au films on Si examined in this study are model systems to investigate the thermomechanical behavior of thin films in two respects and can thus contribute to the understanding of thin film plasticity:

- Au does not react with the surrounding atmosphere at elevated temperatures as e.g. Cu does, but preserves its free surface. Furthermore, the Au films were directly deposited on the amorphous SiN_x diffusion barrier, since adhesion was sufficient. Thus, interlayers that could potentially react with the Au were avoided. This allowed the study of diffusion phenomena, including diffusional stress relaxation by creep and/or surface morphology evolution.
- Two different, thermally stable microstructures at a given film thickness could be prepared, which is usually not easily possible. For the usual thin film microstructure, the grain size scales with the film thickness and is on the order of the film thickness. One set of samples exhibited exactly this behavior. The second set of films had a lateral and vertical grain sizes which was smaller than the film thickness and remained nearly constant over a large film thickness range. Diffusive and dislocation phenomena can thus not only be studied as a function of film thickness, but the contribution of the grain size and film thickness can also be isolated.

3 The thermomechanical behavior of Au films with different microstructures

3.1 Introduction

Microstructure, in particular the grain size, is known to have an important influence on the mechanical performance of materials at room and elevated temperatures. At room temperature, the yield stress in bulk material was found to increase inversely with the square-root of the grain size [73, 74], which even holds for grain sizes down to several 10 nm in the nano-crystalline regime (for a review see [75]). At elevated temperatures, however, small grained materials are less resistant to plastic deformation by creep, because the grain boundaries are preferred diffusion paths. For the mechanical behavior of thin polycrystalline metal films on substrates, additional effects emerge due to the finite film thickness and the constraint that the substrate applies, and the large surface to volume ratio. The room temperature strength of the films is normally determined by the film thickness and increases with decreasing film thickness. This has been extensively studied for Al [5, 7] and Cu [4, 6, 76], because they are the most frequently used metals in microelectronics. Studies have also been extended to Ag [39], Au [38], and NiAl [77]. High flow stresses were attributed to the confinement of a moving dislocation by the film thickness for single crystals [8]; for polycrystalline films additionally by the grain size [9], which is typically on the order of the film thickness. However, simulations suggested that dislocation nucleation may be more important than the confinement of the dislocation motion [10] as observed for Cu films [25].

In recent years, the understanding of diffusional relaxation at elevated temperatures has progressed. This was particularly due to a rigorous theoretical analysis of Gao *et al.* [11], which modeled the substrate constraint by not allowing diffusion along the film/substrate interface. Comparisons with wafer curvature experiments of Cu films still showed that this mechanism alone cannot describe the experimental data [12], but dislocation glide also plays a role. However, heating cycles in a transmission electron microscope [4] provided substantial evidence for the proposed mechanism that grain boundary stresses are relaxed by diffusion of material into or out of the grain boundaries due to tensile or compressive stresses, respectively. As a consequence of this

material accumulation in the grain boundaries, the expected dislocations on (111) glide planes parallel to the film/substrate interface were observed.

The aim of this study was to investigate the stress-temperature behavior of Au films at elevated temperatures and at room temperature employing the wafer curvature method and gain more insight into deformation mechanisms. Au provides the advantage that it does not oxidize and thus can serve as a model system for a free surface. This was crucial to examine diffusional creep phenomena. Furthermore, deformation at room temperature and its dependence on film thickness and grain size was investigated for films with different microstructures for a single film thickness. This should provide additional information on dimensional constraints and their effect on the flow stress.

3.2 Experimental

3.2.1 Film deposition and characterization

Au films were DC magnetron sputtered under ultrahigh vacuum conditions ($\leq 10^{-8}$ mbar) in a commercial magnetron sputtering system (DCA Instruments, Finland). The substrates were (100)-oriented silicon wafers coated on both sides with a 50 nm thick thermal silicon oxide followed by a 50 nm thick CVD silicon nitride layer (Crystec GmbH, Berlin). The wafers and the Au target were Ar^+ sputter-cleaned for two minutes at 200 eV before deposition. The films were sputtered at about 7 Å/s at a sputtering power of 100 W at a pressure of 10^{-4} mbar of pure Ar. By depositing some films at room temperature and others at 300 °C, two different microstructures were created. For a substrate temperature of 300 °C, films with thicknesses from 86 to 847 nm were sputtered. The films deposited at room temperatures were between 57 and 1738 nm thick. Unlike the films sputtered at 300 °C (except for a 600 nm thick film), the ones deposited at ambient temperature were annealed at 500 °C for 30 min directly after deposition to stabilize the microstructure. For most cases, films (1x1 cm^2) were additionally deposited simultaneously on small substrate pieces. These pieces were used for TEM sample preparation. A detailed list of the prepared samples is given in the appendix (chapter 6.1)

For the grain size analysis of films sputtered at 300 °C a LEO 1530 VP field emission scanning electron microscope (SEM) was employed. Images were recorded with a secondary electron detector located in the column, which made the grain boundary grooves visible. The grain boundary traces were manually redrawn onto a

transparency and scanned in order to determine the area of the grains using commercial software (Quantimet Q500/W, Leica). All grain sizes correspond to the diameter of circle having the same area. At least 350 grains were evaluated per film. The measurements were made after the microstructure had stabilized during the first thermal cycle in the wafer curvature tool.

The grain sizes of the films sputtered at ambient temperature were too fine for SEM studies and thus had to be investigated by plan-view TEM. Most of the TEM samples were prepared from the small pieces and the preparation is as follows. A 3 mm in diameter disc was drilled out of the sample, mechanically polished, dimpled, and finally chemically etched with a solution of HNO3:HF:CH3COOH (2:1:1). The silicon nitride served as etch stop so that the Au film remained intact, but the silicon had a hole. For further details and the sample geometry see [16]. Films thicker than 120 nm were Ar+-ion milled to obtain electron transparency. Most of the samples were investigated in a JEOL 2000 FX microscope operated at 200 kV, and some were studied in a JEOL 4000 EX operated at 400 kV. For the grain size analyses, sets of plan-view micrographs at different tilt angles and magnifications were taken. They were processed in the same way as the SEM images. Here at least 220 grains, but usually 300 grains per film thickness were investigated.

The measurement of the actual film thickness is important, because the thickness was not measured during sputter deposition. Instead, the sputtering time which was calibrated by a thickness measurement of a reference sample with a Dektak profilometer. For all types of films, cross-sectional TEM samples were prepared to measure the actual film thicknesses and to study the cross sectional microstructure. The preparation of TEM cross-sections is more complex than for plan-view specimens. Two 3 x 10 mm^2 samples were glued (G1 Epoxy Kit, Gatan; USA) together with the gold films facing each other and subsequently sandwiched between two pieces of silicon with a trapezoidal cross sections for mechanical stability, such that the total height of the stack was about 3 mm (Fig. 3.1).

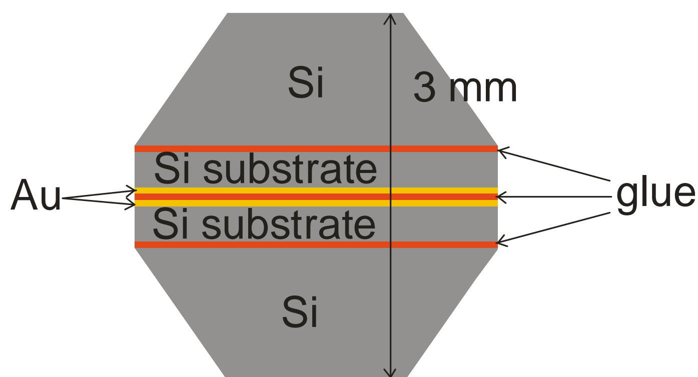

Fig. 3.1: Schematic of a cross-sectional TEM specimen. The film/substrate composites are placed between Si dummies which provide sufficient support for handling.

The specimen was then cut into 400 to 500 µm thick slices using a diamond saw. These were thinned by grinding, then polished on one side and dimpled from the opposite side. Finally, the samples were ion milled to obtain an electron transparent film. For the 1145 thick Au film, a focused ion beam microscope was used to cut an electron transparent lamella for cross-sectional TEM studies. Details of this preparation are given in [17].

The actual film thicknesses were measured for about every second sample from the TEM cross-sectional images. Between 8 and 26 different sites for each sample were evaluated on TEM negatives and averaged. Since the measured values correlate linearly with the nominal film thickness, the actual thicknesses could be extrapolated for the other films (for details see appendix 6.1). The thickness values referred to in the following are all actual thicknesses. The statistical errors of the film thicknesses measured from the TEM micrographs are less than 1.5%. Errors for the linear fits are only about 1%.

Furthermore, grain boundaries parallel to the film substrate interface are found in Au films thicker than 173 nm and sputtered at ambient temperatures. The grain height was also estimated from cross-sectional TEM by counting the intersections of grain boundaries with lines perpendicular to the film/substrate interface. The distances of these lines were larger than the lateral grain size. Between 13 and 63 grains were analyzed. Additionally, the surface roughness of 86, 354 and 688 thick the films sputtered at 300 °C was investigated with an atomic force microscope (AFM). At least four 100 µm^2 scans were evaluated to obtain route mean square (RMS) roughness values.

3.2.2 Stress-temperature measurements

The films were thermally cycled between room temperature and 500 °C and the curvature was measured using a laser scanning technique [4, 18]. The film stress, σ_f, can be calculated from the sample curvature using the Stoney equation [19]:

$$\sigma_f = \frac{M_s \cdot h_s^2}{6h_f} \cdot \Delta K \qquad (1.12)$$

where M_s is the biaxial modulus of the substrate, h_s is the substrate thickness and h_f is the film thickness. ΔK is the change in curvature due to the film stress.

Since the wafers are not ideally flat, their initial curvature was measured prior to film deposition and was subtracted from the film/substrate composite to obtain the film stress. According to eq. (1.12), the experimental error of the stress measurement is composed of substrate and film thickness uncertainties, and of the curvature measurement. The film and substrate thickness errors are 1.5% and 3%, respectively. The error of the curvature measurement depends on the uniformity of the wafer curvature, because it is measured along a single line in this particular experimental setup. Thus, a change in wafer position results in measuring along a different line. For a uniformly curved wafer, this yields very similar measurements. However, if the wafer is non-uniformly bowed, then a different curvature is measured. The non-uniformity is related to the initial curvature of the uncoated substrate. The smaller the curvature the smaller the error induced. Also, since thermal drift during the experiment can change the wafer position, another uncertainty of ± 50 MPa at elevated temperatures with respect to the room temperature stress is introduced. A more detailed analysis of the errors is given in the appendix (6.3.1). While the overall uncertainty in stress values ranges between 6 and 40%, an error of 15 % is typical.

Cooling and heating rates were maintained at 6 °K/min, except for cooling below 100 °C at 4 °C/min, with a nitrogen flow through the furnace provided for cooling. The stress relaxation at 500 °C was studied for two different films sputtered at 300 °C (185 nm and 430 nm thick) and three samples sputtered at ambient temperatures (121 nm, 173 nm and 458 nm thick) by isothermally annealing them at least 180 min.

3.3 Results

In this section, the film microstructure is described in detail and three different types of films will be identified. The stress-temperature curves, the stress-relaxation at 500 °C and the flow stresses at 50 °C and their dependence on film thickness and grain sizes are presented.

3.3.1 Film characterization

Sputtering at two different substrate temperatures yielded different microstructures, which are analyzed in the following, starting with the films sputtered at 300 °C.

3.3.1.1 Films sputtered at 300 °C

At this substrate temperature only films thicker than 86 nm are continuous as determined by plan-view TEM. Films thicker than 86 nm, ranging between 185 and 847 nm, were investigated. Cross-sectional TEM images of the 185 and 847 nm thick films are shown in Fig. 3.2.

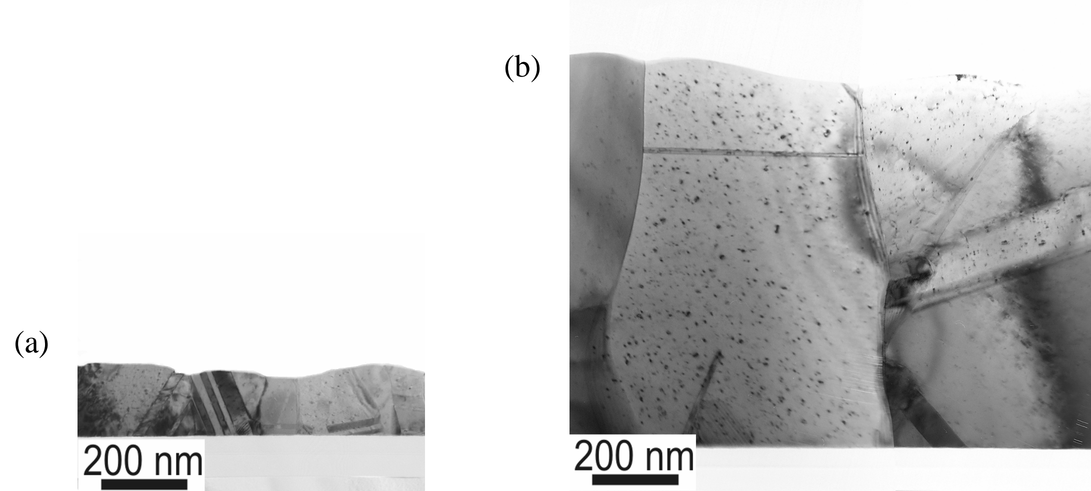

Fig. 3.2: Cross sectional TEM images of (a) 185 nm and (b) 847 nm thick Au films deposited at a substrate temperature of 300 °C. Columnar grains with twins are seen. The 847 nm thick film exhibits a non-columnar grain boundary. The film surface appears fairly rough. The black dots in the grains are artifacts from ion milling.

The films exhibit a columnar grain structure. Some grains have twins parallel to the film/substrate interface and other show inclined twins. The thickest film is mostly columnar, but also exhibits a small fraction of non-columnar grains, as shown in Fig.

3.2b. In addition, the TEM cross-sections also provide information on the surface topography, which was further investigated by AFM seen in Fig. 3.3a for an 86 nm and in Fig. 3.3b for a 688 nm thick Au film. The route mean square (RMS) roughness increased with increasing film thickness from 12.2 nm for the 86 nm thick film to 21.2 nm for the 688 nm thick film. The 688 nm thick film, which is 8x thicker than the 86 nm thick film, is only twice as rough. Thus, in absolute terms, the thicker films are rougher; however, when the roughness is evaluated as a fraction of the film thickness, the thinner films are rougher.

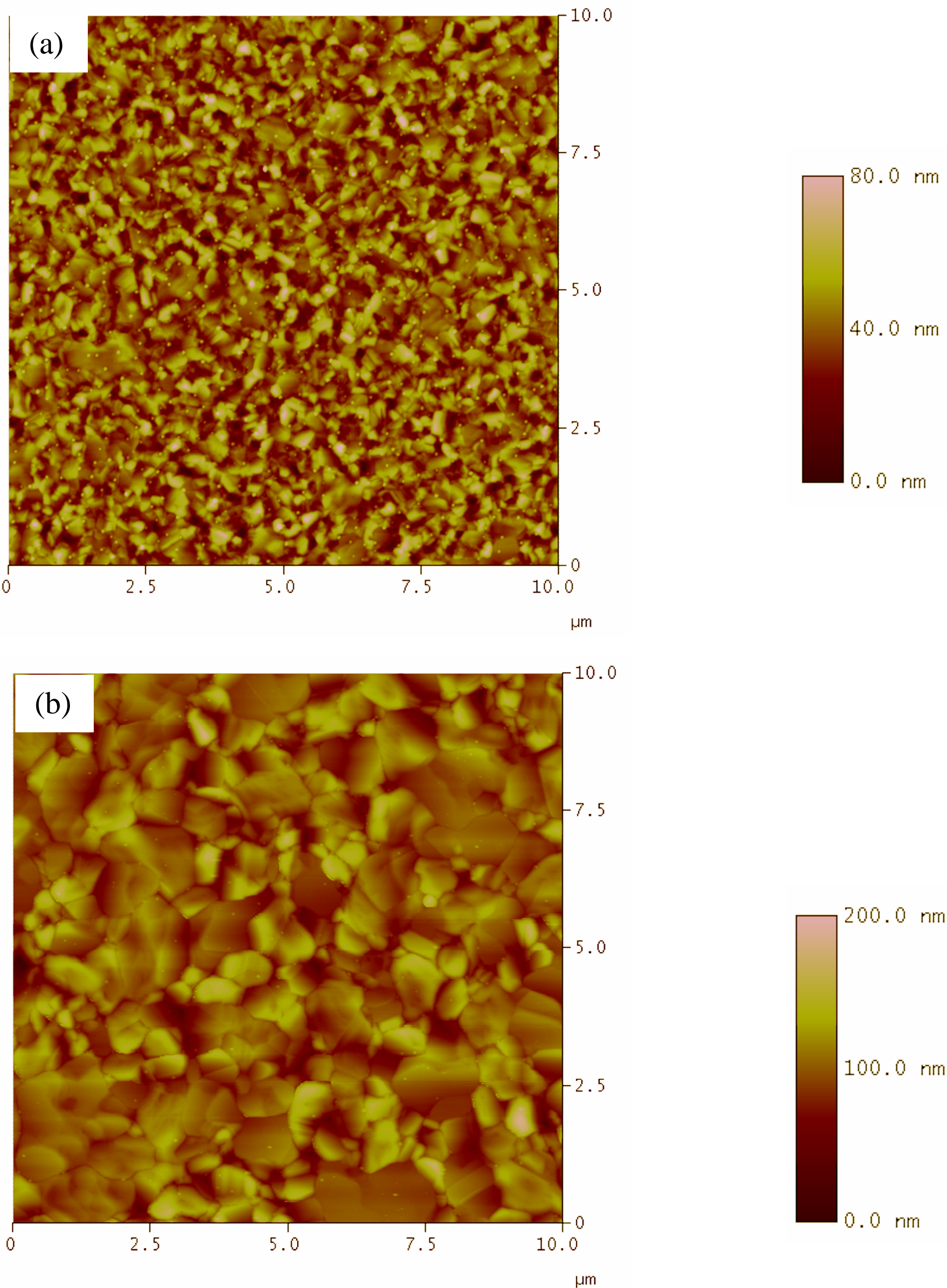

Fig. 3.3: AFM surface scans of 86 nm and 688 nm thick films. The route mean square surface roughness increases from 12.2 nm to 21.2 nm.

SEM plan-view images of the 185 and 847 nm thick Au film surfaces recorded after two cycles are shown in Fig. 3.4. Grain boundary grooves are clearly visible, with some grain boundaries already voided due to thermal cycling. The grain size distributions for the 300 °C deposited Au films are predominantly log-normal (e.g. see Fig. 3.5). Deviations from the lognormal distribution for larger grains visible in Fig. 3.5 may be caused by insufficient statistics. The other films sputtered at 300 °C show a similar behavior. The median grain size values are comparable to the actual film thicknesses and increase linearly with increasing film thickness.

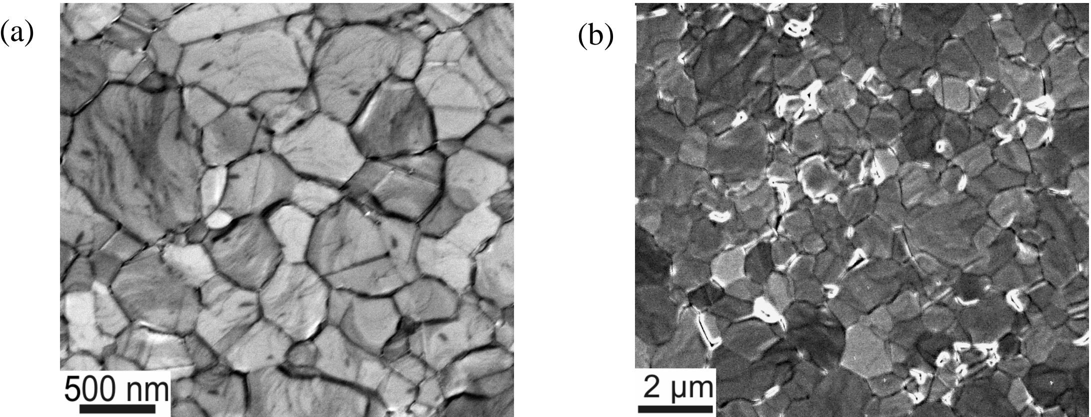

Fig. 3.4: Grain structure as revealed by SEM for the (a) 185 nm and (b) 847 nm thick Au film after 2 thermal cycles. The grain boundary voids seen in the 847 thick Au film resulted from thermal cycling. Note that the micrographs have different magnifications.

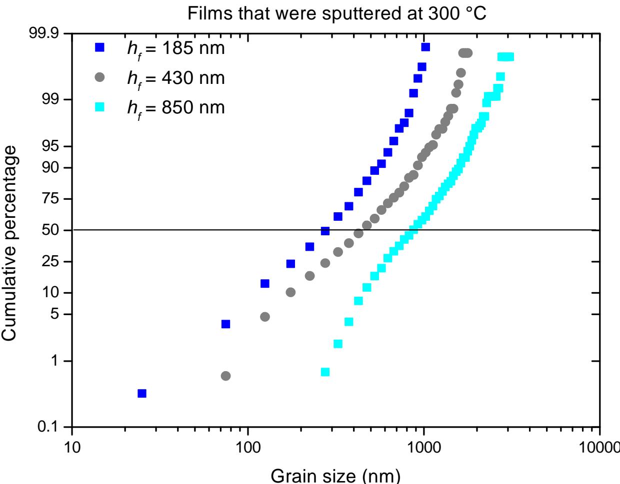

Fig. 3.5: Grain size distributions for Au films sputtered at 300 °C. The distributions are predominantly log-normal and the median grain size increases with increasing film thickness. The deviation at higher grain sizes could result from the limited amount of data. A similar behavior is found for all other films sputtered at 300 °C.

(111)-pole figures (e.g. Fig. 3.6) and rocking curves reveal a broad (111)-fiber texture with a full width half maximum (FWHM) value of 13.1 ± 0.2° for the 185 thick film. With increasing film thickness the FWHM becomes smaller. However, for the 847 nm Au film, which is the thickest film, it is still 10.9 ± 0.2°.

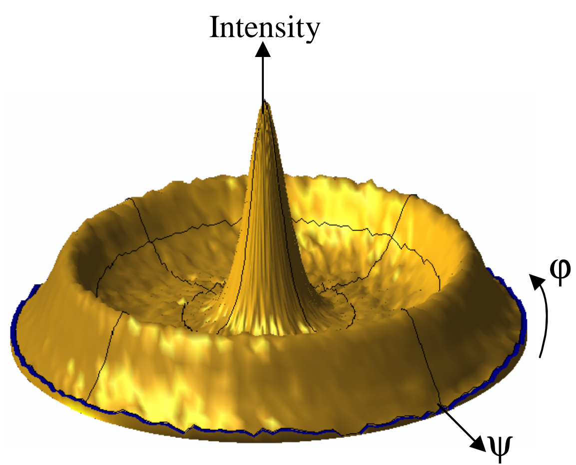

Fig. 3.6: (111)-pole figures for the (a) 185 nm thick with a FWHM of 13.1 ± 0.2°.

The microstructure found in these films is comparable to other thin fcc metal films on Si, e.g. Cu [4, 12] and Ag [39], with the exception that the texture is broader and no (100)-texture component was found for thicker films.

3.3.1.2 Films sputtered at ambient temperatures

Sputtering at ambient temperatures resulted in a very different microstructure, which can be divided into two different types: thin columnar and thicker non-columnar films. The TEM cross-sections of the 121, 265 and 1154 nm thick films presented in Fig. 3.7 illustrate this behavior.

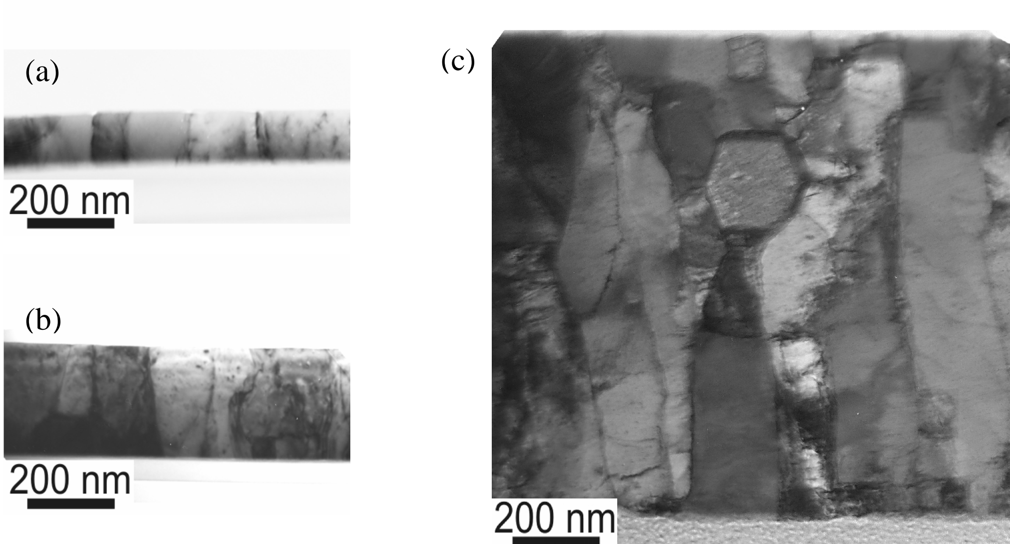

Fig. 3.7: Cross-sectional TEM images of (a) 121 nm, (b) 265 nm and (c) 1145 nm thick Au films. The 121 nm thick film exhibits columnar grains. The thicker films have grain boundaries parallel to the film/substrate interface. Note that all figures have the same scale.

The 121 nm thick film had columnar grains, as did all films thinner than this thickness. The 265 and 1150 nm thick films are non-columnar with grain boundaries parallel to the film substrate interface. The portion of non-columnar grains increased with film thickness. The average grain heights increases from 105 ± 15 for the 173 nm thick film up to 300 ± 45 nm for the 1154 nm thick film.

The plan-view TEM images (Fig. 3.8) indicate that the grain sizes are very small for all room temperature deposited films: 83 nm for the 121 nm thick film and only 98 nm for the 1154 nm thick film. In general, the grain sizes are between 69 and 181 nm with predominantly log-normal grain size distributions shown in Fig. 3.9 for the 121, 469 and 1145 nm thick films. As for the films deposited at 300 °C, the distributions deviate from the log-normal behavior for the 469 and 1145 thick Au films at small and large grain sizes. In contrast, for the 121 nm thick film more than three times more grains were measured and thus, the statistics are better. Films with thicknesses thinner than 121 nm exhibited columnar grains roughly equal in size to the film thickness. This microstructure was comparable to the films sputtered at 300 °C, except the texture was much sharper for films sputtered at ambient temperature as shown in Fig. 3.10. For all films thicker than 121 nm and sputtered at room temperature, the grain size is significantly smaller than the film thickness and the grains are not columnar. However, they are not equi-axed, but elongated in the out-of-plane direction.

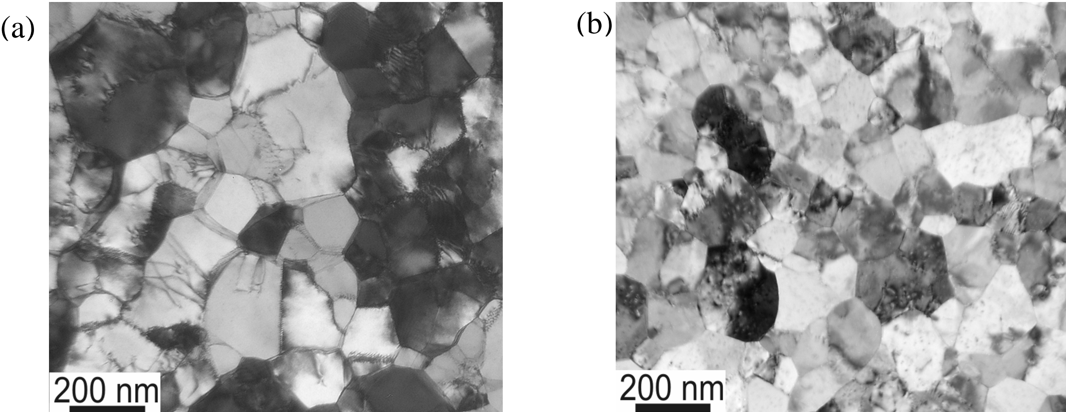

Fig. 3.8: Plan-view TEM images of (a) the 121 and (b) 1145 nm thick films. The grain size remains rather constant at 100 nm with 83 nm for the 121 nm thick film and 98 nm for the 1154 nm thick film.

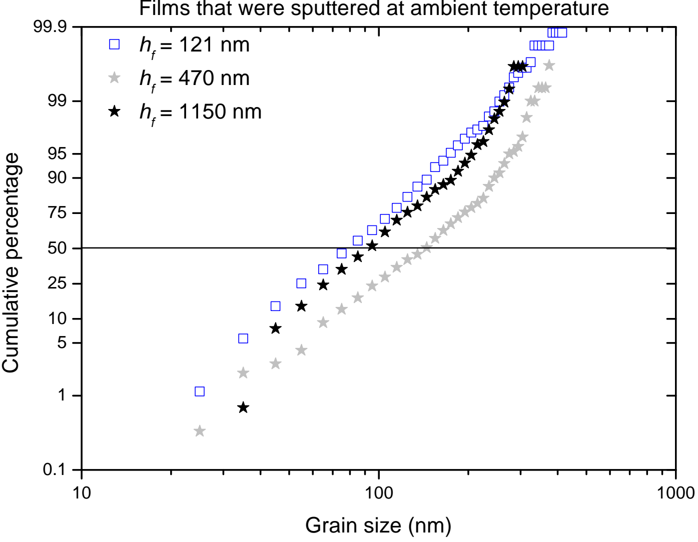

Fig. 3.9: Log-normal grain size distributions of three Au films sputtered at room temperature. The median grain sizes are between 83 and 147 nm.

(111)-pole figures and rocking curves show a (111)-fiber texture with the FWHM of 3.7 ± 0.2° for all film thicknesses. The pole figure of the 1145 nm thick film is shown in Fig. 3.10.

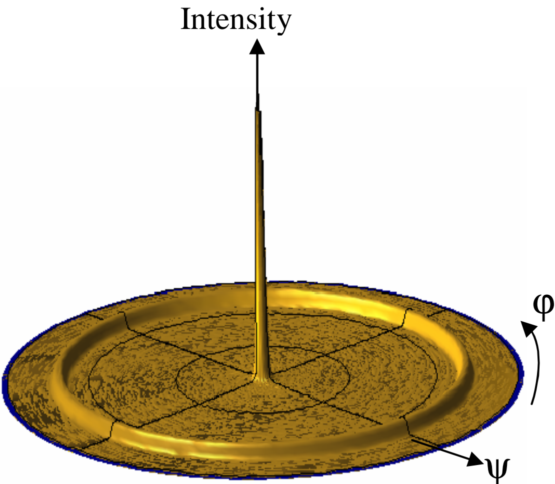

Fig. 3.10: The (111)-fiber texture of 1145 nm thick Au film is seen in the (111)-pole figure. The FWHM is 3.7 ± 0.2° as for all other films sputtered at room temperature.

3.3.1.3 Summary of the different types of films

Fig. 3.11 summarizes the grain sizes for the different films. The columnar films with thicknesses below 121 nm, sputtered at ambient temperatures, and all films sputtered at 300 °C show a linear dependence of the grain size on the film thickness. The grain sizes of the non-columnar films are between 98 and 181 nm for all thickness, where it seems that the thicker films have the slightly larger grains, with the exception of the 1154 thick film. In contrast to the other films, this TEM sample was prepared from a sample that had only been annealed and not thermally cycled, so it could be that the grain size, despite the annealing at 500 °C for 30 min had not completely saturated. The average grain height for the non-columnar films is between 105 and 300 nm, and hence always larger than the lateral grain diameter.

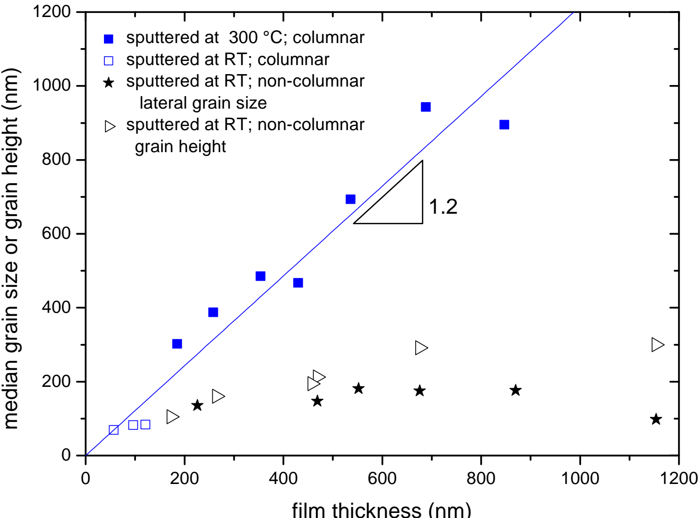

Fig. 3.11: Median grain size vs. film thickness for all deposited films. All columnar films, sputtered at 300 °C (filled squares) and the thinner films sputtered at room temperature (open squares) were fitted together. The slope reveals that the grain size is about 1.2 times the film thickness. The lateral grain size of the non-columnar films (stars) is significantly smaller than the film thickness. The grain height of the non-columnar grains (triangles) is larger than the lateral grain size.

In summary, the Au films in this study can be classified into three categories:

- NC: Non-columnar and sputtered at ambient temperature
- CH: Columnar and sputtered at 300 °C. "H" refers to the film deposition at high temperature.
- CL: Columnar and sputtered at room temperature with "L" refering to the sample preparation at low temperature.

The individual samples will be referred to by these categories, followed by the film thickness in nm, e.g. [NC870] means the 870 nm thick Au film that was sputtered at room temperature and has a non-columnar microstructure. Table 3.1 gives an overview of the three categories with more detailed information and introduces symbols that will help to identify the categories in the course of this work.

Table 3.1: Summary of the different categories of film microstructures

Film type	CH coarse-grained columnar	NC fine-grained non-columnar	CL ultra-thin columnar
Film thickness	86 to 847 nm	173 to 1738 nm	57 to 121 nm
# of samples	9	12	5
Deposition temperature	300 °C	ambient temperature	ambient temperature
Heat treatment after deposition	none	500 °C for 30 min	500 °C for 30 min
Grain size	$1.2 \cdot h_f$	width: 98 to 181nm height: 105 to 300 nm	$1.2 \cdot h_f$
Texture	(111) – fiber texture FWHM = 10.9 – 13.1 ± 0.2 °	(111) – fiber texture FWHM = 3.7 ± 0.2°	(111) – fiber texture FWHM = 3.7 ± 0.2°

3.3.2 Stress-temperature behavior

In this chapter, the stress evolution during thermal cycling is shown for each category of samples: NC, CH, and CL. Since the stress-temperature behavior of different film thicknesses is similar for the types NC and CH, the results of one film thickness is plotted, described, and analyzed as an example for all other curves of that particular type. The stress-temperature behavior of the type CL is discussed by comparing two different samples having the same film thickness. The stress-temperature curves of all films are shown in the appendix 6.3.2.1.

3.3.2.1 Stress-temperature behavior of non-columnar films (type NC)

The first two cycles for the 870 nm thick Au film [NC870] are shown in Fig. 3.12. For the first cycle, the starting stress at room temperature was a little lower than the final stress, which was also the starting stress of the second cycle. This is due to the stress relaxation after film deposition before the stress-temperature measurement. During the initial heating, the deviation from thermoelastic behavior occured at a lower temperature than for the second cycle. The lower starting stress causes the stress to enter the compressive stress regime earlier; at 210 °C for the first cycle as compared to 240 °C during heating the second cycle. The stress relaxation before testing was not studied systematically and the main attention will therefore be focused on the second and subsequent cycles, which are repeatable. All discussions and descriptions are made for those cycles, unless stated otherwise. The first cooling cycle already shows the same behavior as subsequent cycles.

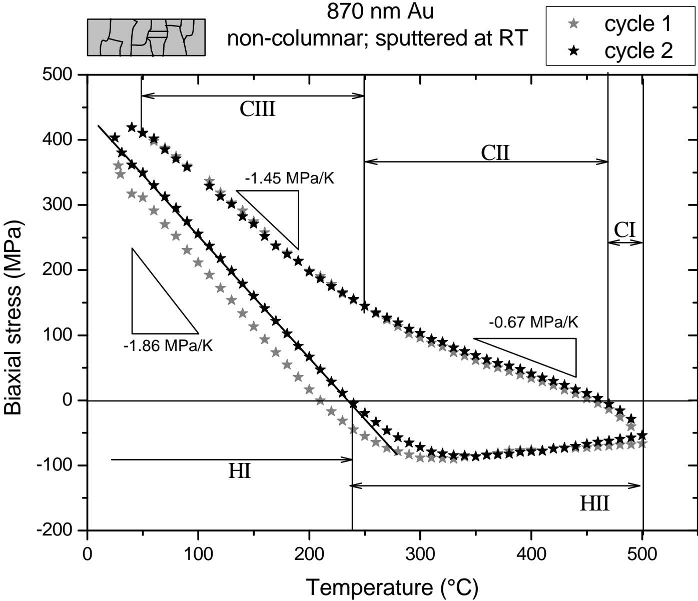

Fig. 3.12: Stress-temperature cycles of the non-columnar 870 nm thick Au film [NC870]. The heating portion of the second cycle exhibits a thermoelastic regime HI and a plastic regime HII. During cooling three regimes appear with a thermoelastic regime CI over a small temperature range and two plastic ones.

The heating portion exhibits two different regimes as indicated in Fig. 3.12 by HI and HII: At first the stress decreases following the thermoelastic line with a slope of

-1.86 MPa/K. Then at 260 °C the stress deviates from this line, bends over, and the compressive stress slightly relaxes at elevated temperatures. During cooling three regimes can be identified; denoted with CI, CII and CIII in Fig. 3.12. Over the first 30 °C during unloading the stress rises significantly (CI) nearly according to a thermoelastic line. In the second regime CII the stress decreases with a shallow slope of – 0.67 MPa/K. At 260°C the transition to the third regime CIII takes place, where the stress increase is larger again (slope: -1.45 MPa/K).

The stress evolution during thermal cycling of the other type NC films is similar to that shown in Fig. 3.12. All curves show these five regimes:

- HI: The thermoelastic slopes during heating range between -1.76 and -2.14 MPa/K and do not depend systematically on the film thickness. The majority of the slopes are around -2.00 ± 0.12 MPa/K
- HII: The transition to this regime occurs between 200 and 280 °C. The stress remains roughly constant in compression. The slight increase or decrease of compressive stress seen in some stress-temperature (e.g. Fig. 3.12) is within the error margins for the wafer curvature measurement as described in experimental section.
- CI: The stress increases rapidly; at maximum over the first 40 °C during cooling. The slopes are between -1.21 to - 2.64 MPa/K, however, the error is large because only a few data points (maximum 4) were fitted.
- CII: The stress only slightly increases in this regime. The slopes range between -0.31 and -0.75 MPa/K and despite the data scatter a general trend of increasing slope with decreasing film thickness is found.
- CIII: The transition to this regime takes place between 230 and 280 °C with thinner films having higher transition temperatures. The slopes range between -1.21 and -1.57 MPa/K.

3.3.2.2 Stress-temperature behavior of columnar films (type CH)

For the columnar films that were sputtered at 300 °C (type CH), the 430 nm thick Au film is given as an example (Fig. 3.13). Again, the first cycle starts at a lower initial stress than the second and third cycle. After thermoelastic loading, a stress drop occurs at 180 °C for the first cycle, which might be indicative of grain growth, since the microstructure was not stabilized by an annealing heat treatment before testing. To investigate this effect, a 600 nm thick film was sputtered at 300 °C, and in contrast

annealed immediately after deposition to 500 °C for 30 min in the sputtering chamber. The room temperature stress at the beginning of the thermal cycle was similar to the final stress after the cycle and no stress-drop occurred. For the 430 nm thick film in Fig. 3.13, all cycles coincide above 300 °C. The second and third cycles exhibit higher room temperature stresses, and did not show a stress-drop during heating. At 220 °C thus both deviate from the thermoelastic line and reach a stress plateau. Two regimes can be discriminated: a thermoelastic regime HI with a slope of -1.98 MPa/K and a plastic regime HII. No thermoelastic unloading is observed, but the cooling portion shows two regimes with a transition from CII to CIII at 260 °C. CII has a very small slope of -0.51 MPa/K, followed by a slope of -1.44 MPa/K for cooling in regime CIII.

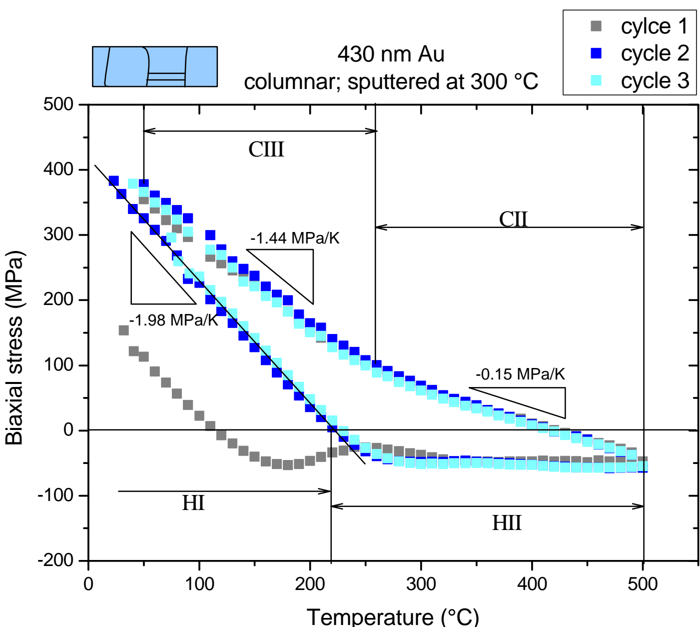

Fig. 3.13: Stress-temperature curve of [CH430]. The stress-drop during the first cycle is probably due to an irreversible change in microstructure, e.g. grain growth. Two regimes can be identified during heating and cooling for the second and third cycles.

For the type CH films the regimes can be summarized as follows. However, evaluation of the 86 nm thick film was not possible due to experimental problems.

- HI: The thermoelastic slopes range between -1.77 and -1.98 MPa/K, except for sample [CH847], which has a slope of -1.61 MPa/K. The slopes do not depend

systematically on the film thickness.

- HII: The transition to this regime occurs between 200 and 250 °C. All films thicker than 258 nm exhibit a plateau, where slight stress increases or decreases are within the error. The film stresses of [CH185] and [CH258] decrease further while heating to 500 °C.
- CII: The shallow slopes in this regime are between -0.36 and -0.50 MPa/K, and they increase with increasing film thickness.
- CIII: The transition temperatures from CII to this regime are between 200 and 270 °C. The slopes increase with increasing film thickness from -1.53 to -1.19 MPa/K.

3.3.2.3 Stress-temperature behavior of the ultra-thin columnar films (type CL)

For this thickness regime, large stress variations among the different samples are observed especially at elevated temperatures. As an example, two second cycles for two 121 nm thick Au films ([CL121a] and [CL121b]) are shown in Fig. 3.14. The thermoelastic slopes during heating are the same (-2.12 MPa/K) and the transition to regime HII is between 260 and 280 °C for both films. However, [CL121a] exhibits less stress relaxation at elevated temperatures. The stress difference at elevated temperatures is large, but it cannot be conclusively decided whether this is still an artifact due to thermal drift or whether it is real. Unloading is thermoelastic for both films, and they eventually enter a plastic regime. However, regime CII is very short and not clearly identifiable. Therefore, no transition temperatures and slopes were determined as for the other films.

All films of type CL exhibit thermoelastic behavior, followed by a plastic regime during heating. Initial cooling occurs according to a thermoelastic line that is followed by a plastic regime. The cooling portion of the 96 nm thick Au film however is more similar to the type NC films, i.e. it exhibits two distinct plastic regimes.

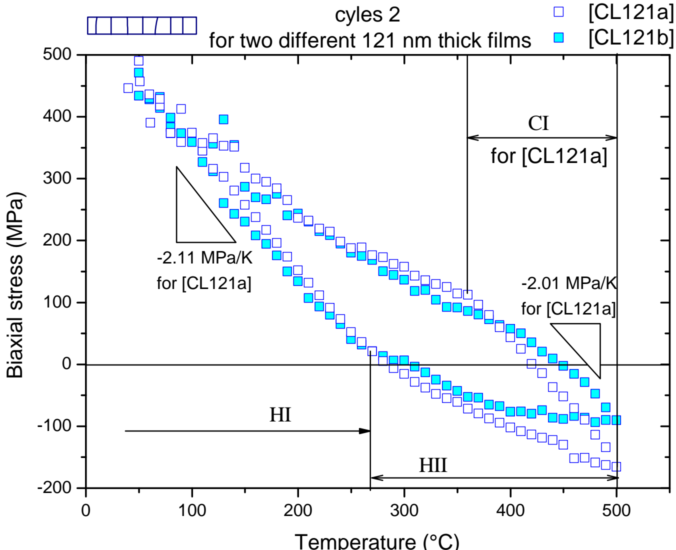

Fig. 3.14: 2nd stress-temperature curves for two different 121 nm thick Au films. The initial thermoelastic heating is similar, but at elevated temperatures the stress in sample [CL121a] decreases more than in [CL121b]. It is not clear whether this is a measurement error or inherent to the samples. The first cooling portion is thermoelastic for both, followed by plasticity.

3.3.2.4 Stress relaxation at 500 °C

Fig. 3.15 depicts the compressive stress relaxation during annealing at 500 °C for the three different types of films.

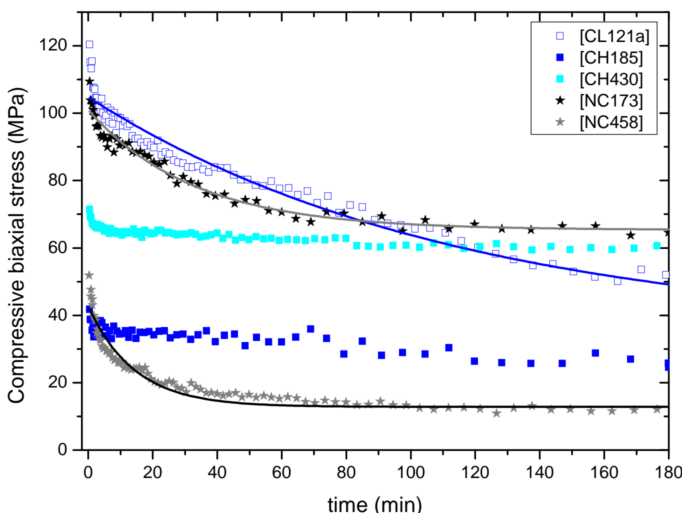

Fig. 3.15: Stress relaxation curves at 500 °C for [CH185], [CH430], [NC173], [NC458] and [CL121a]. The stresses in the columnar films of type CH do not relax much, while type NC films relax significantly and finally reach a constant stress level. The ultra-thin columnar film [CL121a] exhibits a large stress relaxation over 180 min. The fits follow an exponential decay.

Each film type exhibited a different stress relaxation profile. Two films of the type CH were investigated ([CH185], [CH430]). In both CH-type films, the stress decreased 5 MPa over a time period of less than 15 min until a constant compressive stress level was reached. The non-columnar films [NC173] and [NC458] attained a constant stress level after a significantly longer time of 65 min. The stresses relaxed by 35 MPa for both these films. For the thinnest film [CL121a] the stress continued to decrease beyond the 180 min anneal. After 300 min it had relaxed by 80 MPa. The relaxation curve for the type NC and type CL film can be fitted by an exponential decay function, which is indicative of diffusional creep as will be discussed later:

$$\sigma = \sigma_0 - B \exp\left(-\frac{t}{t_0}\right) \tag{3.13}$$

where σ_0, B and t_0 are the fit parameters. The values are given in Table 3.2.

Table 3.2: Parameters of the fits in Fig. 3.15.

Sample	σ_0 (MPa)	B (MPa)	t_0 (min)
[CL121a]	34	70	114
[NC173]	65	36	33
[NC458]	13	30	14

3.3.2.5 Summary of the stress-temperature experiments

Table 3.3 summarizes the characteristics of the stress-temperature behavior of the three sample types, with the exclusion of the type CL 96 nm thick film, because its stress-temperature behavior resembled the of type NC films.

Table 3.3: Characteristics of the stress-temperature behavior for the different types of films.

Film type	Type NC	Type CH	Type CL *
Film thicknesses	173 to 1738 nm	185 to 847 nm	57 to 121 nm
Regime HI: thermoelastic slope	-1.76 to -2.14 MPa/K	-1.77 and -1.95 MPa/K except [CH947]: -1.61 MPa/K	-2.12 and -2.42 MPa/K
Transition temperature from HI to HII	200 to 280 °C	180 to 220 °C	200 to 280 °C
Regime HII: stress	plateau	plateau except [C185] and [CH265]: further decrease	increase of compressive stress
Regime CI: slope of initial unloading	thermoelastic to max. 460°C: -1.28 to -2.64 MPa/K	no thermoelastic unloading	thermoelastic to min. 440 °C: -2.11 to -2.42
CII slope	-0.30 to -0.75 MPa/K large scatter, increase with increasing h_f	-0.36 to -0.51 MPa/K increase with increasing h_f	-
Transition temperature from CII to CIII	230 to 280 °C	200 to 270 °C	-
CIII slope	-1.21 to -1.57 MPa/K	-1.14 to -1.53 MPa/K increase with increasing h_f	-
Stress relaxation at 500 °C	[NC173], [NC458] stress plateau after about 65 min	[CH185], [CH430] stress plateau after about 15 min	[CL121a] compressive stress decreases over at least 300 min

* without the 96 nm thick film [CL96]

3.3.3 Stress at 50 °C

The stresses at 50 °C, usually determined by averaging the stress at 50 °C after three stress-temperature cycles, will be presented as a function of the film thickness and grain dimension. To investigate their dependence on the film thickness for columnar films, both types of columnar films (CH and CL) are plotted together vs. the inverse film thickness in Fig. 3.16. The errors differ from sample to sample, because they depend on the quality and curvature of the individual substrates, as described in section 3.2.2. A linear fit with weighted errors gives a slope of 11 ± 2 MPa·µm, and an intercept of 310 ± 20 MPa. The correlation factor, *R,* of 0.83 indicates that the linear dependence of the flow stress on the inverse film thickness can be considered significant, given the number of the data points included in the fit (12).

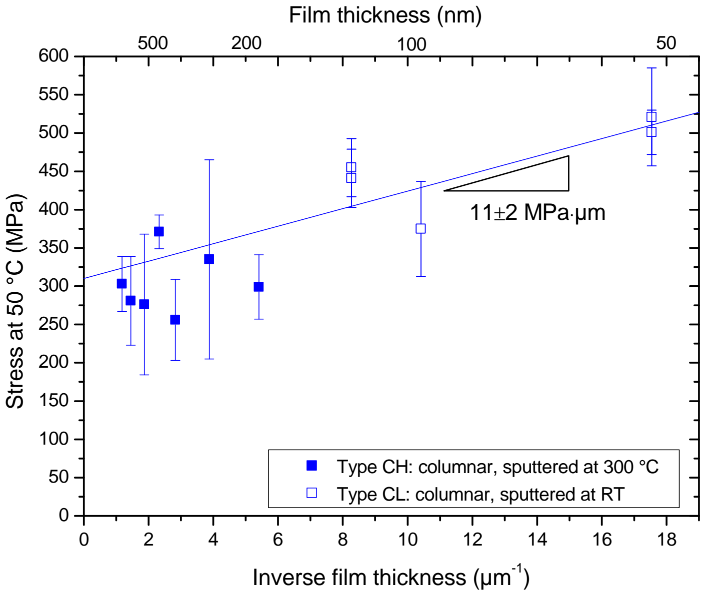

Fig. 3.16: The stress at 50 °C is plotted vs. the inverse film thickness for columnar films of type CH (filled squares) and type CL (open squares). A linear fit through the data of both types yields a slope of 11±2 MPa·µm and an intercept of 310±20 MPa.

Although the grain size is much smaller than the film thickness for type NC films, it is nevertheless instructive to plot the 50 °C stresses as a function of film thickness and grain height, which is essentially an effective film thickness. Fig. 3.17 shows that for both parameters, despite the large scatter of the data, the stress at 50 °C slightly increases with decreasing film thickness and grain height.

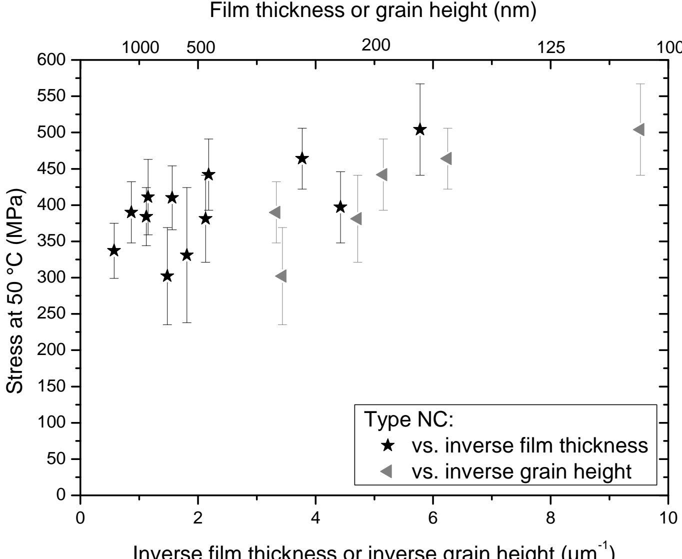

Fig. 3.17: Flow stresses at 50 °C of the non-columnar films (type NC)-films vs. the film thickness and grain height exhibit a slight increase with decreasing dimension.

Another microstructural parameter is the lateral grain size. In this case, the flow stress values of all three types of films fall onto a line when plotted vs. the inverse lateral grain size (see Fig. 3.18). A linear fit weighting the errors yields a slope of 12 ± 2 MPa·µm and an intercept of 303 ± 15 MPa. The quality of this fit is given by R = 0.79.

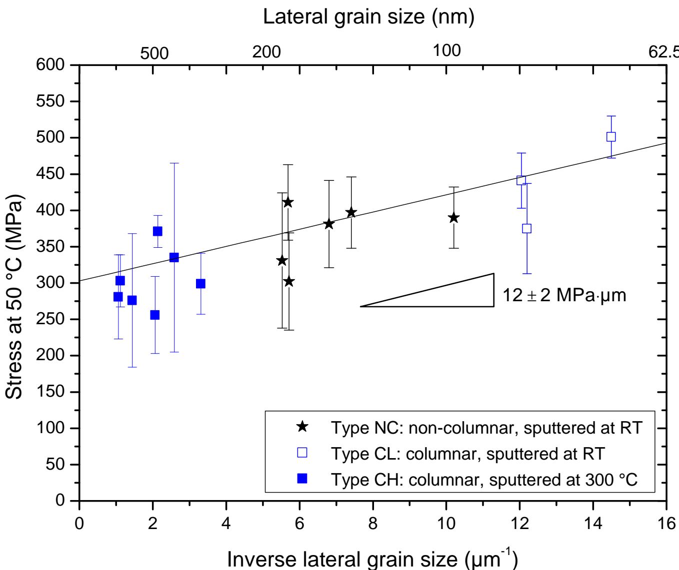

Fig. 3.18: Flow stress vs. the inverse lateral grain size for all three types of films. The linear fit includes all data points. The slope is 12 ±2 MPa·µm and the intercept of 303±16 MPa. The errors have been weighted in the fit.

3.3.4 TEM observations

TEM images were not only recorded to investigate the microstructure, but also to provide information on the defect structures in the films. Fig. 3.19 shows the plan-view TEM image of a larger grain in film [CH86] after thermal cycling to 500 °C. Several parallel glide dislocations, emitted from nearly opposite triple junctions (1 and 2), are observed. They moved towards each other and finally two of them interacted, as can be seen in the point “A”.

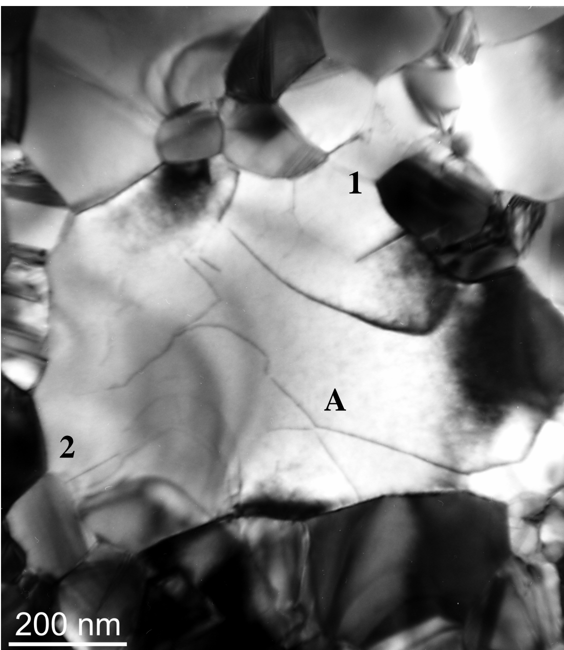

Fig. 3.19: A large grain in a 86 nm thick Au film that was sputtered at 300 °C contained different families of parallel glide dislocations after thermal cycling to 500 °C, which had also reacted. The “A” refers to the reaction point. 1 and 2 indicate the triple junctions from where the dislocations were emitted.

For the type CL films, films of all thicknesses were investigated and all were found to exhibit parallel glide dislocations. Fig. 3.20 shows a micrograph of [CL96] as an example. The arrows in the elongated grain indicate the parallel glide dislocations.

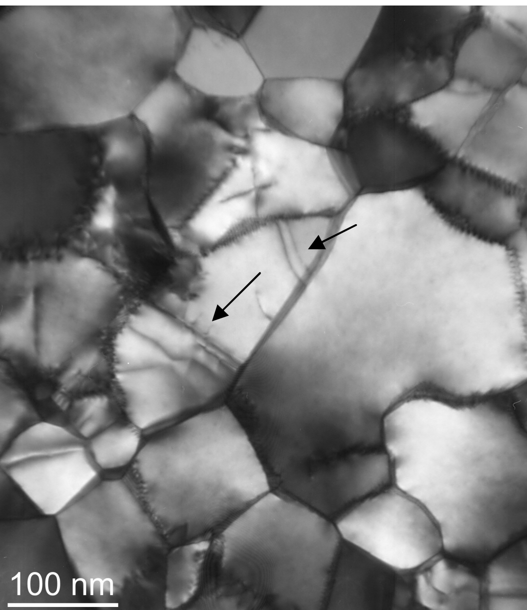

Fig. 3.20: Plan-view TEM image of [CL96] showing parallel glide dislocations as indicated by the arrows.

Furthermore, type CL films additionally exhibited many low-angle grain boundaries. Fig. 3.21 depicts two of them, indicated by the arrows, in a 57 nm thick film ([CL57a]). The individual dislocations that compose the grain boundaries are clearly visible.

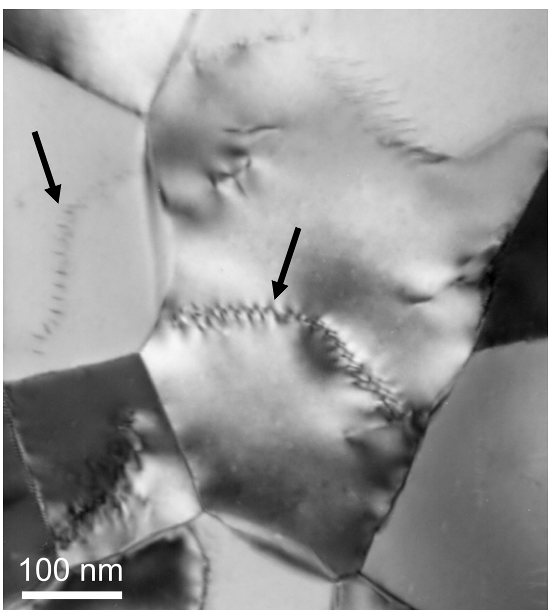

Fig. 3.21: Plan-view TEM images of [CL57a] showing low-angle grain boundaries (indicated by the arrows). The individual dislocations, of which they are composed are clearly visible.

3.4 Discussion

The thermomechanical behavior of thin metal films is microstructure dependent. Thinner films and finer grain sizes are expected to result in higher flow stresses at room temperature. At elevated temperatures, the grain size is anticipated to significantly control the extent of stress relaxation, because the grain boundaries are major material transport pathways for creep [27], and hence more grain boundary area means more diffusive stress relaxation. In this section, the stress-temperature behavior is critically discussed with respect to the film microstructure. The experimental stress-temperature curves of the Au films were found to exhibit several regimes. These regimes are discussed with respect to the most likely deformation mechanisms. The flow stresses and their dependence on microstructural parameters such as film thickness and grain size are also carefully examined and related to common models for thin film plasticity.

3.4.1 Stress-temperature behavior

The stress-temperature curves differ for the film types, but they also have some common features: Upon initial heating, they all behaved thermoelastically (regime HI). The transition to HII occurred between 180 and 280 °C for all film types. During cooling, type CH and NC films exhibited the regimes CII and CIII with transition temperatures between 200 and 280 °C. Only for type CL films, it was hard to identify regime CII and to detect the exact transition temperatures, because regime CI extended over a rather broad temperature range, so that regime CII was very short. Additionally, the individual stress measurements scattered. Nevertheless, the transition temperatures generally were found to be independent of the film microstructure and had values above a homologous temperature of 1/3 (T_m[K]/3 ≅ 175 °C), where grain boundary and surface diffusion are active. Therefore, it can be concluded that diffusive processes played a major role during stress evolution at elevated temperatures for all three film types. The mechanisms will be discussed in the following, because they are expected to strongly depend on the microstructure.

3.4.1.1 Constrained diffusional creep in thin columnar Au films

Type CH and CL films fulfill the precondition for constrained diffusional creep [11], namely a columnar grain structure and significantly fast surface diffusion, because the surface is bare. Parallel glide dislocations, which are a direct consequence of the material transport into the grain boundaries [4, 78], were in fact, experimentally

observed for the first time in Au (see Fig. 3.19 for type CH and Fig. 3.20 for type CL films). The first and so far only other direct observations of these types of dislocations were made in unpassivated Cu films by Balk *et al.* [4].

If constrained diffusional creep were the predominant deformation mechanism at elevated temperature, the stress-temperature curves should reflect this, too. First, the behavior of type CH and CL films will be briefly recapitulated with respect to the differences for types CH and CL and then simulations according to the constrained diffusional creep model are presented. In contrast to type CH films, type CL films did not exhibit a stress plateau during heating at elevated temperatures (see Fig. 3.13 and 3.14), but the compressive stresses increased until 500 °C was reached. When annealed at 500 °C, however, the compressive stresses relaxed significantly (see Fig. 3.15), while they remained nearly constant for the type CH films. This indicates that the stress relaxation in type CH films had already taken place during the thermal cycle and that a certain residual stress remained. Initial unloading of type CL followed, as opposed, to type CH a thermoelastic line and thus regime CII was very short.

The stress-temperature behavior is now compared to the stress-temperature behavior simulated for constrained diffusional creep. The focus will be on the high temperature regime, where diffusion is active, since dislocation plasticity is not included in the simulation. The simulations follow Weiss *et al.* [12, 50]. The equations are given in section 2.2.1, and all general parameters are listed in Table 3.4.

Table 3.4: Parameters for the simulation of the stress-temperature curves

Parameter	Value	Reference
heating rate	0.1 K/s	-
biaxial modulus	180 GPa	[79] mean value between RT and 500 °C
difference in thermal expansion coefficients α_{Au} -α_{si}	$12 \cdot 10^{-6}$ K^{-1}	[80, 81]
grain boundary diffusion pre-factor $\delta D_{gb,0}$	$3 \cdot 10^{-16}$ m^{3}s^{-2}	[82]
grain boundary activation energy Q_{gb}	85 kJ/mol	[82]
atomic volume Ω	$1.69 \cdot 10^{-29}$ m^3	
Young's modulus	78 GPa	[79]
Poisson's ratio	0.42	[79]
Schmid factor	0.27	-

The simulated stress-temperature curves for the grain boundary traction, the thermoelastic intragranular stress and the resulting film stress are shown in Fig. 3.22 together with the measured second cycle of [CH430]. This sample was already presented in Fig. 3.13 and had a median grain size of 469 nm.

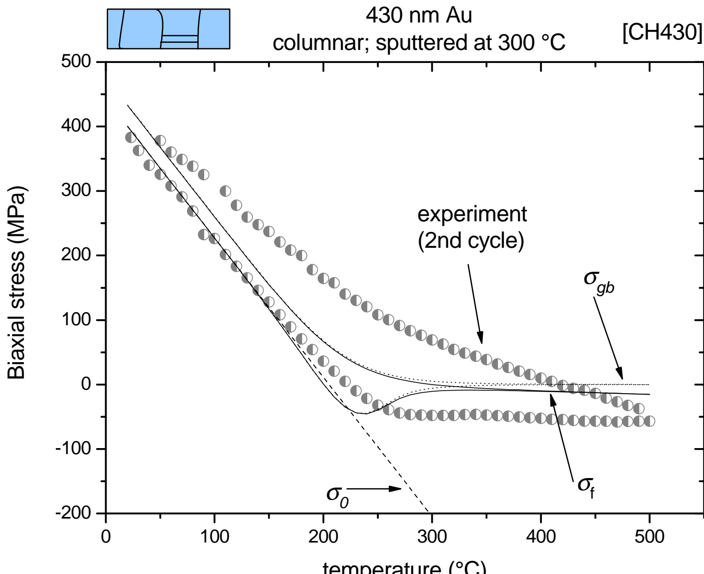

Fig. 3.22: Comparison of experimental stress-temperature behavior of film [CH430] with modeled curves for constrained diffusional creep (solid line). The dotted line represents the grain boundary traction and the dashed line the thermoelastic stress in the grain interior. For the simulation parameters refer to Table 3.4.

During heating, the deviation from the thermoelastic to the plastic behavior occurred at similar temperatures for the simulated and the experimentally measured curve. However, the grain boundary stress was completely relaxed at 300 °C in the simulation and the film stress increased following a small slope, while the experimental curve showed a constant compressive stress plateau and a significant hysteresis.

Bühler *et al.* [78] proposed a threshold stress for grain boundary relaxation, which would result in a compressive stress plateau. This threshold followed from molecular dynamic simulations, where diffusion into the grain boundaries is a precondition for nucleating climb dislocations in the grain boundaries. A critical stress intensity factor is needed for a dislocation to be released from the grain boundary to glide on a plane parallel to the film/substrate interface. To take this into account, the grain boundary traction in eq. (2.8) is modified as follows [33]:

$$\sigma_{gb} = \sigma_t + (\sigma_0 - \sigma_t)\exp\left(-\frac{\lambda t}{t_0}\right) \tag{3.14}$$

where σ_t is the threshold stress for grain boundary diffusion.

The simulation with a threshold of σ_t = - 50 MPa for [CH430] is shown in Fig. 3.23. For the 121 nm thick films (type CL), the simulation with and without threshold and the measurements for [CL121a] and [CL121b] are shown in Fig. 3.24. The grain size measured from TEM images was 83 nm for [CL121a].

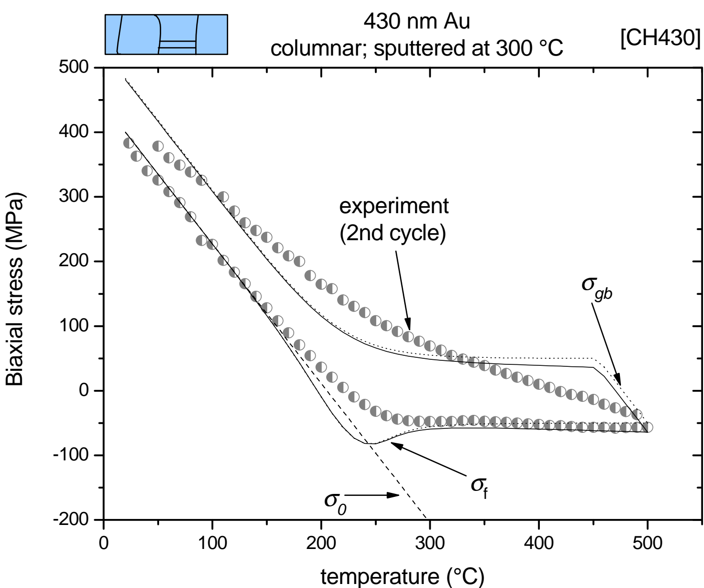

Fig. 3.23: Simulation of constrained diffusional creep (solid line) with a threshold stress of - 50 MP for grain boundary diffusions. The grain boundary traction is shown by the dotted line.

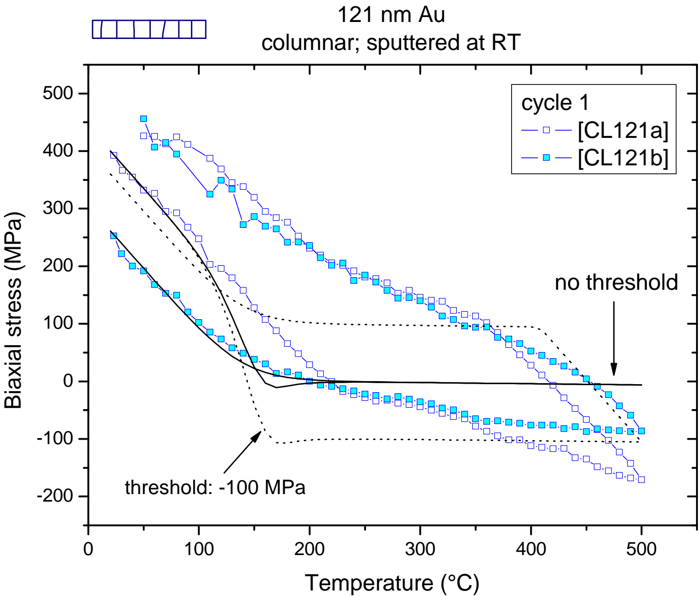

Fig. 3.24: Second stress-temperature cycles of both 121 nm thick films together with the simulation of constrained diffusional creep with a threshold stress of -100 MP.

For [CH430], the heating portion is described well, but cooling is not, because the threshold stress introduces thermoelastic unloading. For [CH121a] and [CH121b], the simulation without a threshold stress does not at all reflect the experimental behavior. The introduction of a threshold, at least, results in a hysteresis at elevated temperatures, but the continued stress increase up to 500 °C is not reproduced. This, however, can be accomplished by increasing the grain size used in the simulation by a factor of three to five as can be seen in Fig. 3.25. Weiss *et al.* [12] had to make a similar assumption for fitting the simulation to the experimental data in thin Cu films. Note that the discrepancies at room temperatures are expected, because the simulation only considers diffusional relaxation, which operates at elevated temperatures and no dislocation plasticity is incorporated.

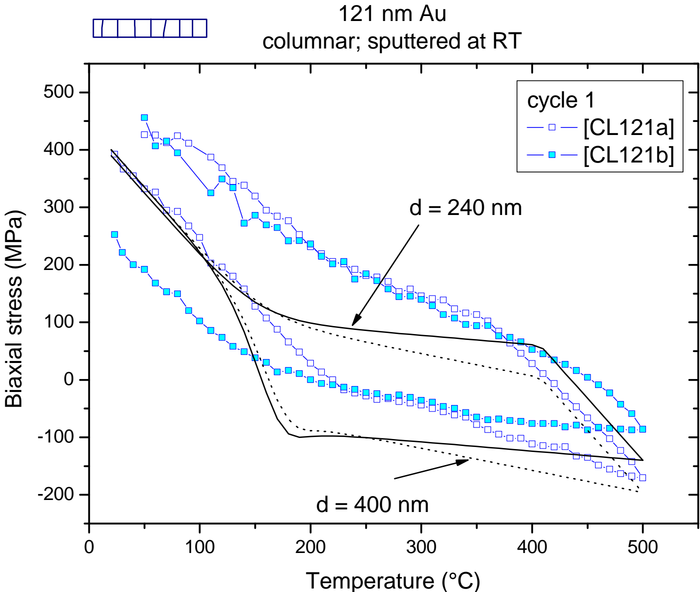

Fig. 3.25: Simulations of constrained diffusional creep with a threshold stress of -100 MPa. The grain size of the 121 nm thick film was chosen 240 and 400 nm, which is three times, and respectively five times the actual grain size of the films.

Although, type CH and type CL films both deform by constrained diffusional creep at elevated temperatures, the films exhibited a different stress-temperature behavior. This might be attributed to the influence of the film properties on surface, grain boundary and interfacial diffusion, which will be qualitatively discussed. As seen in Fig. 3.3, type CH films were significantly rougher. In particular, material transport along the surface into the grain boundaries during cooling could be enhanced by this roughness, because surface curvature reduction might be an additional driving force for material diffusion towards the grain boundaries. Secondly, the difference in the broadness of the texture certainly influences the types of grain boundaries in the film. This, however, affects the grain boundary diffusivity. The (111)-fiber texture of type CH is much broader (FWHM between 10.9 and 13.1°) than the one of type CL films, which is only FWHM of 3.7°. Therefore, CH type films have most likely more high-angle grain boundaries than CL type films. In fact, plan-view TEM images of CL type films revealed many low-angle grain boundaries, as example see the TEM micrograph in Fig. 3.21. The consequence of more high-angle grain boundaries in CH type films could be that grain boundary diffusion is easier and faster than in CL type films. This could be the reason, why CH type films, in contrast to CL type films, do not exhibit thermoelastic unloading and why a larger effective grain size had to be used for the

simulation of CL type films. According to molecular dynamic and discrete dislocation dynamic simulations, high-angle grain boundaries are favorable for nucleation of parallel glide dislocations [78]. Furthermore, in the model of constrained diffusional creep, the absence of interfacial diffusion is assumed, but in any experiment, some diffusion will occur along the interface, albeit it could be very slow compared to surface diffusion. The interfacial structures of films deposited at different substrate temperatures (room temperature and 300 °C) and of films with different grain orientations could vary. One can further speculate that this influences interfacial diffusion in CH and CL type films, and might eventually result in a different stress-temperature behavior, because if significant interfacial diffusion occurs, more stress relaxation at elevated temperature is expected.

The absolute values of the experimental slopes in regime CII are significantly larger than the reduced thermoelastic slope in the simulation (0.1 MPa/K) for type CH films. Furthermore, they increase with decreasing film thickness from 0.35 to 0.72 MPa/K. This can be interpreted as hardening taking place, which is stronger in thinner films. For further investigations, the plastic strain in this regime CII will first be estimated and then the number of dislocations associated with this strain will be calculated. The thermal strain ε_{th} is determined by the following equation:

$$\varepsilon_{th} = (\alpha_{Au} - \alpha_{Si})\Delta T \qquad (3.15)$$

where α_i are the thermal expansion coefficients of the Au and Si and ΔT is the temperature range.

The coefficients of thermal expansion are assumed to be temperature-independent, which is a reasonably good estimate, since the difference of the thermal expansion coefficients only changes from $-11.5\cdot10^{-6}$ K^{-1} at 27 °C to $-12.4\cdot10^{-6}$ K^{-1} at 527 °C [80, 81] The number, N_{disl}, of geometrically necessary dislocations to accomplish the thermal strain, ε_{pl}, in a grain with diameter, d, can be estimated as follows:

$$N_{disl} = \frac{\varepsilon_{th} \cdot d}{b_{eff}} = \frac{(\alpha_{Au} - \alpha_{Si}) \cdot \Delta T \cdot d}{b_{eff}} \qquad (3.16)$$

where b_{eff} is the in-plane component of the Burger vector, b. For parallel glide dislocations, it is simply the Burgers vector, because they move on glide planes parallel to the film/substrate interface.

The dislocation density within a grain is an important quantity for characterizing the defect structure. It can be calculated from eq. (3.16) by dividing by the grain area for grain size, d, assuming the grains to be circular:

$$\rho_{disl} = \frac{N_{disl}}{\pi\left(\frac{d}{2}\right)^2} = \frac{4\varepsilon_{th}}{\pi\, d\, b_{eff}} \tag{3.17}$$

For sample [CH430], the resulting dislocation density is $2.6\cdot10^{13}$ m^{-2} in regime CII, with the Burgers vector b = 0.288 nm and a plastic strain of -0.28 % at a median grain size of 467 nm. This is a high values, which however is a magnitude lower than the dislocation density estimated for a 250 nm thick Ag film by Kobrinsky and Thompson [83], who found $7.5\cdot10^{14}$ m^{-2}.

The densities were estimated for the other films, too. They decrease with increasing film thickness from $5.1\cdot10^{13}$ m^{-2} for [CH185] to $1.4\cdot10^{13}$ m^{-2} for [CH847] (Fig. 3.26). The trend of increasing dislocation density with decreasing film thickness was also expected by Kobrinsky *et al.* [84]. The calculated dislocation densities depend on the median grain size. The grain sizes distributions, however, have similar slopes (see Fig. 3.5), so that under the assumption that dislocations in grains with all sizes behave in a comparable way, the densities can be compared. This would, of course, break down, when a grain only contains one dislocation, because several dislocation in one grain would definitely interact. For the calculated dislocation densities, however, between 4 and 25 dislocations are in one grain. The dislocation densities and the slopes in regime CII are illustrated in Fig. 3.26.

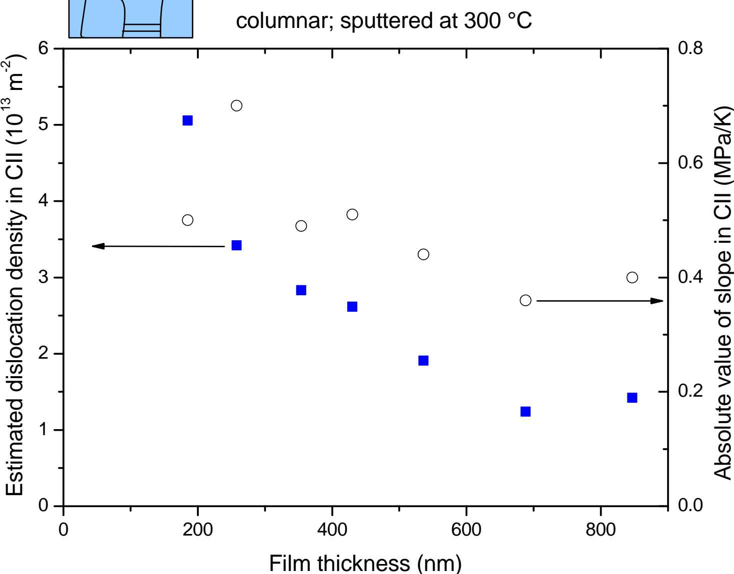

Fig. 3.26: Dislocation densities estimated from the plastic strain and absolute values of the slopes. Both quantities increase with decreasing film thickness.

The comparison leads to the conclusion that higher dislocation densities result in more hardening which could be explained with the interaction of dislocations. If dislocations are already present in a grain, it is presumably harder for new dislocations to move from the grain boundaries where they are nucleated into the grain interior, because they are repelled by the dislocations already present in the grain. Furthermore, with an increasing number of dislocations in a grain it becomes more likely that they are emitted at different grain boundaries and thus can react with each other during glide. TEM of [CH86] showed two families of parallel glide dislocations being emitted from nearly opposite triple junctions (denoted 1 and 2 in Fig. 3.19). They moved towards each other and eventually reacted as can be seen at the point A in the micrograph. These observations are also in accordance with discrete dislocation dynamic simulations [78] of constrained diffusional creep that predict complex networks of parallel glide dislocations.

The ratio of the plastic regimes CII and CIII changes with film thickness. Despite the large scatter in the transition temperature, thinner films exhibit in general a longer diffusive stress regime. This observation is consistent with the stress-temperature behavior of thin Ag films [39]. Studies on Au films on 10 nm W interlayers [85] and Cu films [4] also concluded that thinner films have more diffusive stress relaxation.

3.4.1.2 Stress-temperature behavior of non-columnar Au films

The general shape of the stress-temperature curves for type NC films exhibit the well-known behavior of thin polycrystalline noble metal films on rigid substrates, e.g. Cu [4, 12] and Ag [39]: thermoelasticity (regime HI) followed by plasticity (regime HII) during heating, and upon cooling thermoelastic unloading (regime CI) and two plastic regimes (CII and CIII), where the slope of the first is shallower than that of the second.

The initial thermoelastic unloading during cooling occurs only over a temperature range of 40 °C. For some films, e.g. [NC870] in Fig. 3.12, it might even be superimposed by a stress relaxation process that had already started while the film was still in compression. As already mentioned, in regime CII and HII diffusion is active and diffusional creep is most likely the predominant relaxation mechanism. The unusually fine microstructure provides many fast diffusion pathways, because of the additional grain boundaries parallel to the film substrate interface and the very fine-grains. Because of the in-plane grain boundaries, the preconditions for constrained diffusional creep are not fulfilled, since this model assumes perfectly columnar grain structure. However, the exponential decay of the stresses at 500 °C indicates that a diffusional creep mechanism is active. The exact mechanism is hard to determine, because of the unusual microstructure with some grains being surrounded exclusively by other grains, some are at the interface and others are at the surface. The creep rate is possibly similar to that of classical Coble creep [26]:

$$\dot{\varepsilon} = \frac{K\,\Omega\delta D_{gb}}{kTd^{3}} \tag{3.18}$$

where K is a constant, Ω is the atomic volume, δ is the grain boundary width, k is Boltzmann's constant, T the absolute temperature and d is the grain size. In the case of a thin free-standing foil [86] the grain sizes is twice replaced by the film thickness. For a thin metal film on a rigid substrate the total strain is constant and given by the differences in the thermal expansion coefficients. The stress increase in this regime is 80 ± 40 MPa for all film thicknesses, indicating that grain boundary diffusion is the most important mechanism, because the grain sizes are similar for all type NC films.

3.4.1.3 Comparison the stress-temperature behavior of other metal films

The shapes of the stress-temperature curves of CL type films were similar to those of Cu films with comparable film thicknesses, e.g. the 200 nm thick Cu film in [4] and especially 100 nm [25] and 50 nm [87] thick films, indicating that the same deformation mechanism might act. In fact, Au and Cu films both exhibited parallel glide dislocations, so that it can be concluded that they deformed by constrained diffusional creep. The microstructure and grain sizes of these films were also comparable. Type CH films most likely also deformed by constrained diffusional creep, but had a different stress-temperature curve, when compared to Cu films of comparable film thickness; for a reference see e.g. [12]. Upon initial cooling, the Au films (type CH) did not unload thermoelastically, but the stress only followed a small slope. After the thermoelastic regime, however, Cu also showed a regime with a weak stress increase, comparable to regime CII in Au type CH films, where it was attributed to diffusional deformation. Other Au films on Si with a W interlayer by Leung *et al.* [35] also showed a similar behavior as the films in this study. Even though, columnar Au and Cu films behaved similar in the ultra-thin thickness regime, there was a difference for thicker films.

When compared to films with a passivated surface, e.g. Al [5, 7] or Cu-1%Al [12], the stress-temperature behavior mainly differs during cooling. Thermoelastic unloading occurred over a broad temperature range for passivated films. Also, they only exhibited one plastic regime with a relatively large slope, whereas Au showed a regime with a small slope at elevated temperatures and with a larger slope at lower temperatures. This difference in the stress-temperature behavior can be explained by the absence of surface diffusion in passivated films, so that no diffusional creep can occur, and only dislocation plasticity remains to act at elevated temperatures.

3.4.2 Stresses at 50 °C as function of film thickness and grain size

The dependence of the film stress at 50 °C on the film thickness and the grain size is carefully examined by comparing films with different microstructures and discussing them in light of established models of thin film plasticity.

For comparison of the different types of films to each other and to models, the plot of the stress vs. the inverse film thickness can be very instructive, although the grain size was the smaller dimension for type NC films. Fig. 3.27 shows stress data at 50 °C for all films vs. the inverse film thickness and the most prominent models.

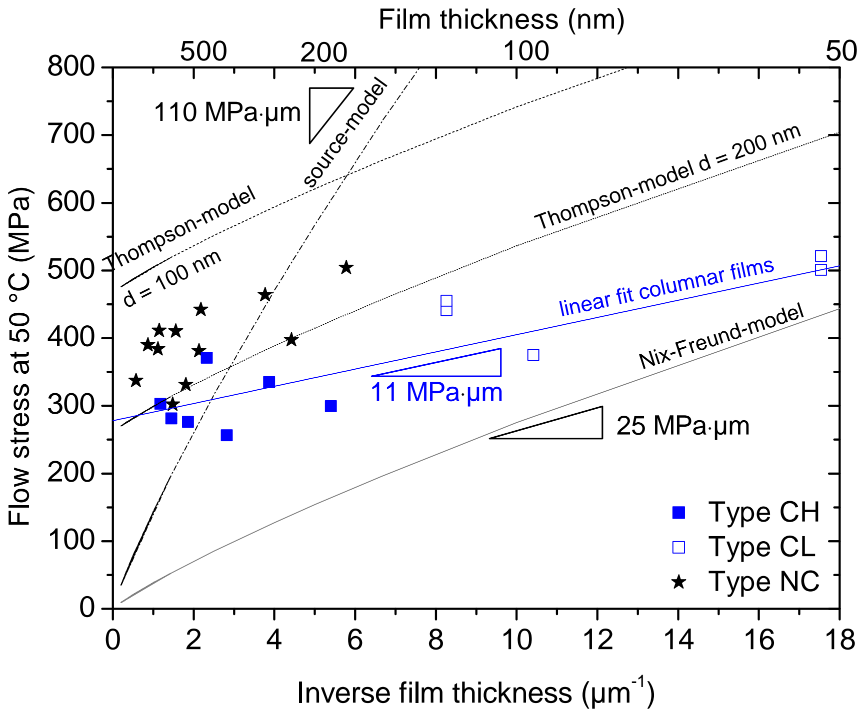

Fig. 3.27: The flow stresses at 50 °C for the three different types of films together with the Nix-Freund model, the source-model and the Thompson-model for 100 and 200 nm. Eq. (2.1) to (2.6) were used with the following parameters: sinϕ/(cosϕcosλ) = 3.1 for a α = 60° dislocation; b = 0.288 nm; β_1=β_2=1, ν_f=0.42, G_{Si}=63.7 GPa, G_{Au}=27.5 GPa; the parameters of the source-model are s_d=h_f/3, α=2.5 and s=0.27.

Type NC films are stronger than type CH films at similar film thicknesses. The grain size, which is significantly smaller than the film thickness for type NC films, provides for additional hardening. For the thinner type NC films with thicknesses of about 200 nm, the stress values are similar to type CL films. In this case, the lateral grain size and the grain height of type NC films are comparable to the grain size and the film thickness of the thickest type CL films ([CL121a], [CL121b]). This comparison already indicates that the smallest dimension determines the strength of the material.

The analysis of the stresses at 50 °C in Fig. 3.16 to 3.18 revealed that they clearly depend on the film thickness and the grain size. For types CH and CL films, the stress decreases linearly with the inverse film thickness, but this line has a very small slope. When the stress is plotted vs. the inverse lateral grain size, the slope is similar. However, type NC films also lie on that line, which means that the grain size as the smaller dimension determines plasticity. For type CH and CL films, the grain size and film thickness are nearly equal. It is, however, remarkable that the stress values of all

types of films fall onto one line, because the grain neighborhood and hence the constraints that a dislocation may feel are different in type NC films and in type CH and CL films. In the non-columnar films, some grains are only surrounded by other Au grains, some are at the film/substrate interface and others are at the surface. In columnar films, every grain has a free surface and a film/substrate interface. It seems that primarily the dimension and not the surrounding of a grain has the major effect on dislocation plasticity. This is opposed to some models, e.g. the Nix-Freund model, where the elastic properties of the substrate enter (eq. (2.1)).

For comparison with the models, the fit of the experimental data for the columnar films (type CH and CL) can be discussed with respect to the Nix-Freund and the source model by von Blanckenhagen (Fig. 3.27). The stresses measured at 50 °C are significantly higher than those predicted by the Nix-Freund model. This is not surprising, because the model only considers an isolated dislocation in a single-crystalline film. The slope, which indicates the dependence on the inverse film thickness, is smaller for the experimental data than for the Nix-Freund model, where the slope is given by the shear moduli of the film and the substrate, the Burgers vector and a factor dependent on the geometry according to eq. (2.1). This smaller slope could imply that it is easier to deposit misfit dislocations at the film/substrate interface or that plasticity in the film is not only accomplished by threading dislocations, but that e.g. parallel glide dislocations could play a role at room temperature.

The slope is also very small when the stress is plotted vs. the inverse grain size, which could be interpreted that the grain boundaries are also weaker than predicted by the Thompson model and perhaps penetrable for dislocations. However, the absolute stresses are relatively high, which points to a large film thickness independent contribution to the stress. It can be speculated that horizontal twins, which are found quite frequently in the films, as seen e.g. in Fig. 3.2, are impenetrable. This would imply that the effective film thickness for dislocations to move is smaller and does maybe not change much with decreasing film thickness. Comparing the Au films to the source model, in which the activation of a dislocation source is the critical step, the experimental data do not at all follow the very steep slope.

For NC films, despite the grain sizes being much smaller than the film thickness, the stresses still are thickness dependent, albeit very weakly. The Thompson model for grain sizes of 100 and 200 nm is also shown in Fig. 3.27. The stress values at $h_f^{-1} = 0$ represent the grain size contribution only. All measured stresses fall between the lines

for grain sizes of 100 and 200 nm, which are the upper and lower limit of the experimentally determined grain sizes. For comparison to the source model, the grain size has to be used as parameter, because it is the smaller dimension. For a grain size of 200 nm, the stress is expected to be 550 MPa, which is larger than the observed values.

3.4.3 Comparison to other studies of Au in small dimensions

Several other studies on Au in small dimensions have been conducted including wafer curvature experiments [85], tensile tests of free-standing films [60, 61], and nano-compression tests of single-crystalline Au pillars [65-67]. In Fig. 3.28 the flow stresses of these studies are compared to the room temperature stresses obtained from the wafer curvature experiments of this study. Note that all data are plotted vs. the smallest sample dimension, which could be the film thickness, the grain size or the pillar diameter.

In this study, the measurement range of Au in small dimension could be further extended into the ultra-thin film thickness regime and first stress values below 100 nm were obtained. The lower limit of most other studies was 200 nm, except for Leung *et al.* [38], who also measured 100 nm thick films. Comparing the results from different sample geometries and testing techniques, it is noteworthy that they all show similar stress values. This further supports the conclusion drawn from the comparison of non-columnar and columnar films that the grain dimension and not the surrounding primarily determines the strength of the material. Moreover, it is generally found that for smaller sample dimensions, the dependence of the stress on the dimension is weaker than for thicker dimensions. The transition occurs at about 500 nm. For the fine-grained free-standing films [61] with grain sizes between 100 and 500 nm a constant stress is reported. Leung *et al.* [38] observed a stress plateau below 500 nm for Au films on Si with W interlayer. Only the pillars [65-67] exhibited a constant stress increase down to the smallest diameter of 200 nm. The films of this study only show a weak film thickness and grain size dependence, respectively, over the entire range from 57 to 847 nm.

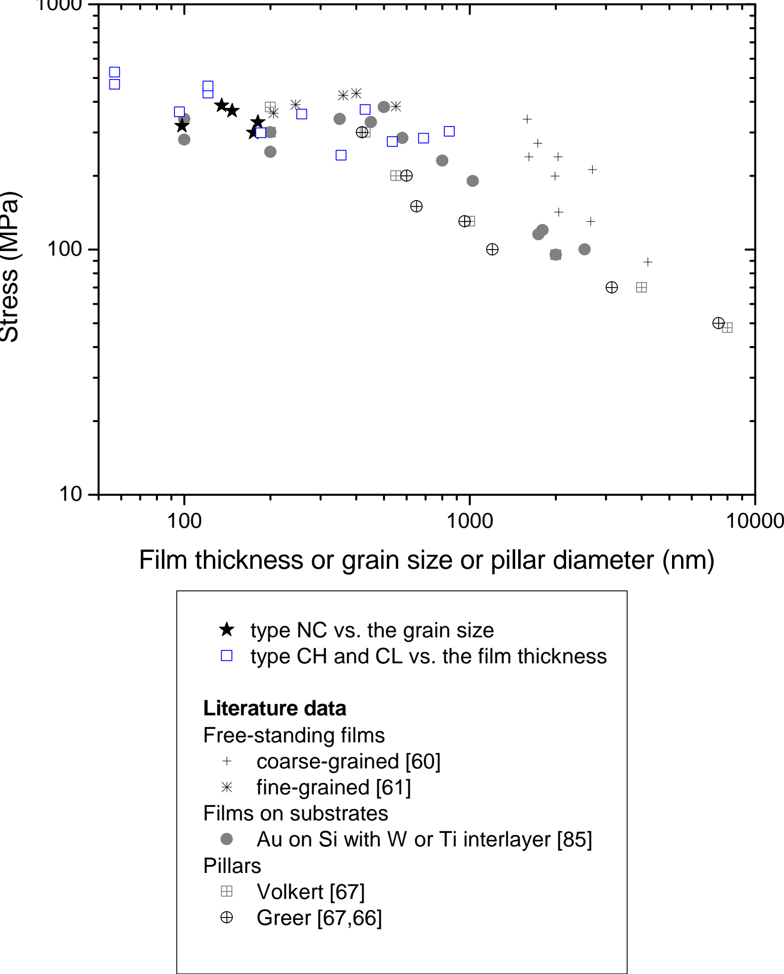

Fig. 3.28: Comparison of literature data of Au films on Si substrates with W or Ti interlayer [85], of free-standing Au films [60, 61] and of nano-sized Au pillars [65-67]. The data are plotted vs. the smallest dimension for each type of sample.

3.5 Summary and Conclusion

The thermomechanical behavior of thin Au films with different microstructures and film thicknesses was investigated. The different microstructures could be achieved by changing the deposition conditions:

- Coarse-grained Au films with the typical thin film microstructure, where the grain sizes were on the order of the film thicknesses, were fabricated by sputtering at a substrate temperature of 300 °C. The films had a broad texture and a substantial surface roughness. The film thicknesses were between 86 and 847 nm.

- Ultra-thin Au films between 57 and 121 nm with a columnar microstructure resulted from sputtering at room temperature. The grain sizes were also on the order of the film thicknesses, but the texture was narrow.
- Fine-grained, non-columnar films between 173 and 1738 nm thick, whose grain sizes were between 98 and 181 nm, were obtained by sputtering at room temperature. The grain heights were between 105 and 300 nm.

Besides elasticity, plastic deformation mediated by diffusional creep and dislocation glide was observed during thermal cycling to 500 °C and isothermal annealing. This was found to be independent of the film type, i.e. the microstructure and/or the film thickness. For diffusive stress relaxation at elevated temperatures, the following observations were made and the following conclusions were drawn:

- Parallel glide dislocations were observed for the first time in Au films.
- The simulation of stress-temperature curves with the formalism of constrained diffusional creep required the introduction of a threshold stress for the onset of creep to describe the heating portion of the experimentally measured stress-temperature curves for CH and CL type films. For CL type films, the experimentally measured stress-temperature curves could be described better, when the grain size used in the simulation was about 3-5 times the value of the measured grain size.
- Differences were observed in the stress-temperature behavior of type CL and CH films, although both contained parallel glide dislocations and had columnar grains. This led to the speculation that film properties, such as texture and surface roughness may influence diffusion and thus the stress-temperature behavior.
- A comparison with literature of thin Cu films reveal that Cu and Auf films both deform by constrained diffusional creep and show very similar stress-temperature curves in the ultra-thin film thickness regime.

At room temperature, dislocation plasticity was found to operate in all types of films:

- The films investigated in this study provided the first stress measurements of Au films below 100 nm in the ultra-thin regime.
- Compared to literature values, the stresses are very similar and independent of testing technique and sample geometry.

- The dependence of the stress on the film thickness and/or grain size is relatively weak.
- The smallest dimension of the film is plasticity-limiting. When plotted vs. the inverse grain size, the stresses of all films fell onto one line. This means that primarily the dimension and not the grain surrounding, e.g. the interface has the major impact on dislocation motion. However, the stresses of type NC films are close to the values that would be expected according to the Thompson model.

4 Hillock formation in non-columnar Au films

4.1 Introduction

For thin films, the surface plays a much greater role than for bulk materials, because the surface to volume ratio is significantly larger. At elevated temperatures, surface diffusion becomes hence important. Also, the grains are usually small in these films and thus grain boundary diffusion plays a major role. The most common testing technique for thin films, wafer curvature measurements, employs temperature changes to strain the metal film on a substrate. Microelectronics and micromechanics processing often requires annealing steps, which induce similar thermal stresses. In addition, the surface morphology could be altered severely by grooving, voiding and/or hillocking. The formation of hillocks and/or voids was reported in numerous metal films on substrates, e.g. Al [42-47], Al-Ta [55], Pb [40, 52], Zn [40], Ag [88, 89], Au [54, 68-70]. Many different models were developed to describe the observed hillock formation. They generally agree that hillocks form to relax compressive film stresses at elevated temperatures and that long-range material transport is needed to form the hillocks. This material transport was thought to occur by interfacial sliding [52], dislocation plasticity [41], diffusion along lateral grain boundaries [55], or grain boundary motion [28, 43].

In the particular case of hillock formation in thin Au films, it was further influenced by the interlayers that had to be introduced to provide for sufficient adhesion of the film to the substrate [68, 69]. Many different adhesion promoting materials were used and nearly all affected the surface morphological evolution, because they diffused into the Au film, reacted with it, segregated at the grain boundaries, and/or oxidized at the surface. Experiments with Ti, V, Cu, Sn, Ni, In [69] and Cr [68, 70] as interlayer materials were conducted and these elements diffused and reacted during annealing between 225 and 500 °C. Only Mo studied by Pennebaker [54] in 1969, is essentially immiscible in Au. However, the experimental techniques are much more sophisticated nowadays than in 1969.

In the present study, Au was deposited onto Si with an a-SiN_x diffusion barrier and adhered well to the substrate, so that additional effects due to reaction with a metallic interlayer material could be avoided. Furthermore, films with two different microstructures could be fabricated. The aim of this study was to investigate the

influence of microstructural parameters on the surface evolution. The focus was on hillock formation and on the identification of the hillock formation mechanism.

4.2 Film deposition and methods

Nine Au films with thicknesses between 57 and 1738 nm were DC magnetron sputtered at room temperature under ultrahigh vacuum conditions ($\leq 10^{-8}$ mbar) in a commercial sputtering chamber (DCA Instruments, Turku, Finland). Au was deposited onto (100)-oriented silicon wafers coated with 50 nm amorphous thermal silicon oxide and followed by 50 nm amorphous silicon nitride acting as diffusions barrier. Prior to Au deposition, the Au target (99.99%) and the substrates were cleaned by Ar^+ sputtering. The sputtering pressure was $< 10^{-8}$ mbar and a sputtering rate of 7 Å/s was used. Immediately after deposition, the samples were annealed in the sputtering chamber at 500 °C for 30 min to stabilize the microstructure. For comparison with the room temperature sputtered films, six samples with thicknesses between 173 and 847 nm were sputtered at a substrate temperature of 300 °C. Film texture was determined from θ-2θ X-ray scans and (111) pole figures were recorded with a Phillips diffractometer.

The thermomechanical behavior of the Au films was studied by the wafer curvature technique [6, 90]. The samples were usually thermally cycled three times between 50 and 500 °C at heating and cooling rates of 4 to 6 K/min. The sample curvature was recorded at 10 °C intervals. A 900 nm film was only cycled to 400 °C and annealed there for 240 min. The film stress can be calculated from the curvature according to Stoney's equation [91]:

$$\sigma_f = \frac{M_s \cdot h_s^2}{6h_f} \cdot \Delta K \tag{4.1}$$

where M_s is the biaxial modulus of the substrate, h_s is the substrate thickness, h_f is the film thickness, and ΔK is the change in curvature.

A CamScan SC44 SEM equipped with a heating stage was used to thermally cycle an 870 nm thick Au film to 500 °C and anneal another at 420 °C for 220 min. The heating rates were between 2 and 5 K/min to be consistent with the wafer curvature measurements. The temperature, however, could only be measured inside the heating

block, onto which the sample was mounted with silver paint. Therefore, the sample temperature may be lower during heating and annealing. When presenting the results, the temperatures measured in the heating block are used. The evolution of the surface morphology, especially hillock formation and growth were monitored *in situ.*

The film surface was investigated before and after thermal cycling with an SEM (LEO 1530 VP). The morphology of the films was usually examined after three thermal cycles to 500 °C. For the 870 nm thick Au film, however, the surface was examined after each of the three cycles. For the films sputtered at 300 °C, the SEM images were also used for grain size analysis. Images were recorded with a secondary electron detector located in the column, which made the grain boundary grooves visible. The grain boundary traces were manually redrawn onto a transparency and scanned in order to determine the grain area using commercial software (Quantimet Q500/W, Leica). All grain sizes correspond to the diameter of circle having the same area as the measured one. At least 350 grains were evaluated per film. Hillock areas and densities could also be determined from these micrographs by similar method. The hillock density was determined from an area of at least 75 x 75 μm^2. Between 26 and 113 hillocks were counted for each film. The mean hillock area was determined by tracing the hillock contours onto a transparency and evaluating them by using the same software as for the grain size analysis.

An FEI 200xP FIB was used to investigate the film and hillock microstructure by cutting cross-sections and imaging the grain structure. The contrast is due to different channeling probabilities of ions in differently oriented grains. When ions channel deeper into the material, they induce fewer secondary electrons and the grains appear darker.

Plan-view and cross-sectional TEM investigations of the film microstructure were carried out in a JEOL 2000 FX operated at 200 kV and a JEOL 4000 EX operated at 400 kV. For plan-view characterization, the wafer was mechanically polished to approximately 80 microns from the backside, dimpled, and chemically etched with an $HF/HNO_3/CH_3COOH$ mixture at room temperature. For Au films thicker than 100 nm ion milling was necessary to produce electron transparency. Sets of micrographs at different tilt angles and magnifications were taken for grain size evaluation and processed the same way as for the films sputtered at 300 °C. At least 220 grains were measured for each sample. For cross-sectional evaluation, the films were glued face-to-face, sandwiched between two pieces of silicon for mechanical stability, and then sliced.

These slices were mechanically ground, polished, dimpled, and finally ion milled to obtain an electron transparent film. To prepare a hillock cross-section, an FEI Nova Nanolab dual beam microscope that has an electron and a focused ion beam was employed. Details of the preparation method are given in [92].

4.3 Au microstructure and thermal stresses

The microstructure of the samples as a consequence of different deposition conditions will be described in the following section. Also, an overview on the macroscopic stress-temperature behavior of the films will be given.

4.3.1 Film microstructure

The films sputtered at room temperature and 300 °C yielded different microstructures. In addition, within the films sputtered at room temperature, two types of films can be distinguished.

Cross-sectional TEM images of the 121, 265 and 890 nm thick films sputtered at room temperature are shown in Fig. 4.1a-c. The 121 nm thick and all thinner films have columnar grains extending through the entire film thickness. All thicker films (see e.g. the 265 and 893 nm thick films in Fig. 4.1b-c) have grain boundaries and twins parallel to the film/substrate interface with increasing number of grains for thicker films. They will be referred to as non-columnar. The TEM cross-sections were also used to measure the actual film thicknesses.

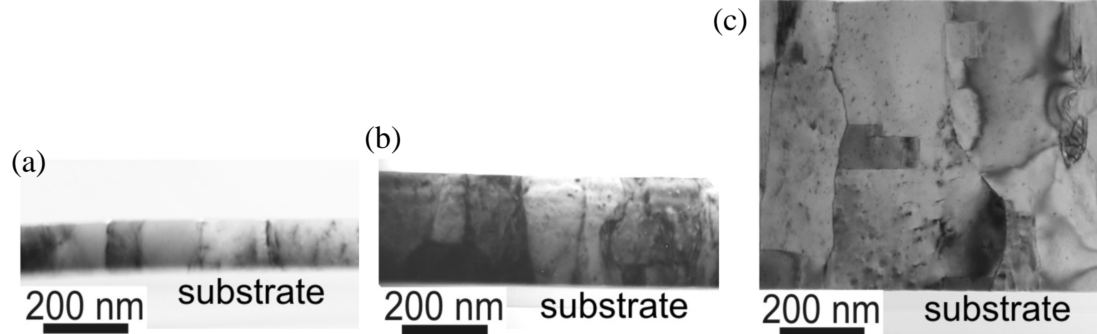

Fig. 4.1: Microstructure of the RT deposited films. Cross-sectional TEM micrographs of (a) a 121 nm, (b) a 265 nm, and (c) an 893 nm thick Au film. The 121 nm thick film has columnar grains, whereas the two other films exhibit twins and grain boundaries parallel to the film/substrate interface.

Plan-view TEM images in Fig. 4.2 or the 121 and the 870 nm thick Au films show that the median grain sizes remain very small, even when the film thickness increases. For the 121 nm thick Au film, it is 83 nm and for the 870 nm thick Au film it is 176 nm. The grain sizes of all room temperature sputtered samples fall between 69 and 185 nm with predominantly lognormal grain size distributions. (111)-pole figures and rocking curves reveal tight (111)-fiber textures with the FWHM = (3.7 ± 0.2)° for all room temperature sputtered films.

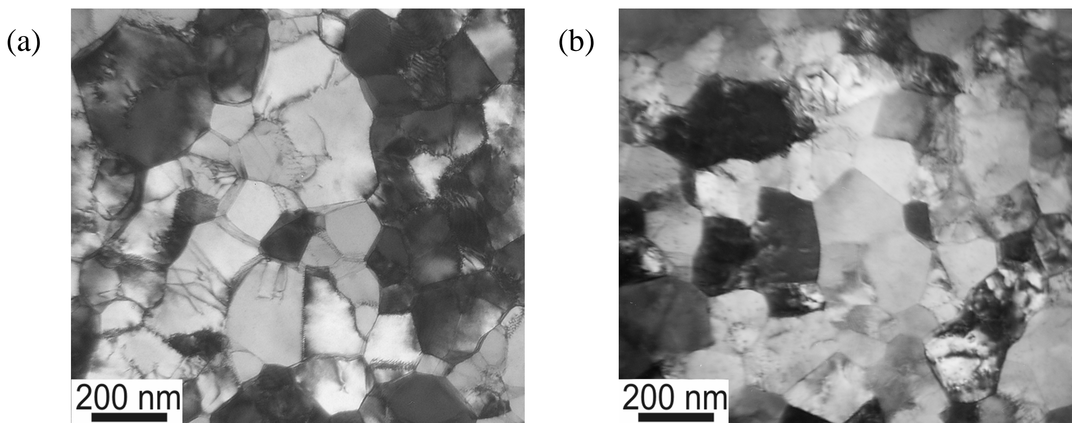

Fig. 4.2: Microstructure of the room temperature deposited samples from plan-view TEM images. (a) a 121 nm thick Au film with a median grain size of 83 nm and (b) an 870 nm thick films with a median grain size of only 175 nm.

The films sputtered at 300 °C exhibit a predominantly columnar grain structure with the median grain size value on the order of the film thickness, as more commonly observed. The two thickest films (688 and 847 nm thick) have some grains that do not extend through the entire film thickness as seen in Fig. 4.3 for the 688 nm thick film. All films have twin boundaries parallel to the substrate similar to the 688 nm thick film. The (111)-fiber texture of these films is broader than for the room temperature deposited samples with the FWHM ranging from 10.9 ± 0.2° to 13.1 ± 0.2°.

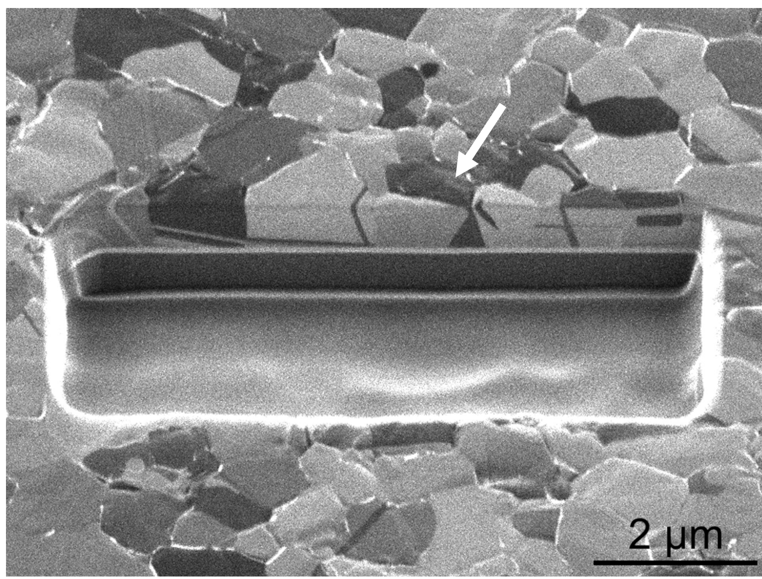

Fig. 4.3: The cross-section of the 688 nm thick Au film sputtered at 300 °C was prepared and imaged under a 40 ° tilt angle employing the FIB. The arrow points to a grain that is non-columnar. All other grains are columnar with some exhibiting twins parallel to the film/substrate interface.

As seen above, the films sputtered at room temperature can be divided into two groups: (i) ultra thin films ($h_f \leq 121$ nm) that have a columnar grain structure and grain sizes on the order of the film thickness, and (ii) thicker films which have additional grain boundaries parallel to the film/substrate interface and grain sizes much smaller than the film thickness. The films sputtered at 300 °C have columnar grains, whose size is about the film thickness. The samples are listed in Table 4.1.

Table 4.1: The microstructure of the samples that were deposited at two different temperatures.

Film thicknesses	57 to 121 nm	265 to 1738 nm	185 to 847 nm
Deposition temperature	room temperature	room temperature	300 °C
Microstructure	columnar	non-columnar	columnar
Grain size	$1.2 \cdot h_f$	98 to 181 nm	$1.2 \cdot h_f$
# of samples	5	7	7

4.3.2 Stress-temperature behavior

The stress-temperature behavior as measured from wafer curvature is shown in Fig. 4.4a-c for the three different types of films. For the 870 nm thick non-columnar Au film (Fig. 4.4a), the starting stress of the first cycle is slightly lower than the stress at the end of the cycle, whereas starting and final stresses are the same for the second cycle and all subsequent cycles. After film deposition and before testing, the stress had relaxed at room temperature. The film is in a tensile stress state at room temperature and follows a thermoelastic line. The deviation from the linear behavior occurs at a slightly lower temperature during the first than during the second cycle, because the starting stress of the first cycle is lower. At 320 °C, the curves of both cycles join each other and the compressive stress slightly relaxed to 500 °C. However, this relaxation is so small that it is within the errors of the measurement, such that it also can be considered as a stress plateau. Upon cooling a very short elastic regime is observed, followed by two plastic regimes in tension, where the high-temperature one has a shallower slope than the low-temperature one. The stress-temperature curves of the other non-columnar films look similar (for more details see chapter 3.3.2.1). The thinner columnar films ($h_f \leq$ 121 nm) sputtered at room temperature do not exhibit the stress plateau during heating as shown in Fig. 4.4b, but instead the stress increases further until 500 °C. During unloading, thermoelastic behavior proceeds compressive until at least 450 °C and then plasticity occurs. Finally, the 688 nm thick columnar Au film sputtered at 300 °C also follows a thermoelastic line during cooling until a stress plateau is reached (Fig. 4.4c). No thermoelastic unloading is observed during cooling, but plastic stress relaxation occurs down to room temperature. This stress-temperature curve is typical for all columnar films sputtered at 300 °C. The stress relaxation that takes place during the heating portion of a thermal cycle can be estimated from the difference of the measured stress in the film at 500 °C and the stress obtained by extrapolating the thermoelastic line to 500 °C as shown in Fig. 4.4. For the 870 nm thick Au film, the stress relaxed during the second cycle is thus 370 MPa. The stress relaxed during the second cycle of the 121 nm thick film was 410 MPa and for the 688 nm thick columnar Au film 520 MPa were relaxed.

(a)

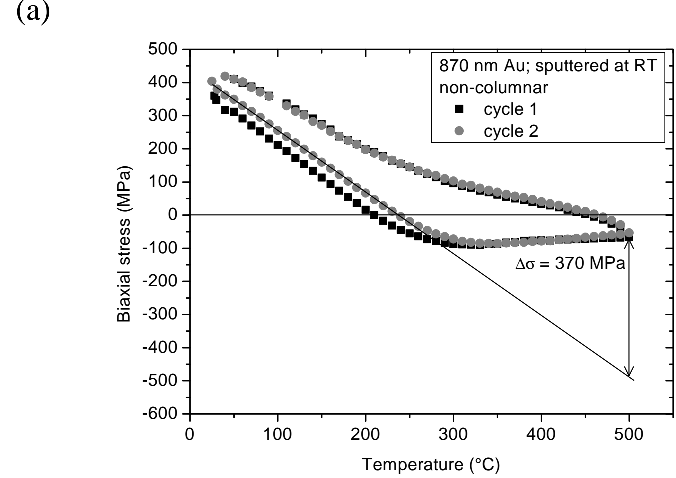

(b)

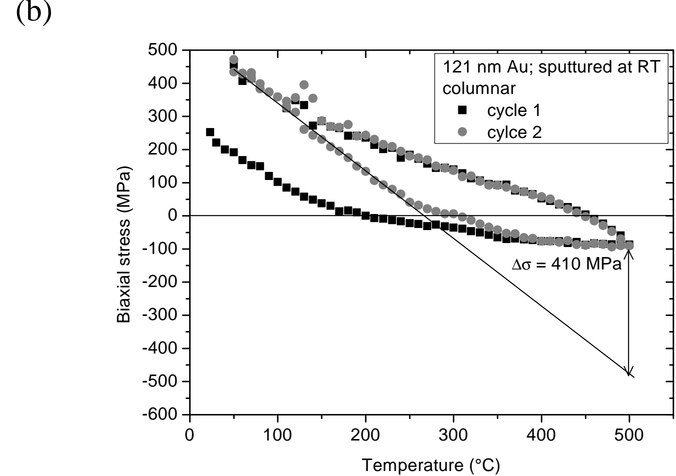

(c)

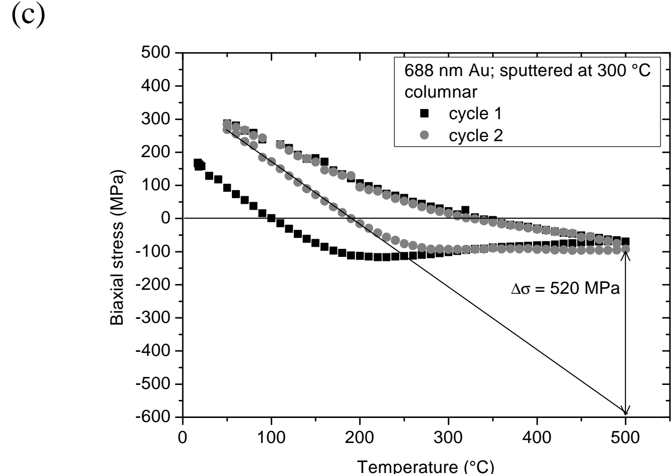

Fig. 4.4: Stress-temperature behavior of (a) an 870 nm thick and (b) a 121 nm thick Au film sputtered at room temperature. (c) depicts the stress of thermal cycling for a 688 nm thick Au film sputtered at 300 °C. In all plots, the stress relaxation during the second cycle is given by extrapolation of the thermoelastic line to 500 °C and subtracting the measured stress at that temperature.

The compressive stress relaxation of the 900 nm thick film during isothermal annealing at 400 °C is shown in Fig. 4.5. First, the compressive stress decreases rapidly and eventually after about 50 min a constant stress is reached. The fitting parameters are given in plot.

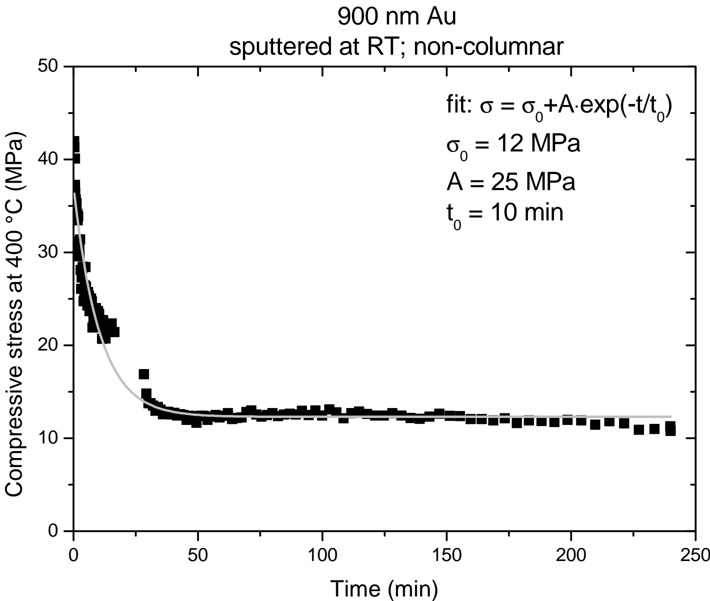

Fig. 4.5: Compressive stress relaxation during annealing at 400 °C. The curve could be fitted by an exponential decay with a threshold stress.

4.4 Hillocks

Thermal cycling has different effects on the surface morphology evolution for non-columnar and columnar films, independent of the film deposition temperature of the columnar films. Initially, all films deposited at room temperature formed only grain boundary grooves after annealing at 500 °C (e.g. see the 870 nm thick Au film in Fig. 4.6). After three thermal cycles, however, the room temperature deposited 870 nm thick non-columnar Au film exhibited numerous voids and hillocks (Fig. 4.7). The branched void shape suggests that they nucleated at triple junctions and grew along the grain boundaries. Also, hillocks are often bounded by voids. This morphology is typical for all non-columnar films. On the other hand, a 121 nm thick, room temperature deposited columnar Au film only exhibited grain boundary grooves and some voids, but no hillocks after three thermal cycles (Fig. 4.8). The other ultra-thin columnar films sputtered at room temperature, with thicknesses of 57 and 96 nm, had a similar surface profile after three thermal cycles. The predominantly columnar films sputtered at 300 °C only exhibited hillocks for the two thickest films (688 and 847 nm Au), which possessed some grains that did not extend through the entire film thickness.

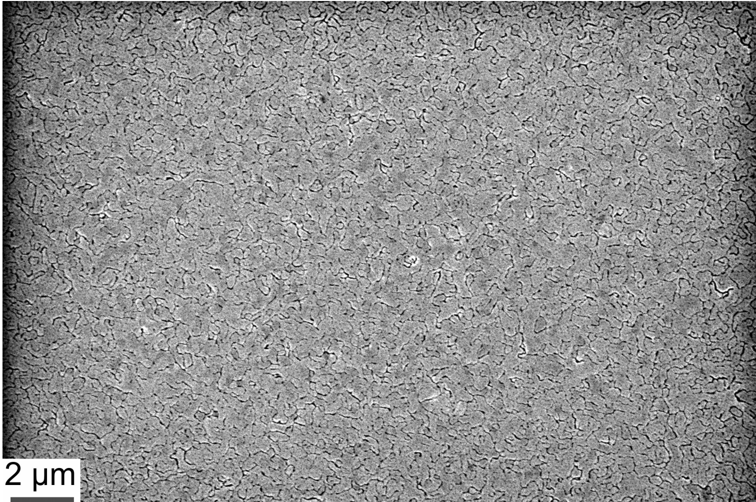

Fig. 4.6: Surface of an 870 nm thick non-columnar Au film after deposition at room temperature and annealing for 30 min at 500 °C. The grain boundaries are grooved.

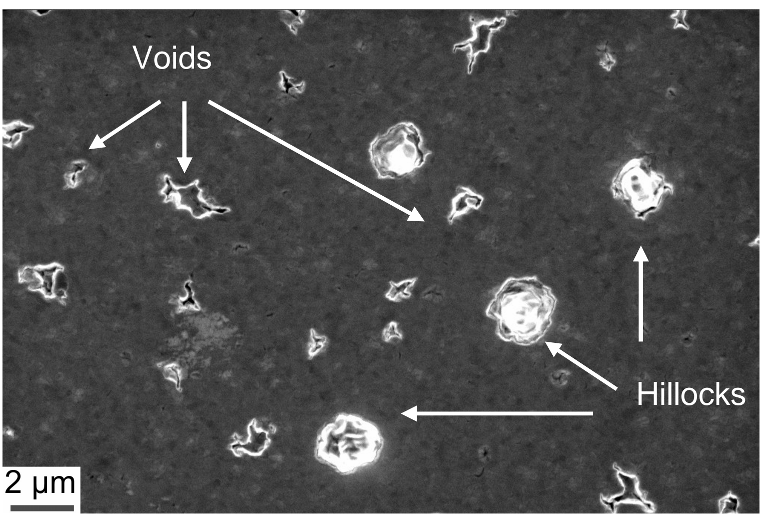

Fig. 4.7: Surface of an 870 nm thick Au non-columnar film after three thermal cycles to 500 °C. Hillocks and voids are clearly visible. Some voids and hillocks are marked in the image.

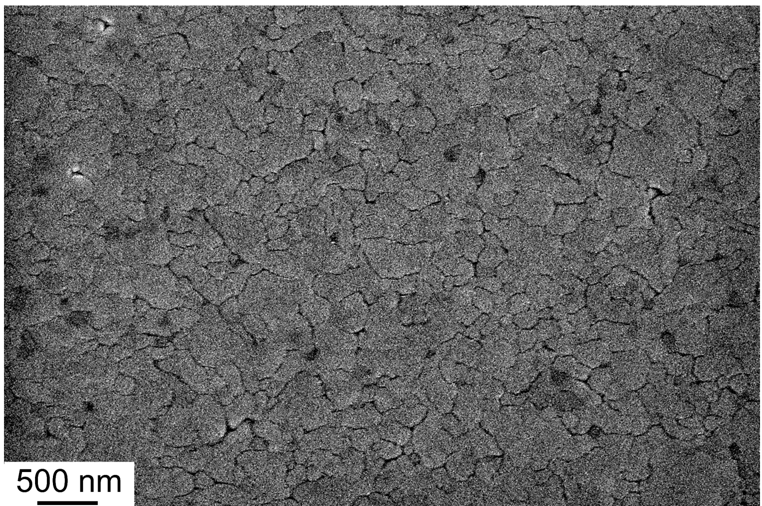

Fig. 4.8: Surface of a columnar 121 nm thick Au film after three thermal cycles to 50 °C. Only grain boundary grooves and some voids are visible.

In summary, only the non-columnar films with grain boundaries parallel to the film/substrate interface were prone to hillock formation. Films with a columnar microstructure were basically resistant to hillock formation and only grain boundary grooves and voids were observed.

4.4.1 Hillock microstructure

Fig. 4.9 shows a TEM cross-section of a hillock in a 1154 nm thick Au film after seven thermal cycles. The hillock is composed of several grains, which have a much larger grain size than the surrounding matrix. Voiding is not observed around this particular hillock.

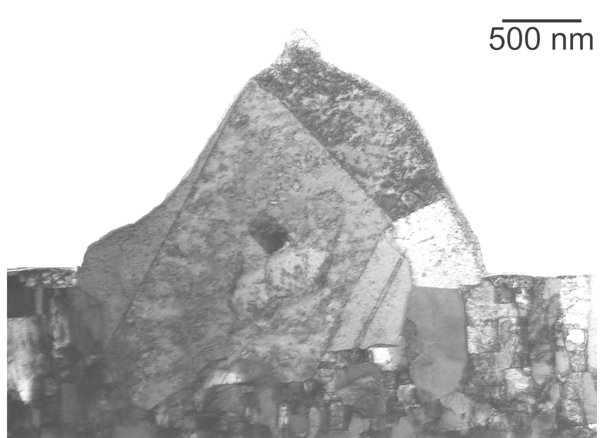

Fig. 4.9: Cross-sectional TEM of a hillock in a 1154 nm thick non-columnar Au film after seven thermal cycles. The hillock is composed of several grains, which are significantly larger than the grains in the film.

FIB studies for different film thicknesses show that the microstructure of Fig. 4.9 is typical for the hillocks. In Fig. 4.10 and Fig. 4.11 the cross-sections from a 469 and an 870 nm thick Au films also show hillocks composed of several grains, some of which are twinned. These micrographs further suggest that the hillock height above the film surface is roughly half of the hillock diameter. Note that the image is taken at a tilt angle of 45°, so that the hillock is distorted. Hillocks exhibit various shapes; some look hemispherical (e.g. see Fig. 4.11), while others as seen in Fig. 4.10 are cone-like. The hillocks do not always extend through the entire film thickness. None of the micrographs revealed any pores or delamination of the film.

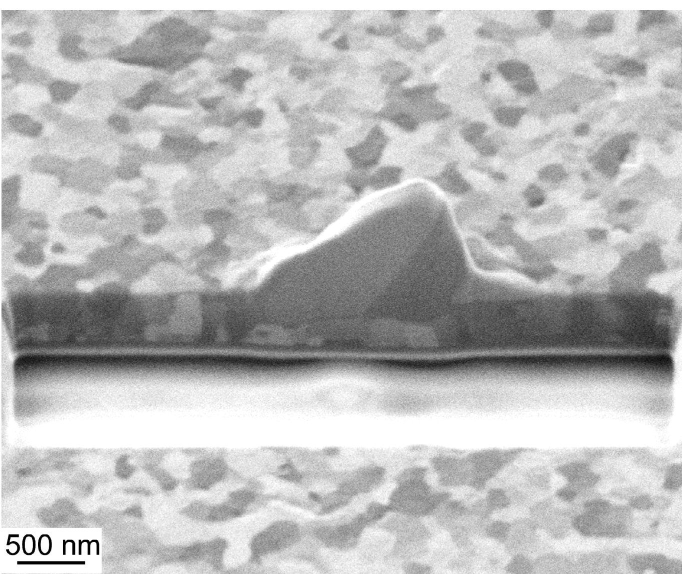

Fig. 4.10: Hillock cross-section by FIB in a 469 nm thick Au film at a tilt angle of 45 °. The hillock does not entirely extend to the film/substrate interface and has a cone-like shape.

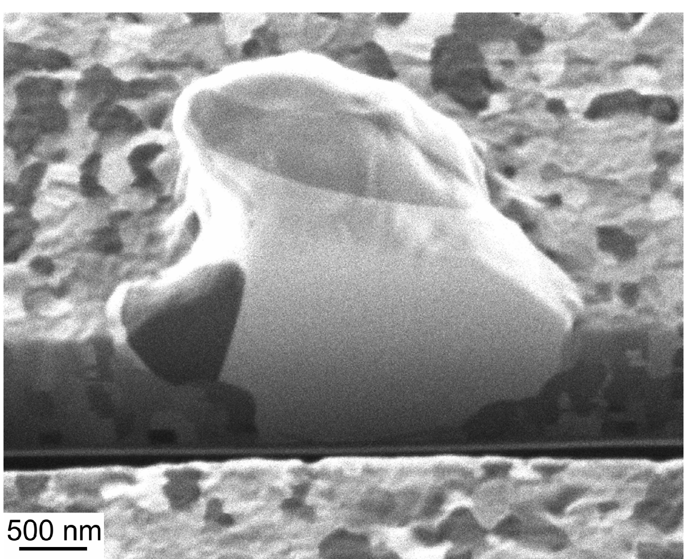

Fig. 4.11: The cross-section of a hillock in a 1154 nm thick Au film at a 45° tilt prepared and imaged by FIB. The hillock reaches the film/substrate interface.

As seen in Fig. 4.10 and Fig. 4.11, cones and hemispheres can be regarded the extreme shapes of the hillocks. Many hillocks exhibit features of both. Therefore, the volume is estimated by the average of the volume calculations for a cone and a hemisphere. The volume V_{HS} of a hemisphere with the radius R is given by:

$$V_{HS} = \frac{2}{3}\pi R^3 \tag{4.2}$$

And the volume V_C of a cone with the height $H = R$ is:

$$V_C = \frac{1}{3}\pi R^3 \tag{4.3}$$

The average, which will be used for hillock volume calculations:

$$V_{hill} = \frac{1}{2}\pi R^3 \tag{4.4}$$

For example the radius of the hillock in

Fig. 4.10 is about 880 nm, which yields a volume of 1.07 µm^3. The statistical data for further analysis of the hillock volumes are presented in the next section, where the SEM images are evaluated.

4.4.2 Hillocks statistics

The hillock densities and the median basal areas after three thermal cycles for film thicknesses between 265 and 1738 nm are plotted in Fig. 4.12. The hillock density increases with film thickness, except for the 640 nm thick Au film, which has an exceptionally high hillock density. The 469 nm thick film, on the other hand, has a lower hillock density. For the density measurements the areas investigated were between 5840 and 18900 µm^2 and for each sample at least 35 hillocks were counted. The error of the analysis shown in Fig. 4.12 is due to hillocks that may have been overlooked or features that were erroneously identified as hillocks. For each analysis this could possibly be about 10 %, assuming that the area is representative of the whole sample. Measurements were always made in the middle of the wafer, because near the edge, the hillock density seemed to be larger. The hillock areas, based on measurements of at least 32 hillocks per sample, vary strongly and no really systematic trend can be observed. Here, the error is more complex, since an incorrect redrawning of the outer boundaries of the hillock onto the transparency is possible. This error is hard to

estimate, but independently repeated analysis of the same images suggested it is about 10 %.

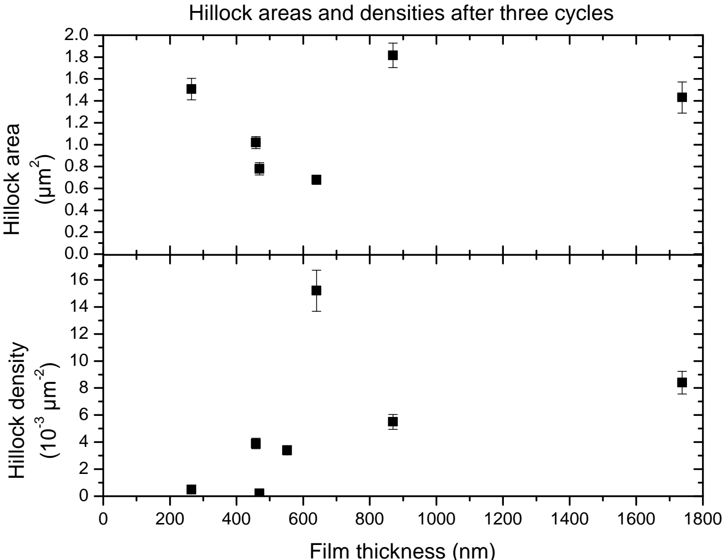

Fig. 4.12: Hillock densities and hillock areas after three thermal cycles to 500 °C in the wafer curvature machine for various film thicknesses. The densities increase with decreasing film thickness, while the areas do not vary systematically with film thickness.

The hillock density was also measured for the 870 nm thick film after the first, second and third thermal cycle. It increased with the number of cycles (Fig. 4.13), with new hillocks formed during each cycle.

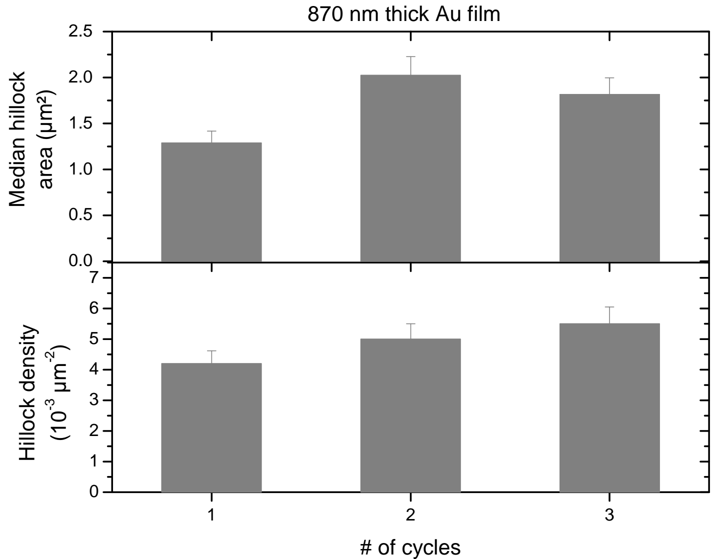

Fig. 4.13: Hillock densities after the first three cycles for an 870 nm thick Au film. The hillock densities increase with the number of cycles, while the hillock areas remain constant between the second and third cycle.

Most hillocks appeared during the first cycle and the hillock densities were $4.2 \cdot 10^{-3}$ μm^{-2}, $5.0 \cdot 10^{-3}$ μm^{-2} and to $5.5 \cdot 10^{-3}$ μm^{-2} after the first, second and third cycle, respectively. The median hillock area increased between the first and the second cycle, but remained basically constant when the film was cycled a third time.

The hillock sizes distributions were also analyzed. For each film thickness, the frequency of hillocks with a particular area after three thermal cycles is plotted in Fig. 4.14. Although the hillock statistics for some film thicknesses are low, some observations can still be made. The distribution of hillock areas is wider for thicker films than for the thinner films. A Shapiro-Wilk test [93], which examines whether a normal distribution is given, revealed that films thinner than 640 nm have a normal distribution when a significance level of 0.05 is considered.

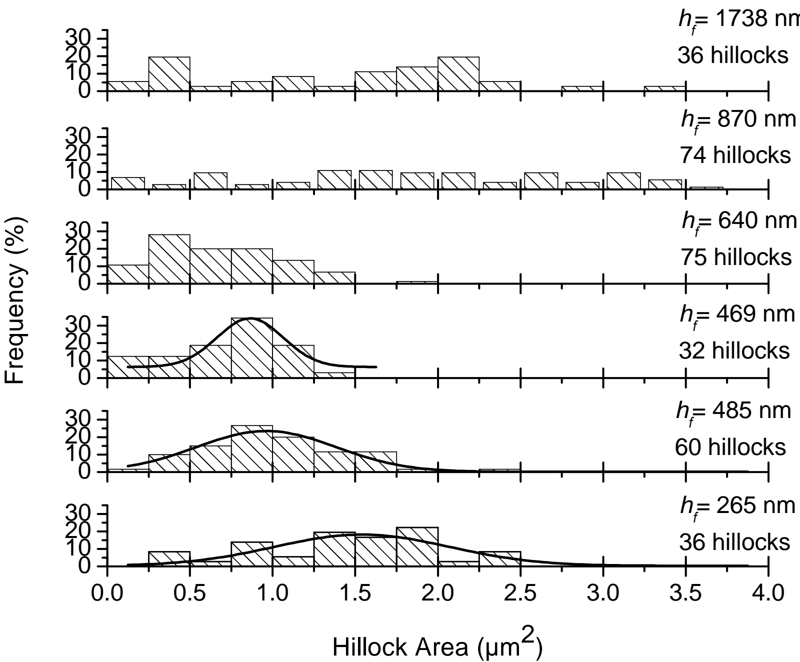

Fig. 4.14: Hillock area distributions after three thermal cycles for all measured film thicknesses. The hillock distributions for films < 640 nm are approximated as normal by the Shapiro-Wilk test [93] for a significance of 0.05. The Gaussian fits are also included in the plot.

The distribution of hillock area also changes with the number of cycles for the 870 nm thick film (Fig. 4.15). After the first cycle, there is still a normal distribution, while after subsequent cycles; this distribution becomes much broader and is no longer Gaussian.

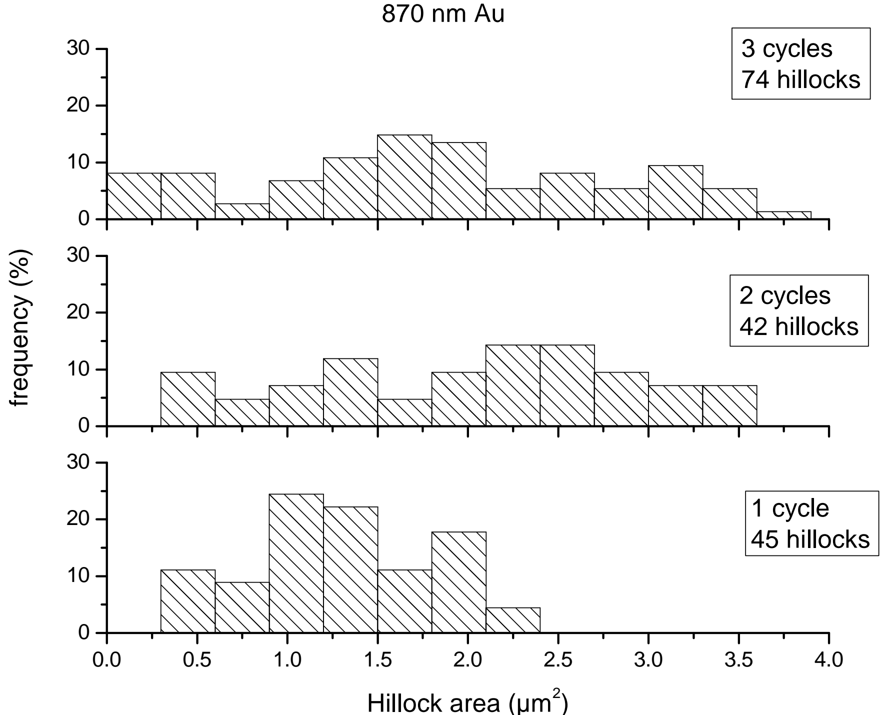

Fig. 4.15: The distribution of the hillock areas of an 870 nm thick film after subsequent thermal cycling. After the second cycle, the distribution has become much broader than it was after the first cycle.

4.4.3 Hillock growth during thermal cycling

The *in situ* heating cycles in the SEM revealed that new hillocks nucleated and existing hillocks grew between 300 und 400 °C. Fig. 4.16 shows a sequence from a second heating cycle of an 870 nm thick Au film. The first image taken at 350 °C shows no hillocks. At 400 °C a hillock had already formed and continued to grow up to 450 °C, but not during further heating to 500 °C. During cooling, however, the hillock did not disappear or shrink as is seen in Fig. 4.16. The stresses measured from the wafer curvature experiments of a comparable sample are also given in the images.

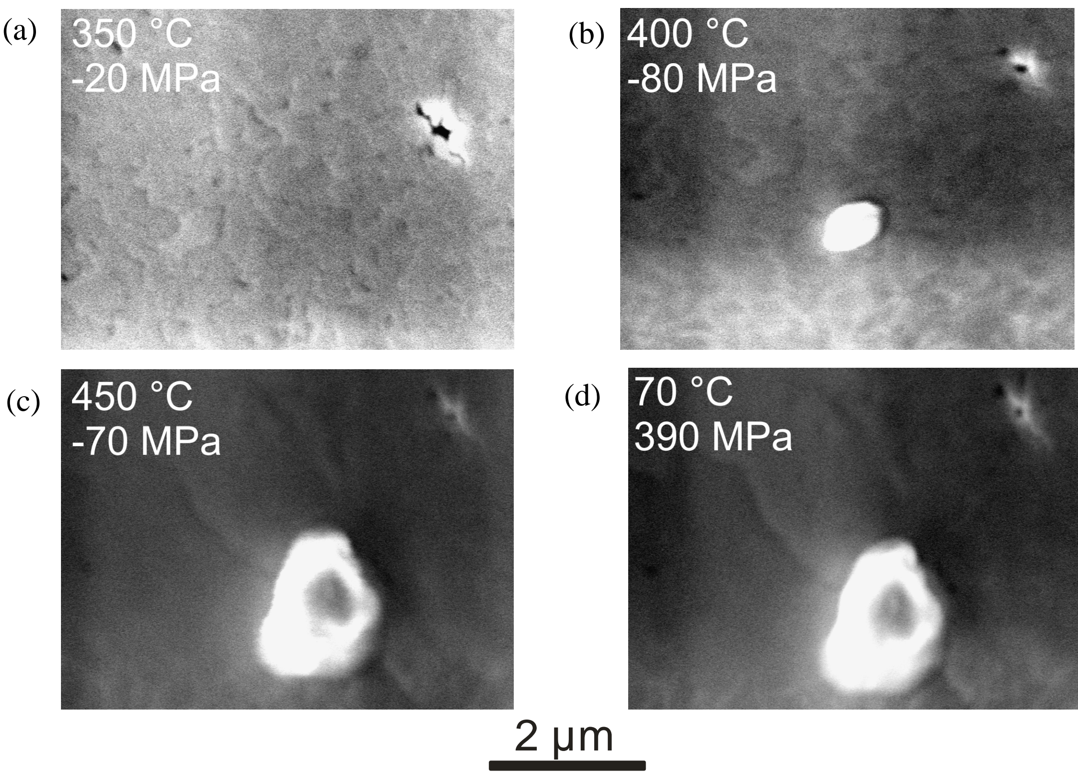

Fig. 4.16: Second *in situ* thermal cycle of an 870 nm thick Au film in an SEM: (a) at 350 °C, (b) first hillock observed at 400 °, (c) hillock growth up to 450 °C, (d) hillock after cooling to 70 °C.

4.4.4 Hillock growth during isothermal annealing

In a further *in situ* experiment, hillock growth was investigated at a constant temperature of 420 °C for the 870 nm thick Au film. 420 °C was high enough to observe substantial hillock growth and was tolerated by the equipment over a longer period of time. Although, the hillocks initially formed between 350 and 400 °C, hillock

growth was only evaluated from the moment that the annealing temperature of 420 °C was reached, which was 100 min after the cycle had started and 10 min after the first hillocks were observed. In Fig. 4.17a-d the hillock is depicted at four different times: after 4, 24, 62 and 213 min. The first image (a) was recorded just after the film reached 420 °C. Significant growth is observed after 24 and 62 min. In the last time interval (up to 213 min) the hillock still grew, but much less than in the previous intervals.

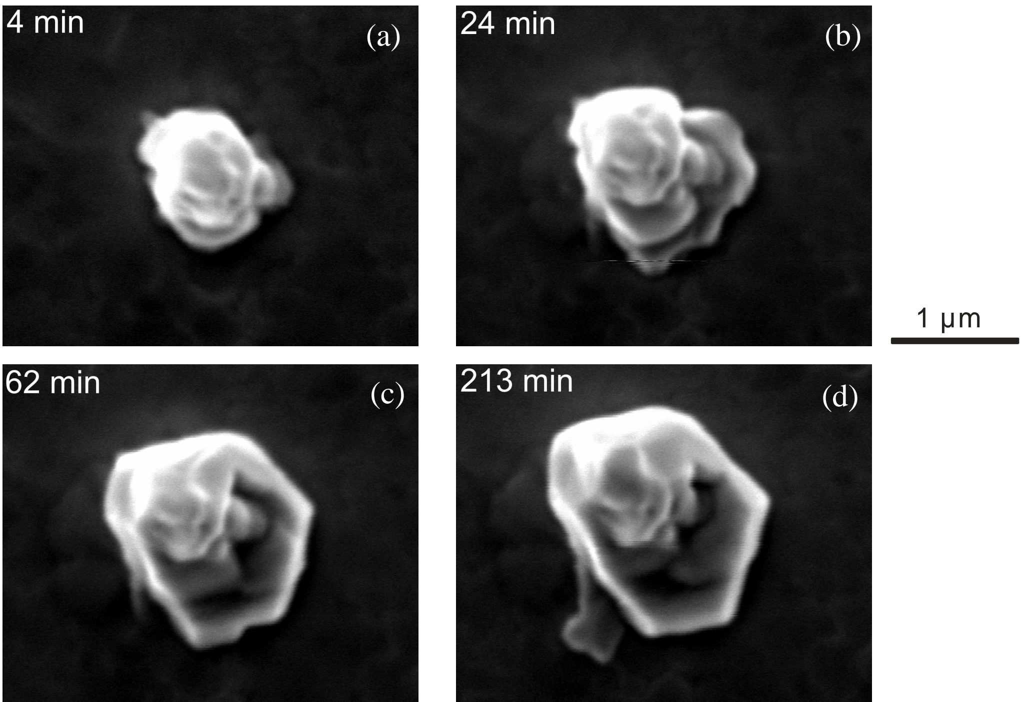

Fig. 4.17: *In situ* SEM images of annealing at 420 °C monitoring hillock growth: (a) after 4 min, (b) after 24 min, (c) after 62, and (d) after 213 min.

Three other hillocks were also monitored during the annealing and their areas are plotted as a function of time in Fig. 4.18. Hillock A is the one shown in the micrographs in Fig. 4.17. Hillock B emerged between 350 and 420 °C, while for hillocks C and D it is not known at which temperatures and/or time they formed. The time was set to be 0 min when 420 °C was reached.

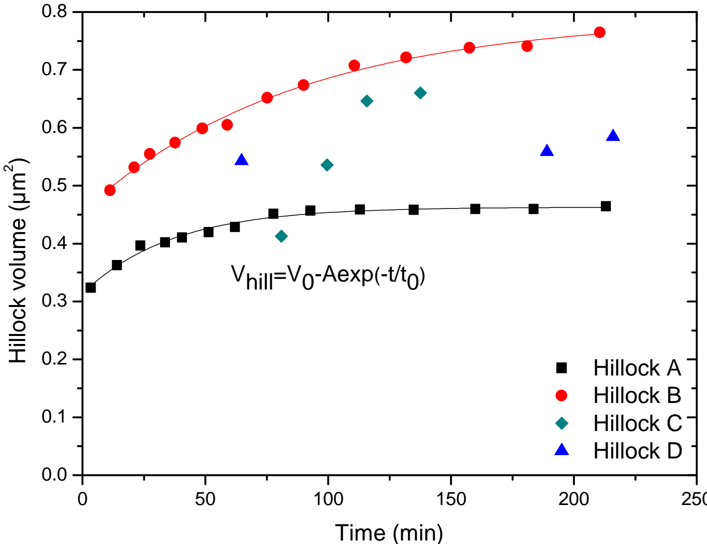

Fig. 4.18: Growth of different hillocks at 420 °C investigated by *in situ* SEM. The hillock volume was calculated according to eq. (4.4) from the measured hillock area.

The volume of the hillocks is estimated from the areas using eq. (4.4). The increase of the hillock volume over time can be fitted by an exponential function:

$$V_{hill} = V_0 - A \cdot \exp\left(-\frac{t}{t_0}\right) \qquad (4.5)$$

where t is the time, t_0 a characteristic time constant, A a constant and V_0 the final volume of the hillock. The parameters of the two fits are given in Table 4.2.

Table 4.2: Parameters of the exponential fits in Fig. 4.18.

	V_0 (µm³)	A (µm³)	t_0 (min)
hillock A	0.463 ± 0.003	0.149 ± 0.006	36 ± 3
hillock B	0.7921 ± 0.013	0.337 ± 0.009	87 ± 8

4.5 Discussion of hillock formation

Kinetics and thermodynamics have to be considered to understand the reasons for and mechanisms of the hillock formation during thermal cycling in thin metal films on rigid substrates. Potential transport mechanisms that may lead to material accumulation will be discussed in light of the film microstructure. Since it is generally accepted that the driving force for hillock formation is compressive stress relaxation [44, 47, 52-54], the stresses relaxed by the hillocks will be compared with the macroscopic stress-temperature measurements.

4.5.1 Hillock formation mechanisms

Material transport can occur by diffusion or dislocation plasticity. Dislocation motion, however, is not very likely in the non-columnar films that form hillocks, because TEM images (see e.g. Fig. 4.1, 4.2 and 4.9) revealed hardly any dislocations in the film. Furthermore, if dislocations were responsible for material transport, columnar films would be expected to form hillocks as well. The experiments, however, revealed that only *non-columnar* films were susceptible to hillock formation. Moreover, hillocks were first observed between 300 and 400 °C by *in situ* SEM. In this temperature range at least grain boundary and surface diffusion were active (T_m[K]/3 ≅ 173 °C). A third potential diffusion path could be the film/substrate interface. This is very unlikely, as FIB cross sections showed that many hillocks do not reach down to the film/substrate interface, especially in thicker films (e.g. see Fig. 4.9 and 4.10). Also, no pores or delamination were observed at the interface. Table 4.3 lists the diffusion pre-factors, and the activation energies for bulk, grain boundary and surface diffusion. To estimate diffusivities and diffusion distances during thermal cycling, it is assumed that diffusion operates between 250 and 500 °C. The average diffusivities in this temperature range were obtained by integrating the diffusivities between 250 and 500 °C and dividing the result by 250 K. The resulting values are given in Table 4.3. The grain boundary diffusivity, δD_{gb}, contains additionally the grain boundary width, δ. Considering that diffusion only occurred along the grain boundary, but not in the adjacent grain, it had to be divided by the grain dimension, to obtain an effective diffusivity that can be compared to other diffusivities as bulk or surface diffusivity. The value for the average diffusivity between 250 and 500 °C was normalized by a grain height of 300 nm as obtained from cross-sectional TEM (Fig. 4.9). This grain height is the upper limit, and

thus the diffusion coefficient is the lower limit. The average diffusion distance x can be estimated by:

$$x \approx \sqrt{2Dt} \tag{4.6}$$

where t is the time. Heating from 250 to 500 °C in the wafer curvature experiment takes 2500 s at a heating rate of 6 K/min.

Table 4.3: Diffusivities and estimates of diffusion distance for bulk, grain boundary and surface diffusion. The diffusivities were averaged between 250 and 500 °C. For the grain boundary diffusion, it was additionally normalized by a grain height of 300 nm.

bulk diffusion	grain boundary diffusion	surface diffusion
$D_{0,b} = 9\cdot10^{-6}$ m²/s	$\delta D_{0,gb} = 3\cdot10^{-11}$ m³/s	$D_{0,s} = 3\cdot10^{-16}$ m²/s
Q_b = 173 kJ/mol	Q_{gb} = 85 kJ/mol	Q_s =62 kJ/mol
[94]	[95]	[96]
average diffusivity between 250 to 500 °C $\overline{D}_b = 2.0\cdot10^{-18}$ m²/s	average diffusivity between 250 to 500 °C $\delta\overline{D}_{gb}/d_h = 4.5\cdot10^{-16}$ m²/s with d_h = 300 nm	average diffusivity between 250 to 500 °C $\overline{D}_s = 5.2\cdot10^{-16}$ m²/s
diffusion distance between 250 and 500 °C $\overline{x}_b = 0.1$ µm	diffusion distance between 250 and 500 °C $\overline{x}_{gb} = 1.5$ µm	diffusion distance between 250 and 500 °C $\overline{x}_s = 1.7$ µm

Bulk diffusion between 250 and 500 °C is two orders of magnitude slower than grain boundary and surface diffusion. The latter two have about the same value, when a grain dimension of 300 nm is assumed. Hence, material transport for hillock formation is most likely accomplished via grain boundary and/or surface diffusion. In the literature, long-range material transport was identified as one of the key factors in hillock formation [40, 41, 43, 52, 55] to move a sufficient amount of material to the site of the hillock. Two mechanisms can now be proposed: (i) diffusion of material from the film interior to the surface along the vertical grain boundaries followed by surface diffusion as a long-range material transport. This is schematically shown in Fig. 4.19a. (ii) diffusion along the network of the horizontal grain boundaries as the in-plane, long-range material transport mechanism followed by diffusion along the vertical grain boundaries, which is illustrated in Fig. 4.19b.

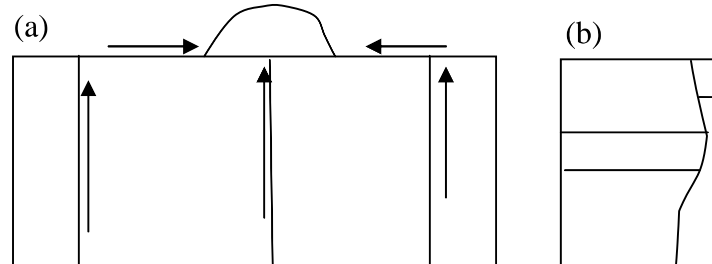

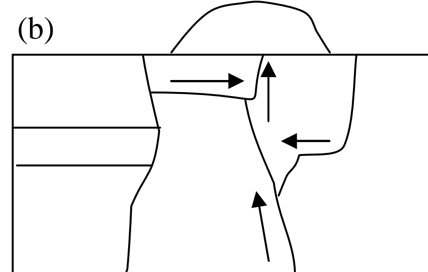

Fig. 4.19: Schematic illustration of the two possible mechanisms for hillock formation: (a) material diffuses along the vertical grain boundaries to the surface, on which it further diffuses to the hillock. (b) material diffuses along the horizontal, in-plane grain boundaries and along the vertical grain boundaries to the film surface. The second mechanism acts most likely in the non-columnar Au films, whereas columnar films did not exhibit hillocks.

That the columnar films do not form hillocks favors the second mechanism; where horizontal grain boundaries form long-range diffusion networks in the non-columnar films. Diffusion along the surface does not seem to be effective enough to bring a significantly amount of material to one site. The analysis of Al-Ta films by Iwamura *et al.*[55] also predicted that larger hillocks only emerge if lateral diffusion in the film is possible due to small grains. However, for columnar Al-Ta films large-grained films, a high density of small hillocks was predicted and observed. The columnar large-grained Au films of this study, in contrast, did not show small hillocks. The material could potentially be redistributed on the free surface, as opposed to Al, which has a native oxide.

Material flux divergences must occur to nucleate hillocks. Triple junctions are most likely locations of such flux divergences and hillocks presumably nucleate at triple junctions at or close to the surface, from where they grew both above the film surface and towards the interface. Because of the small grain size, the non-columnar films also offer many triple junctions as potential nucleation sites, so that it is more likely to find a site of good flux divergence.

The grain size of the hillocks greatly exceeds that of the surrounding matrix and they often exhibited twins. The hillock growth in the film is reminiscent of secondary recrystallization, where certain grains grow significantly. In fact, Pennebaker [54] treated hillock formation as secondary recrystallization. However, this formalism only explained the growth of the hillock in the film and not above the film surface.

New hillocks nucleated and existing hillocks continued to grow during subsequent cycles as was shown for the thermal cycles of the 870 nm thick film and could also be

monitored during *in situ* cycles in the SEM for a film with the same thickness. The hillock size distributions were Gaussian after the first cycle, and became broader after subsequent cycles. Thinner films generally had smaller hillocks (except for the 265 nm thick film) and the distributions of the hillock areas remained Gaussian after three cycles. Hillock sizes eventually saturated as suggested from the *in situ* annealing SEM experiment.

The hillock volume can be assumed to be directly proportional to the stress relaxation. And indeed, both the stress relaxation and the hillock formation at a constant temperature showed an exponential dependence on time. However, the fit parameters were different. The most interesting parameter is the characteristic time t_0, which, when diffusional creep mediated by grain boundaries is assumed, contains the microstructural dimensions. The grain size is cubed for classical Coble creep [26], while the stress in a free-standing thin foil [86] depends on the product of the grain size and the square of the film thickness. Hwang *et al.* [47] applied the latter to explain hillock formation in thin Al films. In this study of non-columnar Au films on a substrate, however, neither the preconditions for Coble's nor Gibb's formalism are completely fulfilled, but diffusional creep along grain boundaries is still active and provides material for hillock formation. The lower time constant for the macroscopic stress relaxation indicates that not all diffusion ultimately leads to hillock formation.

Voids are not the focus of this analysis, but the fact that they occurred independently of the microstructure led to the conclusion that they are a surface phenomenon. The main diffusive pathways were probably the vertical grain boundaries and the surface, because voids were mainly found along grain boundaries and at triple junctions. Also, the amount of material that had to be removed for creation of a void was possibly much smaller than the material needed for hillock formation. Hence, fewer diffusion pathways were required or slower diffusion was sufficient.

4.5.2 Hillocks and stress

The driving force for hillock formation was the relaxation of compressive stresses at elevated temperature. From the comparison of the *in situ* SEM heating cycles with wafer curvature measurements of the macroscopic film stress, it is known that hillocks form and grow when the film is in a compressive stress state. The 870 nm thick film in Fig. 4.16 had a stress of -85 MPa at 350 °C. Above this temperature the first hillocks were observed in the *in situ* SEM temperature cycle.

From the hillock density, ρ_{hill}, and the measured hillock areas the compressive stress $\Delta\sigma_{hill}$ relaxed by hillock formation can be estimated [42]:

$$\Delta\sigma_{hill} = M_{111} \frac{V_{hill}\rho_{hill}}{2h_f} \tag{4.7}$$

where M_{111} is the biaxial modulus for a (111)-fiber textured film and has a value of 190 GPa [79]. For the calculation of the hillock volume V_{hill} see 4.4.1. The hillock densities, the volumes, and the stresses are listed in Table 4.4. The macroscopic stress relaxation during heating is obtained from the stress-temperature cycles as described in 4.3.2 and compared to the stresses relaxed by the hillocks.

Table 4.4: Hillock densities and volumes and the stress relaxation estimated from the hillocks and from the macroscopic stress-temperature measurements.

Film thickness (nm)	Hillock density (10^{-3} µm^{-2})	Hillock volume (µm^3)	Dtress relaxed by hillocks during 3 cycles (eq. (4.7)) (MPa)	Macroscopic stress relaxation during the 2nd cycle (MPa)
265	0.5 ± 0.05	0.49 ± 0.07	87 ± 22	450 ± 50
469	0.2 ± 0.02	0.18 ± 0.03	7 ± 2	548 ± 50
458	3.9 ± 0.4	0.27 ± 0.04	218 ± 55	464 ± 50
640	15.2 ± 1.5	0.14 ± 0.03	319 ± 80	432 ± 50
870	5.5 ± 0.6	0.60 ± 0.09	358 ± 90	372 ± 50
1738	8.4 ± 0.8	0.40 ± 0.06	186 ± 46	486 ± 50

The stress relaxed by hillocks during three cycles was always lower than the macroscopic stress relaxation in one thermal cycle calculated from the stress-temperature plot. The sample to sample variation of the hillock densities was very large and it could be that the investigated areas were too small. However, it is obvious that hillock formation is not the only stress relaxation mechanism. For Al films [47] e.g. diffusional creep was attributed to be a fast relaxation mechanism and hillock formation a slower one. For other studies [42, 53, 54], in contrast, hillock formation was found to

be able to relax the total observed stress relaxation or it was presumed for data analyses [54].

If it is assumed that the stress distribution around a hillock is spherically symmetric, then a hillock could relax the stresses in the adjacent film up to a distance corresponding to the diffusion length. For a heating rate of 6 K/min between 250 and 500 °C, it can be estimated to 1.5 µm (see Table 4.3), which corresponds to an area of about 7 μm^2 that can be relaxed. The hillock radii are not considered in these estimates. Their inclusion would slightly increase this area, because material only has to move to the edge of the hillock. In contrast, the median hillock distance in our films is several 100 nm. It can, therefore, be concluded that hillock formation is a very local phenomenon and that hillock nucleation is difficult. However, it is known from microdiffraction experiments that thin Cu [97] and Al [98, 99] films have locally varying stresses for adjacent grains. Such local stress gradients would provide for the driving force to locally form hillocks and relax the area close to the hillocks at regions of maximal gradient and where the grain boundaries are of the high diffusivity nature.

Formation of hillocks also involves creation of additional surface area, which is linked to an increase in the energy of the system. On the other hand, the compressive stress in the film is relaxed by moving material onto the surface. These two contributions can be balanced to investigate, whether hillock formation was thermodynamically favorable. First, the additional surface area has to be estimated. As for the volume, the shapes of the hillocks are assumed to be between hemispheres and cones, and the average of their surface areas is taken. The surface area, S_{hill}, of a hillock is then:

$$S_{hill} = \frac{1}{2}\left(S_{HS} + S_C\right) = \frac{1}{2}\left(2\pi R^2 + \sqrt{2}\pi R^2\right) = \left(1 + \frac{\sqrt{2}}{2}\right)\pi R^2 \qquad (4.8)$$

where S_{HS} and S_C are the surface areas of a hemisphere and a cone, respectively. For the cone, the height was assumed to be equal to the radius of the base.

The total change in surface energy E_1 (per unit area) is given by the energy increase due to the total surface area increase ΔS. To obtain the change in surface area for one hillock, the area of the base of the hillock has to be subtracted from its surface area, since the base is no longer a free surface.

$$E_1 = \Delta S \gamma_s \rho_{hill} = (S_{hill} - A_{hill}) \rho_{hill} \gamma_s \tag{4.9}$$

where γ_s is the surface energy of Au.

The energy E_2 per unit area that is released the by stress relaxation is given by

$$E_2 = \Delta \sigma_{hill} \cdot h_f \tag{4.10}$$

Making an energy balance with $E_2 \geq E_1$, the value of a critical stress is obtained

$$\Delta \sigma_{hill}^{crit} = \frac{\Delta S \cdot \gamma_s \cdot \rho_{hill}}{h_f} \tag{4.11}$$

Typical values for eq. (4.11) are: ΔS = 0.8 µm^2 for a radius of R = 360 nm, γ_s = 1.4 J/m^2 [100], ρ_{hill} = 5.5·10^{-3} µm^{-2}, and h_f = 870 nm. The resulting critical stress is about 7 kPa, which is very low compared to the actual stress relaxations estimated for hillock formation, which are between 7 and 358 MPa. Hillock formation is thermodynamically favorable as long as the increase in energy due to the additional surface is smaller than the energy released by the compressive stress relaxation due to the hillock volume. Even if the hillock density were larger, e.g. 1/7 µm^{-2}, which would be the density, if the distance between hillocks were the diffusion length, the critical stress would only be 0.2 MPa.

Any possible changes of crystallographic orientations of the hillock surface compared to the film surface were not considered in this calculation. Since the critical stress is rather low, this should however, not change the fact that hillock formation is energetically favorable.

Hillock growth towards the substrate is essentially grain growth. It also reduces compressive stresses due to a decrease of lower density grain boundary volume. To estimate the effect, the hillocks in the film are assumed to be hemispheres with the radii equal to the film thickness and without grain boundaries. The volume of a hillock in a 1 µm thick film would then be 2.1 µm^3. The grains in the film are assumed to be cuboids with a grain height of 300 nm and a lateral grain size of 180 nm. Thus the volume of one grain is 0.0097 µm^3. The number of grains that would fit into the volume

is 216. With a grain boundary width of 1.5 nm, the grain boundary volume results in 0.045 μm^3, which is only 2 % of the hillock volume. Given the fact that not the total 2 % are relaxed, but less because the grain boundaries have a finite density, this effect is relatively small and negligible compared to the stresses relaxed by the material that had diffused on top of the surface. Nevertheless, it is large enough to be the driving force for hillocks to grow towards the film/substrate interface, because otherwise the hillocks would be expected to only grow on the film surface.

All energetic considerations were in favor of hillock formation. Hence, it is a kinetic issue, whether hillocks form or not. In particular the availability of enough fast diffusion pathways seems to be crucial. This is also supported the macroscopic stress-temperature measurements as shown in Fig. 4.4. Independent of the microstructure, all films showed similar high temperature compressive stresses, but only the non-columnar films exhibited hillocks.

4.6 Summary and Conclusion

The surface and its evolution for thin Au films with columnar and non-columnar microstructure on Si substrates were investigated by various measurement techniques including wafer curvature, *in* and *ex situ* SEM, FIB and TEM. The following trends are observed.

- Only the *non-columnar* films formed hillocks during thermal cycling in the high temperature compressive stress regime.
- The horizontal grain boundaries in the non-columnar films were crucial to hillock formation, because they acted as pathways for long-range material transport. The hillocks formed at or close to the surface and grew both towards the film/substrate interface and out of the film.
- From the comparison of the stresses relaxed by the hillocks according to their volume and the macroscopic stress relaxation it was found that hillock formation cannot account for the total stress relaxation during thermal cycling, but locally relaxed compressive stresses.
- It was shown that for the given hillock geometries and densities, the formation of hillocks always reduced the total energy of the system, despite e.g. an increase of free surface. Therefore, kinetics determined, whether hillocks formed for the non-columnar films or did not form for the columnar films.

5 Summary

The effects of the microstructure and the film thickness on the thermomechanical behavior of thin Au films were examined. Au provided a model system for films with bare surfaces that allowed investigating the role of surface diffusion during thermal cycling. It was thoroughly examined how stresses and surface morphology evolved. To this end, films with different microstructures were fabricated by DC magnetron sputtering Au onto Si substrates at two different substrate temperatures. Three different types of films were obtained. Sputtering at room temperature yielded columnar films with grain sizes approximately equal to the film thicknesses for films that were between 57 and 121 nm thick, while films between 173 and 1738 nm thick were non-columnar with grain boundaries parallel to the film/substrate interface. These films contained thermally stable grains with lateral sizes between 98 and 181 nm and grain heights between 105 and 300 nm. Films sputtered at 300 °C had columnar grains with the grain sizes roughly equal to the film thicknesses. The (111)-fiber texture for the 300 °C sputtered samples was rather broad, when compared to the room temperature sputtered films. Also, the surfaces were substantially rougher when deposited at high temperature.

The films responded differently to thermal cycling between room temperature and 500 °C for different microstructures. The non-columnar films showed the well-known and reported behavior, in which the initial loading was thermoelastic, followed by a compressive stress plateau. Initial unloading was also thermoelastic and subsequently exhibited two plastic regimes, where the first had a shallower slope than the second. The ultra-fine, columnar films ($h_f \leq 121$ nm) behaved similarly, however, instead of showing a compressive stress plateau during heating, the stress kept increasing until 500 °C. The thermoelastic unloading occurred over a broader temperature range, so that the two plastic regions were harder to identify. The columnar films sputtered at 300 °C lacked an initial thermoelastic unloading during cooling, and thus the first of the two plastic regimes began directly upon cooling.

The stress-temperature behavior of all films indicated that, independent of the microstructure, diffusive processes operated at elevated temperatures and dislocation glide was dominant at room temperature. The columnar films sputtered at room temperature and at 300 °C both fulfilled the precondition for constrained diffusional creep, namely a columnar microstructure and a free surface. In deed, TEM micrographs

revealed parallel glide dislocations in Au films for the first time. This type of dislocations is a direct consequence of material diffusion from the surface into the grain boundaries under tensile stresses. The heating portion of the stress-temperature curves could be described by simulations employing the constrained diffusional creep mechanism with a threshold stress for its onset. For type CL films, the grain sizes for the simulation had to be larger than the experimentally determined grain sizes. Although the microstructures of both types of columnar films were similar, the stress-temperature curves were different, e.g. in contrast to type CL films, type CH films did not unload thermoelastically. It could be that the diffusional processes and thus the stress-temperature behavior at elevated temperatures depended on the sharpness of the texture, the surface roughness, the film thicknesses and/or the film/substrate interface, whose structure might have been influenced by the sputtering conditions.

The comparison to studies of Cu films showed that Au and Cu both exhibited constrained diffusional creep and behaved similarly in the ultra-thin film thickness regime ($h_f \leq 120$ nm). When compared to Al films, as expected, the stress-temperature curves of Al and Au differed, because Al did not exhibit a diffusive regime due to the native oxide that hinders surface diffusion.

In this study, the measurements of stress data for Au films could be extended further below 100 nm into the ultra-thin regime. The stresses were found to depend on the film thickness and the grain size. However, when plotted vs. the inverse grain size, the stresses of all films fell onto one line. For the columnar films, grain size and film thickness were approximately equal, but for non-columnar films the grain size was significantly smaller than the film thickness and nearly constant. The stresses roughly agreed with those predicted by the Thompson model. It is also noteworthy that the grains in columnar and non-columnar films had different surroundings, but the plot of the stress vs. the inverse film thickness only showed all data points on one line. Hence, the results of the stress measurements suggest that not the surrounding, e.g. the film/substrate interface or the surface, but the dimension itself determined the strength of the material. The comparison of the film stresses to literature data of Au in small dimension also showed similar stress values for all samples, although the results were obtained by different testing techniques and for different sample geometries. This is partly in contrast to the models of thin film plasticity, where the surface state and the substrate matter, but in accordance with the evaluation of the columnar and non-columnar films.

The surface after three thermal cycles showed grain boundary grooves and voids for all film types. The non-columnar films additionally formed hillocks. Thus, a precondition for hillock formation was grain boundaries parallel to the film/substrate interface, which could provide a network of fast diffusion pathways. The hillock densities and basal areas were determined. These data were used to estimate the compressive stresses that were locally relaxed by moving the material from the film into the hillocks. The stress relaxation by hillock formation was always smaller than the macroscopic stress relaxation determined from wafer curvature measurements. A comparison of *in situ* thermal cycles and temperature holds performed in an SEM and the stress-temperature measurements in the wafer curvature apparatus showed that hillocks first formed at about 350 °C when the film was in a compressive stress state and when diffusion was active. Annealing at 420 °C for nearly 4 h suggested that the hillock size saturated. The hillock microstructure investigated by FIB and TEM, revealed that they are not single crystalline and have grains significantly larger than those in the film.

By comparison with columnar films that had similar film thicknesses and compressive stresses at elevated temperatures, but did not form hillocks, it could be concluded that the unusual grain structure with horizontal, in-plane grain boundaries is crucial for hillock formation. Material moves along this grain boundary network in the film plane and then eventually diffuses along a vertical grain boundary with a high diffusivity to the surface, where the hillock nucleates at a triple junction, when a significant flux divergence is given.

In conclusion, diffusive stress relaxation played a major role at elevated temperatures for Au films. This was expected due to the free surface. Constrained diffusional creep could be identified in columnar Au films. Non-columnar films also showed diffusional creep, but additionally formed hillocks, which was a local stress relaxation mechanism. At room temperature, clearly the smallest dimension dominated plasticity. The dependence of the stresses on the film thickness and the grain size, respectively was generally were weak, but agreed well with literature data of other Au samples in small dimensions.

6 Appendix

6.1 Film thickness

Since the film thickness during sputtering was only controlled by deposition time, which in turn was calibrated from Dektak profilometer measurements, it was necessary to determine the actual thicknesses of the films using cross-sectional TEM. At least 8 measurements per film were averaged with the statistical errors below 1.5 %; for [CL121b] it was only 3 %. Fig. A-1 shows the room temperature sputtered films, i.e. type NC and CL. Two sputtering runs with different film thickness calibrations were performed and are denoted with batch 1 and 2. The linear fits of the two batches are used to extrapolate the actual film thicknesses for films not measured. The error of the fit is about 1%.

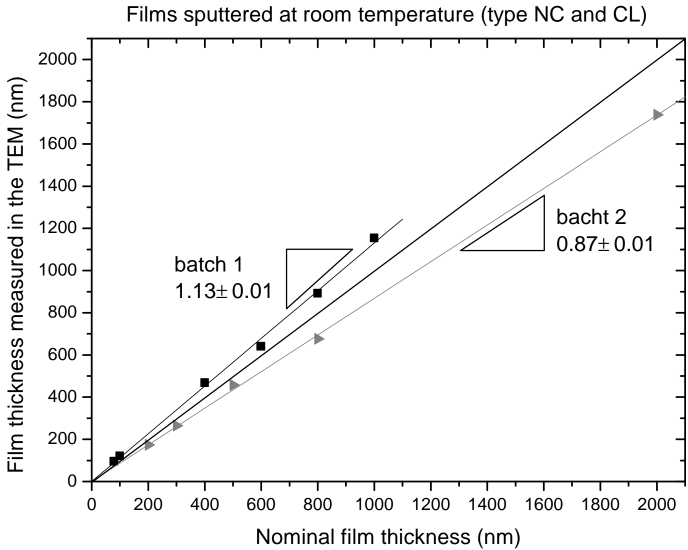

Fig. A-1: Film thickness measurements from cross-sectional TEM vs. the nominal film thickness for room temperature deposited films. Each of the two batches shows a linear dependence. The error bars of the thickness are within the size of the symbol.

Fig. A-2 shows the measured vs. the nominal film thicknesses for the films sputtered at 300 °C. Since these data also fall onto a line, the remaining film thicknesses could be reliably extrapolated.

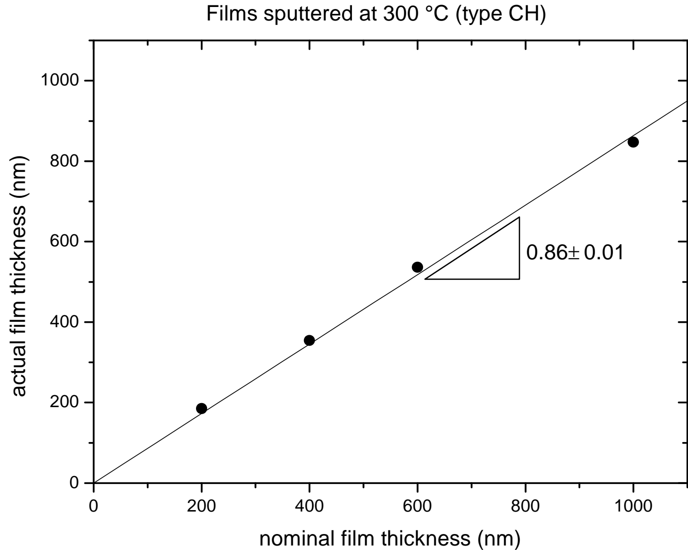

Fig. A-2: Measured film thickness as a function of the nominal thickness and the linear fit of the data. The errors are within the size of the symbol.

The statistical error for measured film thickness is usually below 1.5 %. Only for [CH185] it is 3% due to the large roughness. The errors of the linear fits of the measured vs. the nominal film thicknesses are about 1%. Therefore, we will use Δh_f = 1.5% h_f for further estimates and calculations of film thickness errors.

Table A-1 summarizes the measured and extrapolated films for all sputtering runs.

Table A-1: List of all samples giving their actual film thickness

<table>
<tr><th>sample</th><th>film thickness (nm)</th><th></th><th></th></tr>
<tr><td>[CH185]</td><td>185</td><td>measured</td><td rowspan="7">sputtered at 300 °C</td></tr>
<tr><td>[CH258]</td><td>258</td><td>extrapolated</td></tr>
<tr><td>[CH354]</td><td>354</td><td>measured</td></tr>
<tr><td>[CH430]</td><td>430</td><td>extrapolated</td></tr>
<tr><td>[CH536]</td><td>536</td><td>measured</td></tr>
<tr><td>[CH688]</td><td>688</td><td>extrapolated</td></tr>
<tr><td>[CH847]</td><td>847</td><td>measured</td></tr>
<tr><td colspan="4"></td></tr>
<tr><td>[CL57a]</td><td>57</td><td>extrapolated</td><td rowspan="5">sputtered at room temperature

batch 1</td></tr>
<tr><td>[CL57b]</td><td>57</td><td>extrapolated</td></tr>
<tr><td>[CL96]</td><td>96</td><td>measured</td></tr>
<tr><td>[CL121a]</td><td>121</td><td>measured</td></tr>
<tr><td>[CL121b]</td><td>121</td><td>extrapolated</td></tr>
</table>

<table>
<tr><td>[NC226]</td><td>226</td><td>extrapolated</td><td rowspan="5"></td></tr>
<tr><td>[NC469]</td><td>469</td><td>measured</td></tr>
<tr><td>[NC640]</td><td>640</td><td>measured</td></tr>
<tr><td>[NC893]</td><td>893</td><td>measured</td></tr>
<tr><td>[NC1154]</td><td>1154</td><td>measured</td></tr>
<tr><td colspan="4"></td></tr>
<tr><td>[NC173]</td><td>173</td><td>measured</td><td rowspan="7">sputtered at room temperature

batch 2</td></tr>
<tr><td>[NC265]</td><td>265</td><td>measured</td></tr>
<tr><td>[NC458]</td><td>458</td><td>extrapolated</td></tr>
<tr><td>[NC552]</td><td>552</td><td>extrapolated</td></tr>
<tr><td>[NC676]</td><td>676</td><td>measured</td></tr>
<tr><td>[NC870]</td><td>870</td><td>extrapolated</td></tr>
<tr><td>[NC1738]</td><td>1738</td><td>measured</td></tr>
</table>

6.2 Texture

Table A-2 gives the FWHM of the (111)-fiber texture for the samples investigated.

Table A-2: FWHM values from (111) rocking curves

Films sputtered at room temperature			**Films sputtered at 300 °C**		
sample name	film thickness (nm)	FWHM (°)	sample name	film thickness (nm)	FWHM (°)
[CL57b]	57	3.5	[CH185]	185	13.1
[CL121b]	121	3.5	[CH354]	354	12.6
[NC226]	226	4.0	[CH536]	536	11.8
[NC469]	470	4.0	[CH847]	847	10.9
[NC640]	640	4.0			
[NC1154]	1154	3.5			

6.3 Stress-temperature measurements

6.3.1 Experimental error of the wafer curvature measurements

This section describes in detail the errors estimated and calculated for the wafer curvature measurements. The film stresses were calculated from curvature measurements according to the Stoney equation [91]:

$$\sigma_f = \frac{M_s \cdot h_s^2}{6h_f} \cdot \left(\frac{1}{R_{meas}} - \frac{1}{R_{ref}} \right) \tag{A-1}$$

where M_s is the biaxial modulus of the substrate, h_s is the substrate thickness, and h_f is the film thickness. R_{ref} is the radius of curvature of the uncoated wafer and R_{meas} is the radius of curvature of the substrate with the metal film on top.

Error propagation of eq. (A-1) yields that the error $\Delta\sigma_f$ of the film stress is composed of the uncertainty Δh_s of substrate thickness and uncertainty Δh_f of the film thickness. Furthermore, the errors of the curvature measurements ΔR_{ref} for the uncoated and ΔR_{meas} for the coated substrate enter.

$$\begin{aligned}\Delta\sigma_f &= \left|\frac{\partial\sigma_f}{\partial h_s}\right|\Delta h_s + \left|\frac{\partial\sigma_f}{\partial h_f}\right|\Delta h_f + \left|\frac{\partial\sigma_f}{\partial R_{meas}}\right|\Delta R_{meas} + \left|\frac{\partial\sigma_f}{\partial R_{ref}}\right|\Delta R_{ref} \\ &= \left|\sigma_f\right| \cdot \frac{\Delta h_s}{h_s} + \left|\sigma_f\right| \cdot 2\frac{\Delta h_f}{h_f} + \left|\frac{M_s}{6}\frac{h_s^2}{h_f}\frac{1}{R_{meas}}\right| \cdot \frac{\Delta R_{meas}}{R_{meas}} + \left|\frac{M_s}{6}\frac{h_s^2}{h_f}\frac{1}{R_{ref}}\right| \cdot \frac{\Delta R_{ref}}{R_{ref}} \end{aligned} \tag{A-2}$$

The substrate thickness was measured and varies at maximum ± 5 µm over the whole 2'' sample. Given a substrate thickness of about 200 µm this makes a relative error of 2.5 %. The errors of the film thicknesses were discussed in section 6.1 and assumed to be 1.5 %.

The main error for the curvature measurements originates from the non-uniform wafer curvature, because the curvature is only measured experimentally along one line. For different positions of the wafer in the laser scanning system, the curvature is measured along different lines, which eventually leads to a different curvature value, if the wafer is non-uniformly curved. The influence of the accuracy of positioning was studied by examination of the reproducibility of the curvature measurements. Several wafers were measured, taken out, remounted, and measured again. The flat of the wafer was lined up the same for each measurement to be as reproducible as possible. The error was estimated to be 10 %. However, the issue of positioning and reproducibility arises twice in the experiment, namely for the reference measurement of the uncoated substrate and for the actual measurement of the coated sample. For both cases, this is

only an issue of the silicon wafer and can thus be summarized in the error of the reference measurement $\Delta R_{ref} / R_{ref}$ = 20%. All other errors of the curvature measurements are negligible and thus $\Delta R_{meas} / R_{meas} = 0$.

Plugging these numbers in eq. (A-2), the error which represents the offset of the stress measurement is given by:

$$\Delta\sigma_f = 0.055 \cdot \left|\sigma_f\right| + 0.20 \cdot \left|\frac{M_s}{6} \frac{h_s^2}{h_f} \frac{1}{R_{ref}}\right| \qquad \text{(A-3)}$$

From eq. (A-3) it is seen that wafers with a large radius of curvature have smaller errors. This is reasonable, because the flatter the wafer, the smaller is the reference curvature that is subtracted from the curvature measurement of the coated substrate and the non-uniformity becomes less important. Additionally, flatter wafers are usually more uniformly curved.

During stress-temperature cycles, a second issue that arises is the change of wafer position due to thermal drift. This does not result in an offset of the stress-temperature curve as the above errors do, but rather changes the shape of the stress-temperature curves, because the line along which the curvature is measured changes during the experiment. Especially at elevated temperatures, where the sample had drifted the most, this becomes relevant. The sample position is indicated by x- and y-values that basically represent the position of the laser signal on the photo cell. The y-values changes more during thermal cycling and seems to be more important. Fig. A-4 and A-5 show the first three stress-temperature cycles for a 688 nm thick film and the y-values vs. the temperature during thermal cycling, respectively. At elevated temperatures, the first cycle has different stress values than the subsequent cycles; at 500 °C the difference is 35 MPa. Also, the y-values are different for the first and the subsequent cycles. In general, the stress-temperature evolution at elevated temperatures has an error of 30 to 50 MPa because of thermal drift. This is an issue in the analysis of curve shapes at elevated temperatures. In the given example it cannot be resolved, whether the film exhibits a stress plateau of a slight stress relaxation.

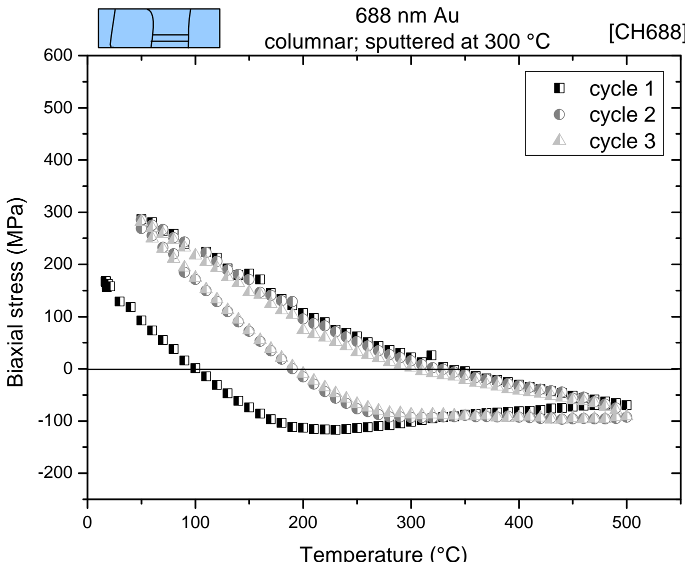

Fig. A-4: The first three stress-temperature cycles of film [CH688]. The behavior of the first cycle at elevated temperature is different than of the subsequent cycles. The difference is attributed to a change in sample position due to thermal drift and the resultant measurement error.

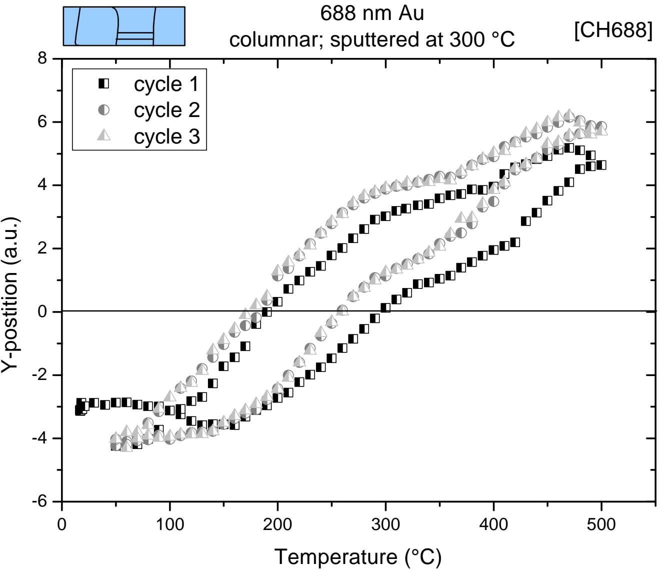

Fig. A-5: Thermal drift of [CH688] indicated by the y-position value during three stress-temperature cycles.

6.3.2 Stress-temperature curves

The stress-temperature curves of all samples are shown for the three different types. For each type, a table with values of the slopes, the stresses and transition temperatures between the various regimes are given.

6.3.2.1 Stress-temperature curves of type CH

The stress-temperature curves for the films that were sputtered at 300 °C are shown in Fig. A-6 beginning with the smallest film thickness.

Fig. A-6: Stress-temperature curves of all type CH films

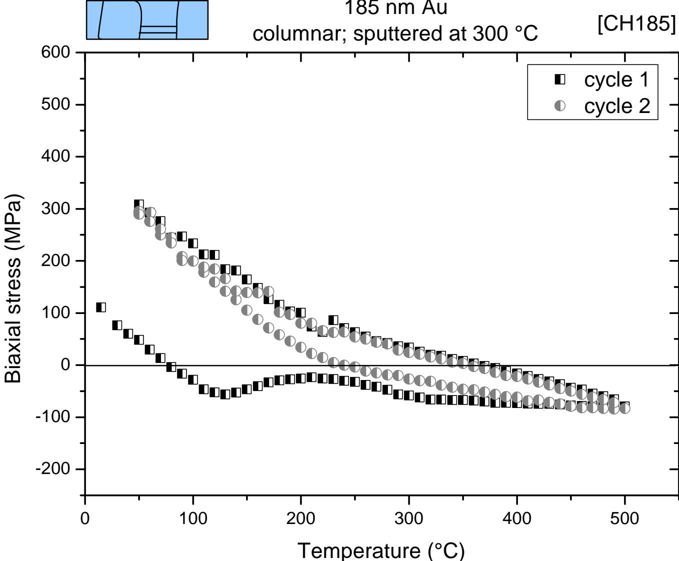

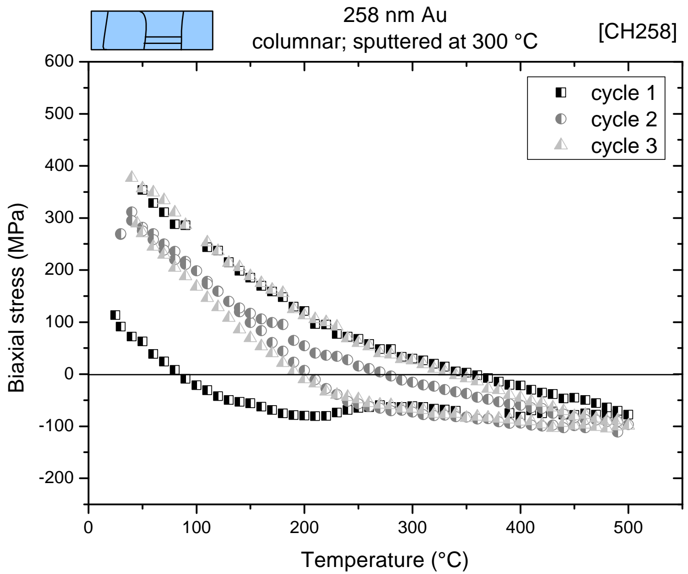
258 nm Au
columnar; sputtered at 300 °C
[CH258]
cycle 1
cycle 2
cycle 3
Biaxial stress (MPa)
Temperature (°C)
600
500
400
300
200
100
0
-100
-200
0
100
200
300
400
500

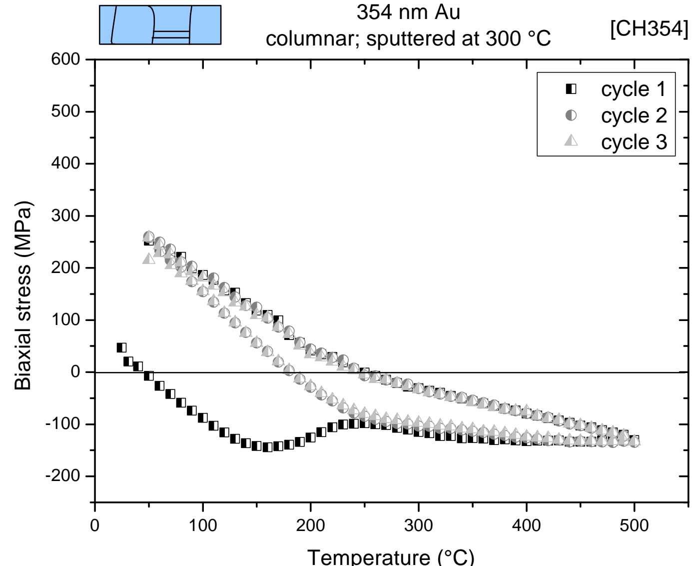
354 nm Au
columnar; sputtered at 300 °C
[CH354]
cycle 1
cycle 2
cycle 3
Biaxial stress (MPa)
Temperature (°C)
600
500
400
300
200
100
0
-100
-200
0
100
200
300
400
500

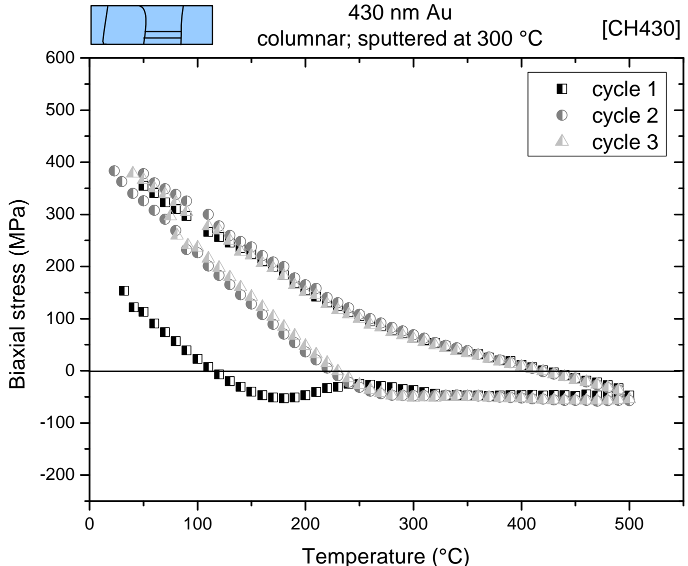
430 nm Au
columnar; sputtered at 300 °C
[CH430]
cycle 1
cycle 2
cycle 3
Biaxial stress (MPa)
Temperature (°C)
600
500
400
300
200
100
0
-100
-200
0
100
200
300
400
500

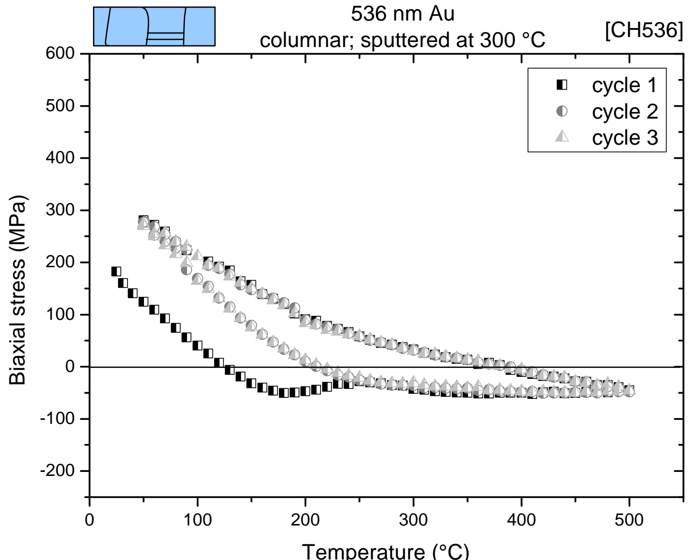
536 nm Au
columnar; sputtered at 300 °C
[CH536]
cycle 1
cycle 2
cycle 3
Biaxial stress (MPa)
Temperature (°C)
600
500
400
300
200
100
0
-100
-200
0
100
200
300
400
500

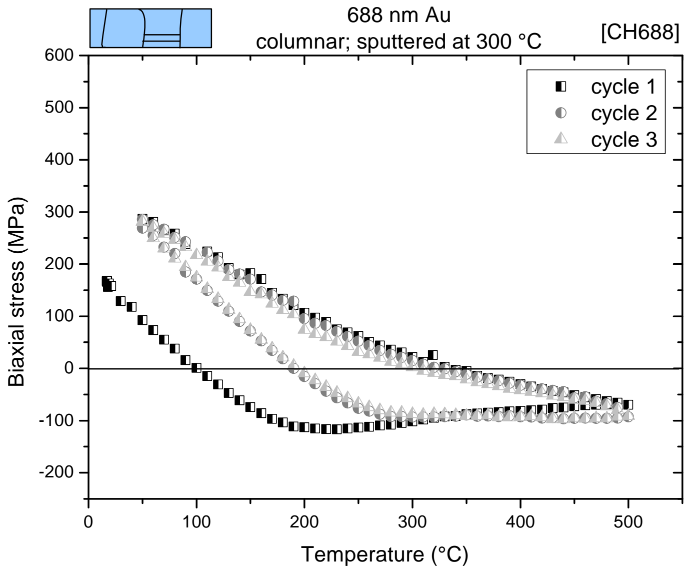

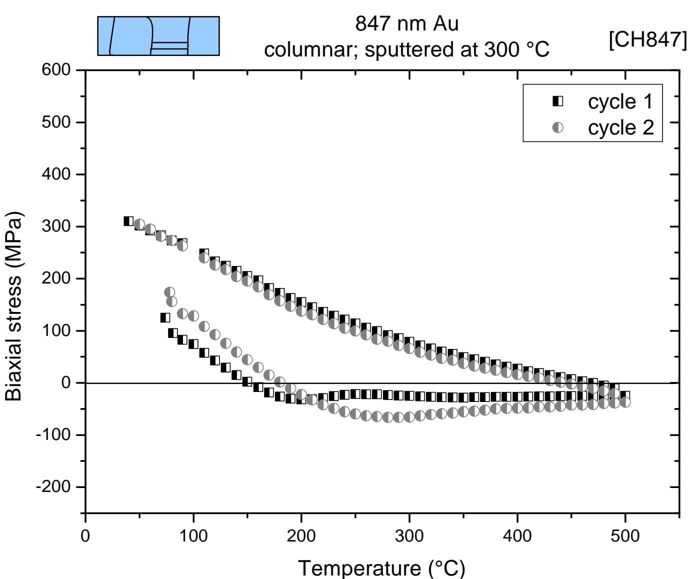

As discussed in chapter 3.3.2.2, the stress-temperature curves of type CH can be divided into four different regimes: HI, HII, CII, CII. The slopes and the transition temperatures are given in table A-3.

Table A-3: Slopes, stresses and transition temperatures for type CH films.

sample	film thickness (nm)	stress at 50 °C (MPa)	slope HI (MPa/K)	slope CII (MPa/K)	slope CIII (MPa/K)	transition temperatu re HI to HII (°C)	transition temperature CII to CIII (°C)
[CH185]	185	299 ± 26	-1.80 ± 0.04	-0.50 ± 0.01	-1.53 ± 0.05	200	200
[CH258]	258	335 ± 58	-1.88 ± 0.01	-0.70 ± 0.02	-1.19 ± 0.06	210	240
[CH354]	354	256 ± 18	-1.95 ± 0.02	-0.49 ± 0.01	-1.45 ± 0.03	200	230
[CH430]	430	371 ± 36	-1.98 ± 0.02	-0.51 ± 0.02	-1.44 ± 0.03	220	260
[CH536]	536	276 ± 21	-1.77 ± 0.03	-0.44 ± 0.03	-1.21 ± 0.03	180	240
[CH688]	688	281 ± 19	-1.92 ± 0.03	-0.36 ± 0.01	-1.33 ± 0.04	220	270
[CH847]	847	303 ± 18	-1.61 ± 0.03	-0.40 ± 0.01	-1.14 ± 0.02	180	250

6.3.2.2 Stress-temperature curves of type NC

The stress-temperature measurements of all type NC films are shown in Fig. A-7, beginning with the smallest film thickness.

Fig. A-7: Stress-temperature cycles of all type NC films

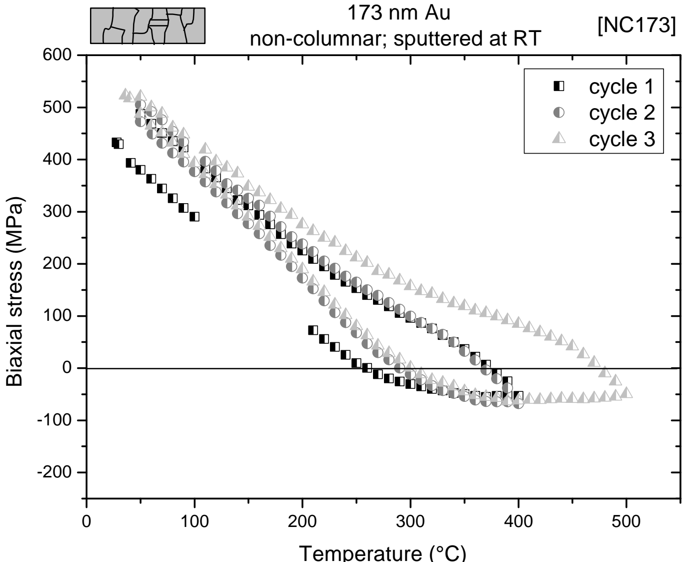

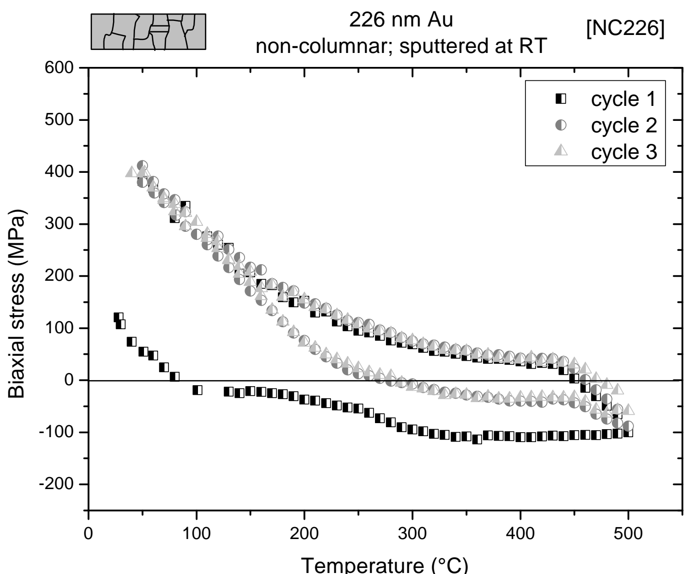
226 nm Au
non-columnar; sputtered at RT
[NC226]
cycle 1
cycle 2
cycle 3
Biaxial stress (MPa)
Temperature (°C)
600
500
400
300
200
100
0
-100
-200
0
100
200
300
400
500

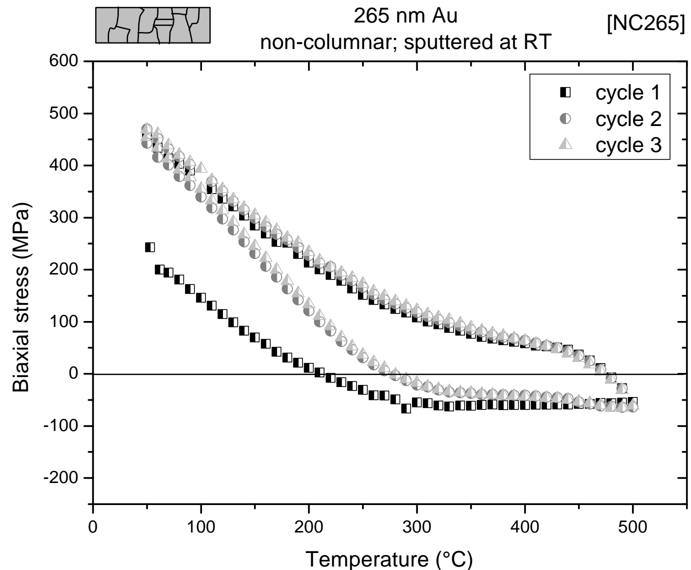
265 nm Au
non-columnar; sputtered at RT
[NC265]
cycle 1
cycle 2
cycle 3
Biaxial stress (MPa)
Temperature (°C)
600
500
400
300
200
100
0
-100
-200
0
100
200
300
400
500

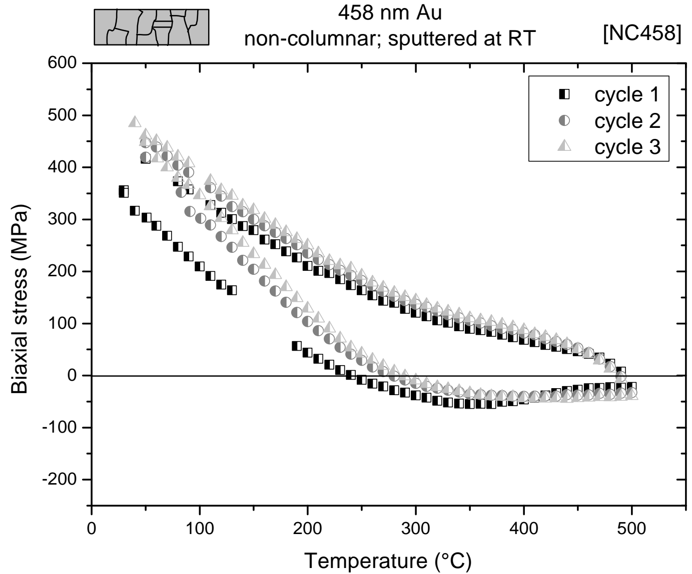
458 nm Au
non-columnar; sputtered at RT
[NC458]
cycle 1
cycle 2
cycle 3
Biaxial stress (MPa)
Temperature (°C)
600
500
400
300
200
100
0
-100
-200
0
100
200
300
400
500

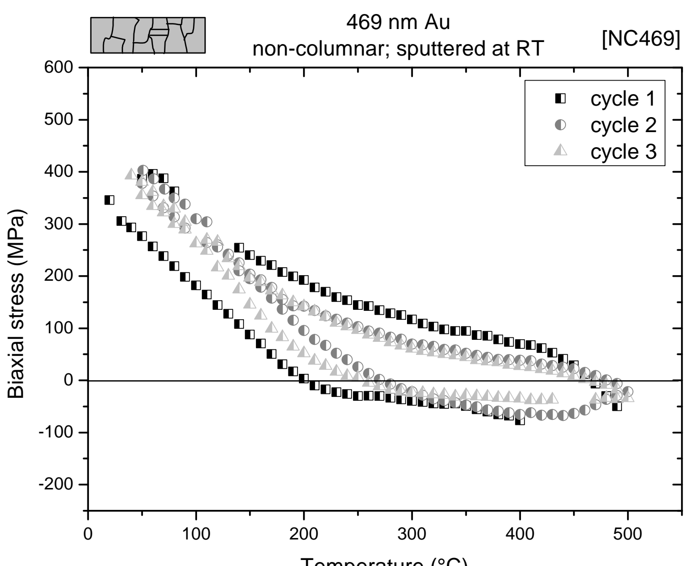
469 nm Au
non-columnar; sputtered at RT
[NC469]
cycle 1
cycle 2
cycle 3
Biaxial stress (MPa)
Temperature (°C)
600
500
400
300
200
100
0
-100
-200
0
100
200
300
400
500

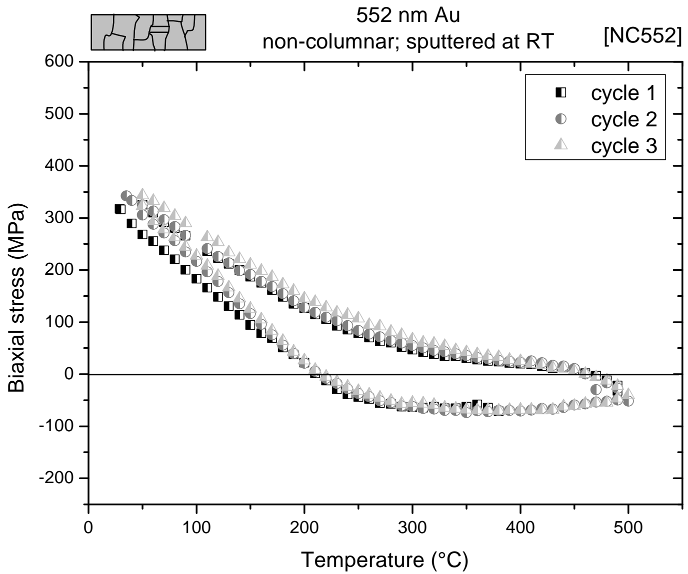
552 nm Au
non-columnar; sputtered at RT
[NC552]
cycle 1
cycle 2
cycle 3
Biaxial stress (MPa)
Temperature (°C)
600
500
400
300
200
100
0
-100
-200
0
100
200
300
400
500

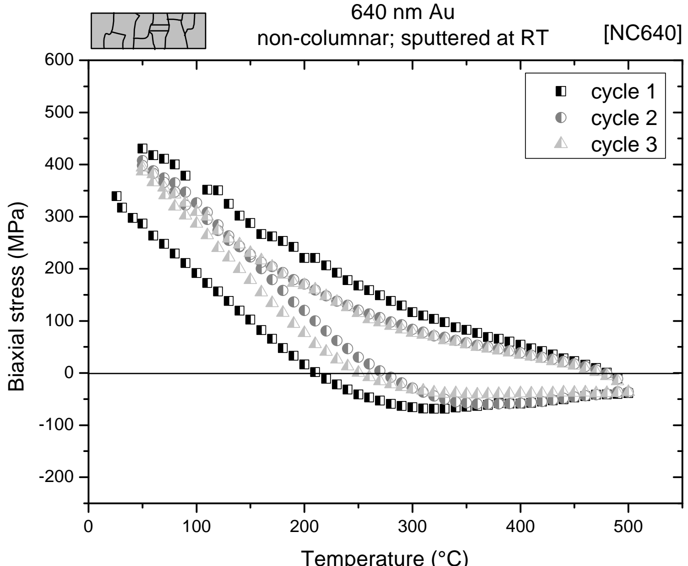
640 nm Au
non-columnar; sputtered at RT
[NC640]
cycle 1
cycle 2
cycle 3
Biaxial stress (MPa)
Temperature (°C)
600
500
400
300
200
100
0
-100
-200
0
100
200
300
400
500

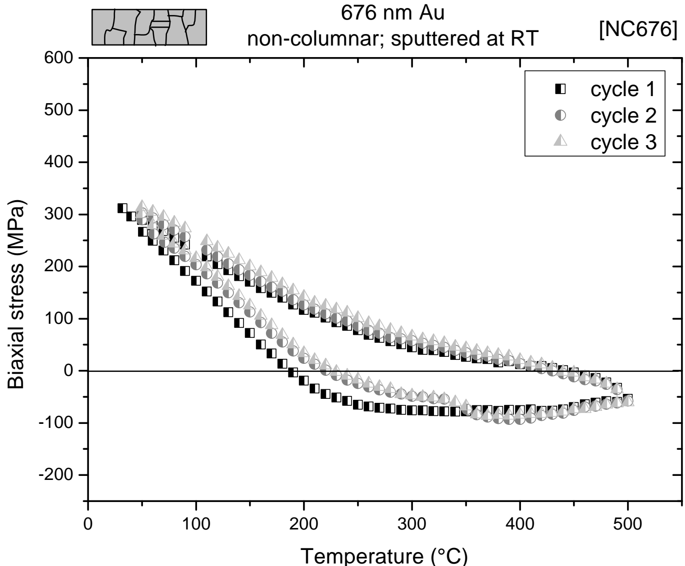
676 nm Au
non-columnar; sputtered at RT
[NC676]
cycle 1
cycle 2
cycle 3
Biaxial stress (MPa)
Temperature (°C)
600
500
400
300
200
100
0
-100
-200
0
100
200
300
400
500

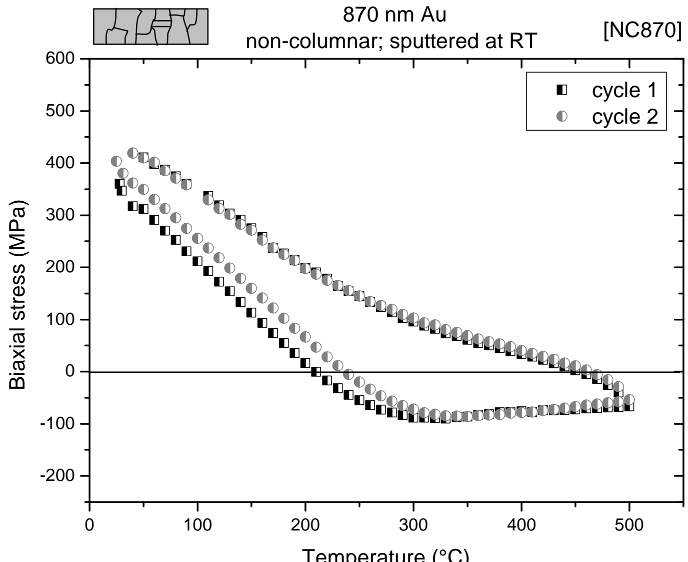
870 nm Au
non-columnar; sputtered at RT
[NC870]
cycle 1
cycle 2
Biaxial stress (MPa)
Temperature (°C)
600
500
400
300
200
100
0
-100
-200
0
100
200
300
400
500

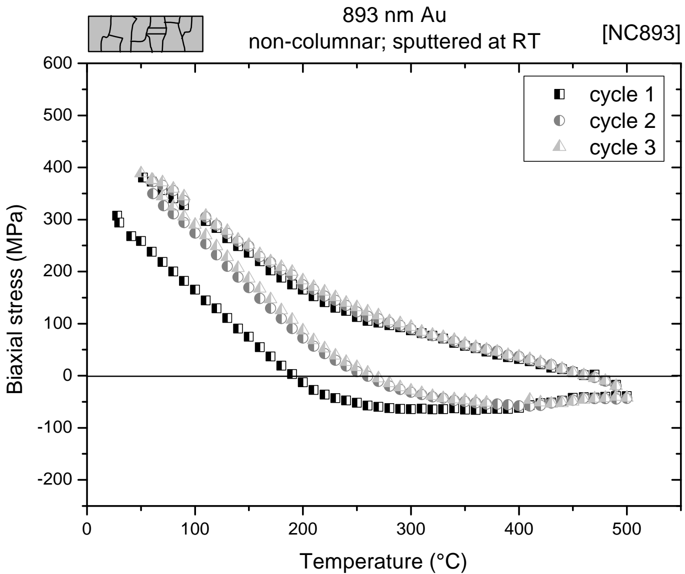

893 nm Au
non-columnar; sputtered at RT
[NC893]
cycle 1
cycle 2
cycle 3
Biaxial stress (MPa)
Temperature (°C)

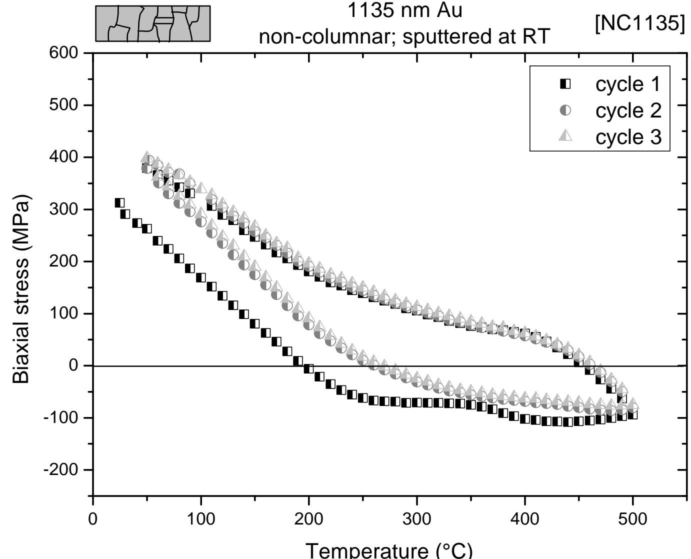

1135 nm Au
non-columnar; sputtered at RT
[NC1135]
cycle 1
cycle 2
cycle 3
Biaxial stress (MPa)
Temperature (°C)

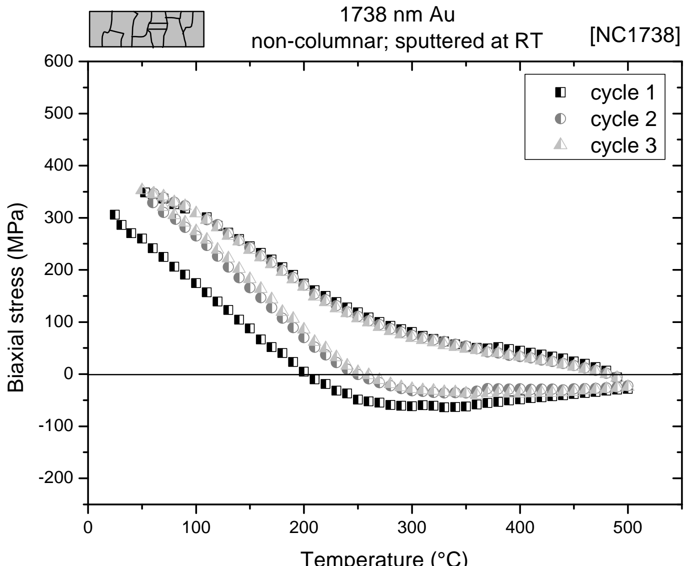

The non-columnar films (type NC) also exhibit different regimes during thermal cycling. Compared to type CH, the cooling curves have a third regime CI. The values of the slopes and transition temperatures are listed in Table A-4 and Table A-5.

Table A-4: Slopes and stresses of type NC films.

sample	film thickness (nm)	stress at 50 °C (MPa)	slope HI (MPa/K)	slope CI (MPa/K)	slope CII (MPa/K)	slope CIII (MPa/K)
[NC173]	173	504 ± 45	-2.04 ± 0.01	-1.94 ± 0.1	-0.75 ± 0.02	-1.55 ± 0.03
[NC226]	226	397 ± 37	-2.08 ± 0.01	-2.20 ± 0.1	-0.40 ± 0.02	-1.62 ± 0.05
[NC265]	265	464 ± 36	-2.14 ± 0.01	-2.36 ± 0.3	-0.59 ± 0.01	-1.57 ± 0.03
[NC458]	458	442 ± 50	-2.10 ± 0.02	-2.64 ± 0.3	-0.49 ± 0.02	-1.37 ± 0.03
[NC469]	469	381 ± 26	-2.14 ± 0.04	-1.28 ±	-0.32 ± 0.03	-1.53 ± 0.07
[NC552]	552	331 ± 31	-1.97 ± 0.02	-1.34 ± 2	-0.40 ± 0.02	-1.23 ± 0.02
[NC640]	640	410 ± 42	-1.95 ± 0.02	-1.78 ± 0-4	-0.42 ± 0.01	-1.31 ± 0.05
[NC676]	676	302 ± 30	-1.76 ± 0.02	-1.58 ± 0.3	-0.43 ± 0.02	-1.21 ± 0.02
[NC870]	870	411 ± 23	-1.86 ± 0.01	-1.90 ± 0.3	-0.63 ± 0.02	-1.45 ± 0.02
[NC893]	893	384 ± 25	-2.00 ± 0.02	-2.31	-0.51 ± 0.02	-1.42 ± 0.02
[NC1154]	1154	390 ± 33	-1.95 ± 0.02	-2.49 ± 0.3	-0.43 ± 0.02	-1.43 ± 0.02
[NC1738]	1738	337 ± 23	-1.88 ± 0.02	-1.21 ± 0.3	-0.30 ± 0.01	-1.45 ± 0.01

Table A-5: Transition temperatures of type NC films.

sample	film thickness (nm)	transition HI to HII (°C)	transition CI to CII (°C)	transition CII to CIII (°C)
[NC173]	173	280	460	280
[NC226]	226	230	440	240
[NC265]	265	240	460	280
[NC458]	458	240	470	270
[NC469]	469	200	470	260
[NC552]	552	210	470	270
[NC640]	640	260	470	280
[NC676]	676	200	470	230
[NC870]	870	240	470	250
[NC893]	893	220	480	240
[NC1154]	1154	230	460	230
[NC1738]	1738	230	470	260

6.3.2.3 Stress-temperature curves of type CL

The stress-temperature behavior for the type CL films is shown in Fig. A-8

Fig. A-8: Stress-temperature curves for type CL films.

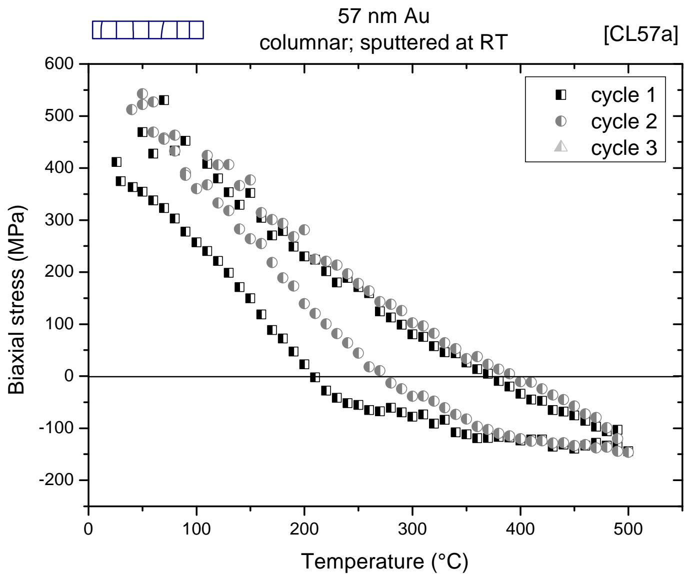

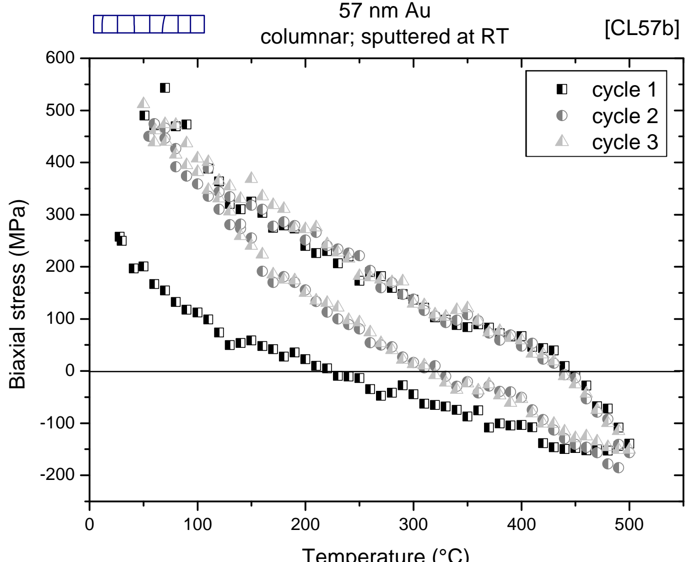
57 nm Au
columnar; sputtered at RT
[CL57b]
cycle 1
cycle 2
cycle 3
Biaxial stress (MPa)
Temperature (°C)
600
500
400
300
200
100
0
-100
-200
0
100
200
300
400
500

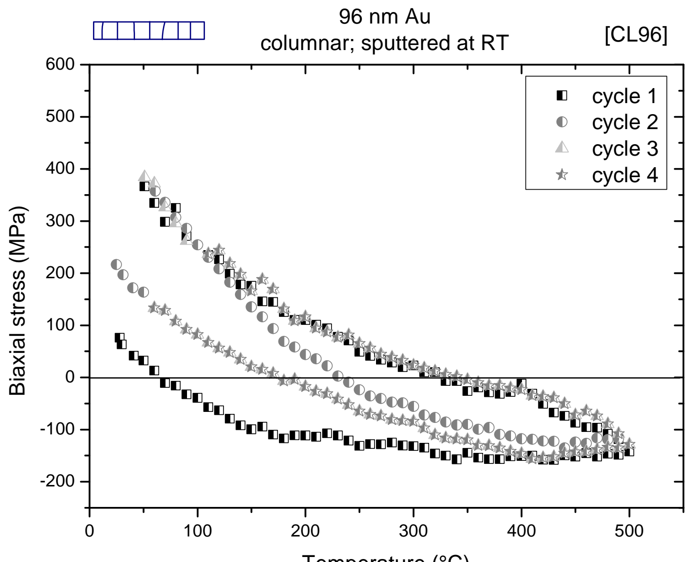
96 nm Au
columnar; sputtered at RT
[CL96]
cycle 1
cycle 2
cycle 3
cycle 4
Biaxial stress (MPa)
Temperature (°C)
600
500
400
300
200
100
0
-100
-200
0
100
200
300
400
500

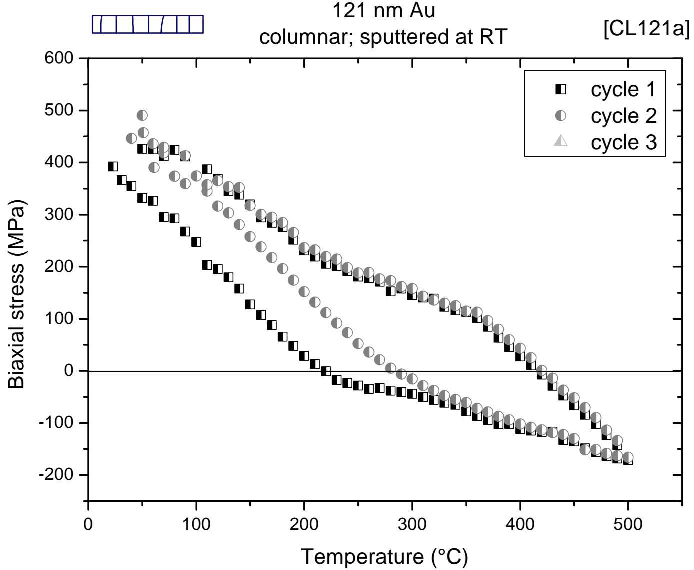

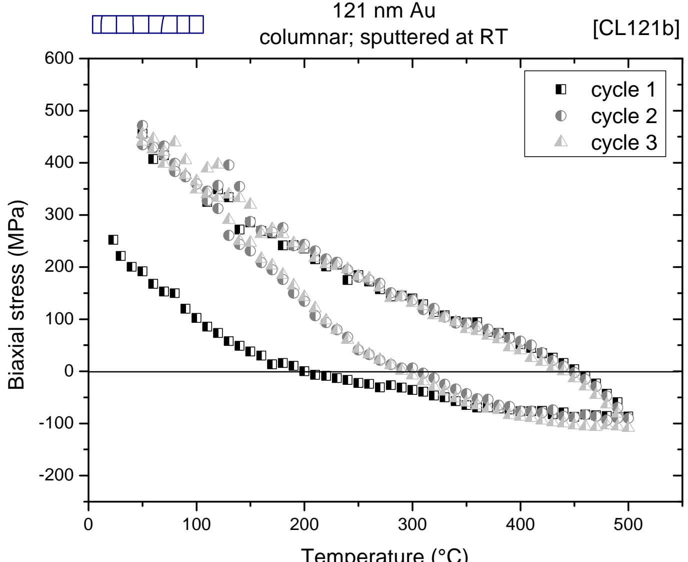

The films of type CL have two heating regimes (HI and HII). During cooling an elastic unloading is observed (CI). Other than that, the cooling curve cannot be classified in CII and CIII as for type CH and NC. The slopes and temperatures are given in Table A-6.

Table A-6: Slopes, stresses and transition temperature of type CL films.

sample	film thickness (nm)	stress at 50 °C (MPa)	slope HI (MPa/K)	transition HI to HII (°C)	slope CI (MPa/K)	transition CI to plastic cooling (°C)
[CL57a]	57	521 ± 50	-2.28 ± 0.03	270	-2.22 ± 0.1	460
[CL57b]	57	501 ± 39	-2.23 ± 0.1	200	-2.84 ± 0.2	440
[CL96]	96	375 ± 30	-2.42 ± 0.03	180	-1.62 ± 0.1	450
[CL121a]	121	441 ± 39	-2.11 ± 0.01	280	-2.01 ± 0.04	360
[CL121b]	121	455 ± 41	-2.12 ± 0.04	260	-1.57 ± 0.09	440

7 Deutsche Zusammenfassung

7.1 Einleitung

Die schnell voranschreitende Entwicklung in der Mikrosystemtechnik hat stetig neue Herausforderungen für die Werkstoffwissenschaft zur Folge, da eine Vielzahl neuer Materialien und Materialkombinationen eingesetzt werden soll. Die Miniaturisierung spielt hierbei eine zentrale Rolle, da viele Materialeigenschaften Größeneffekte zeigen. Dünne Metallschichten z.B. haben außergewöhnlich hohe Festigkeiten [2], die sogar mit abnehmender Schichtdicke noch zunehmen. Dies kann positive und negative Auswirkungen für den Einsatz im Bauteil haben. Einerseits durchläuft das Bauteil während des Herstellungsprozesses oft mehrere Temperaturbehandlungen. Aufgrund der unterschiedlichen thermischen Ausdehnungskoeffizienten der Materialen können hohe Spannungen in der Metallschicht entstehen. Diese relaxieren u.U. während des Einsatzes, wodurch sich die Eigenschaften des Bauteils ändern können. Weitere Folgen der Temperaturbehandlung können die Bildung von Materialanhäufungen (Hügel) auf der Oberfläche oder Löcher in der Schicht sein. Die Fähigkeit der Schicht hohe Spannungen auszuhalten, kann man sich andererseits auch zur Kraftübertragung zunutze machen. Sowohl zur Verbesserung der Bauteilzuverlässigkeit als auch um die Leistung gezielt zu einzustellen, ist es wichtig die grundlegenden Mechanismen zu verstehen.

Für viele Anwendungen in der Mikrosystemtechnik ist Gold (Au) ein geeignetes Material, da es ein hervorragender elektrischer Leiter ist und eine hohe optische Reflektivität besitzt. Des Weiteren ist es resistent gegen die meisten Chemikalien, die als Ätzlösungen während der Herstellung verwendet werden. Und nicht zuletzt öffnet seine Biokompatibilität den Weg für den Einsatz in Mikrosystemen für biologische Anwendungen.

In der Dünnschichtmechanik wurden in den letzten 15 Jahren hauptsächlich die Leiterbahnmaterialien Al und Cu untersucht. Es wurde beobachtet, dass die Fließspannungen höher sind als im entsprechenden Massivmaterial und mit abnehmender Schichtdicke ansteigen [4-7]. Dies wurde der Einengung der Versetzungsbewegung durch die Schichtdicke zugeschrieben [8]. Bei polykristallinen Schichten kommt eine weitere Einengung durch die Korngrenzen hinzu [9]. In den letzen Jahren wurde auch, ausgelöst durch eine theoretische Analyse von Gao et al.

[11], die Spannungsrelaxation durch Diffusionskriechen verstärkt untersucht. Für Cu Schichten stimmten die experimentell gemessenen Spannungs-Temperatur-Kurven und deren Simulation überein [12]. Mikroskopische Untersuchungen zeigten auch, dass der vorgeschlagene Verformungsmechanismus zu gelten scheint: Material diffundiert entlang der Oberfläche in die Korngrenzen, sammelt sich dort, was einen inhomogenen Spannungszustand zur Folge hat, so dass schließlich Versetzungen auf Ebenen parallel zum Substrat von diesen Korngrenzen emittiert werden.

Die vorliegende Arbeit konzentriert sich auf das thermomechanische Verhalten dünner Au Schichten auf Si. Au eignet sich hervorragend als Modellsystem, um Eigenschaften zu untersuchen, die von der Oberflächendiffusion abhängen, wie z.B. eingeengtes Diffusionskriechen oder auch die Änderung der Oberflächenmorphologie, da es auch bei höheren Temperaturen nicht mit der umgebenden Atmosphäre reagiert, wie z.B. Cu oder Ag. Außerdem wurde dem Einfluss der Schichtmikrostruktur besondere Beachtung geschenkt, da es möglich war über einen breiten Schichtdickenbereich von 100 bis 850 nm zwei unterschiedliche thermisch stabile Mikrostrukturen bei einer Schichtdicke herzustellen.

7.2 Experimentelles

Au Schichten wurden mittels Magnetron-Sputtern im Ultrahochvakuum ($\leq 10^{-8}$ mbar) in einer kommerziellen Sputterkammer (DCA Instruments, Finnland) abgeschieden. Bei den Substraten handelte es sich um (100)-orientiertes Si mit einer 50 nm dicken SiO_x- und einer 50 nm dicken SiN_y-Zwischenschicht. Die Abscheiderate betrug 7 Å/s, wobei Proben bei einer Substrattemperatur von 300 °C und Raumtemperatur hergestellt wurden und somit zwei verschiedene Mikrostrukturen erzielt werden konnten. Im Gegensatz zu den Schichten, die bei 300 °C abgeschieden wurden, wurden die bei Raumtemperatur hergestellten Schichten in der Sputterkammer 30 min bei 500 °C ausgelagert, um die Mikrostruktur zu stabilisieren.

Die Charakterisierung der Mikrostruktur erfolgte mittels verschiedener Mikroskopietechniken. Im Transmissionselektronenmikroskop (TEM) wurden Querschnittsproben von ungefähr der Hälfte aller Schichten untersucht. Es wurde entweder ein JEOL 2000 FX oder ein JEOL 4000 EX benutzt. Hierbei galt es nicht nur die Mikrostruktur zu analysieren, sondern auch die tatsächliche Schichtdicke nachzumessen. Aufgrund dieser Messungen konnten die tatsächlichen Schichtdicken für

die restlichen Proben extrapoliert werden. Zur Korngrößenbestimmung wurden von den bei Raumtemperatur hergestellten Schichten zusätzlich TEM Durchsichtsproben hergestellt. Für Schichten dicker als ca. 100 nm, wurde das Au mit einem Argonionenstrahl gedünnt, um eine elektronentransparente Schicht zu erhalten. Es wurden Bilder unter verschiedenen Kippwinkeln aufgenommen, die Korngrenzen auf einer Transparentfolie nachgezeichnet und die Flächen mit einer kommerziellen Software (Quantimet Q500/W, Leica) ausgemessen.

Die Korngrößen der bei 300 °C abgeschiedenen Schichten konnten aus rasterelektronenmikroskopischen Aufnahmen in einem LEO VP. bestimmt werden. Die Korngrenzen wurden dabei ebenfalls auf einer Transparentfolie nachgezeichnet und ausgewertet. Des Weiteren wurde das Rasterelektronenmikroskop (REM) verwendet, um die Oberfläche vor und nach den thermischen Zyklen zu untersuchen. Von den sich gebildeten Hügeln wurden die Grundflächen bestimmt. Ein weiteres REM (CamScan SC44), das mit einem Heiztisch ausgestattet war, wurde benutzt um die Hügelbildung in einer 870 nm dicken Schicht direkt zu beobachten. Die Probe war dabei mit Leitsilber auf diesem Tisch angebracht und wurde manuell mit einer Heizrate zwischen 2 und 5 K/min zwischen Raumtemperatur und 500 °C zykliert. Eine weitere 870 nm dicke Au Schicht wurde ca. 210 min bei 420 °C ausgelagert und somit das zeitliche Wachstum der Hügel beobachtet.

Die Charakterisierung der Mikrostruktur der Hügel erfolgte im Rasterionenmikroskop (FIB) und im TEM. Der Ionenstrahl im FIB konnte dazu genutzt werden, Hügelquerschnitte zu erstellen und die Mikrostruktur abzubilden. Eine Querschnittsprobe für das TEM wurde außerdem im FIB präpariert. Die Textur der Schichten wurden über Polfiguren in einem Phillips Diffraktometer ermittelt. Die Schichten wurden zwischen Raumtemperatur und 500 °C mit Heizraten von 4-6 K/min thermisch zykliert und die Krümmung alle 10 °C laseroptisch gemessen [6, 90]. Die Krümmung der Probe ist umgekehrt proportional zur Spannung in der Schicht [91], so dass über die Krümmungsänderung der Probe die Spannungsänderung in der Schicht bestimmt werden kann. Zusätzlich wurde die Spannungsrelaxation bei 500 °C über mindestens 180 min für einige Schichten gemessen.

7.3 Ergebnisse und Diskussion

Im Folgenden werden die unterschiedlichen Mikrostrukturen, die Ergebnisse der Spannungstemperaturmessungen, die daraus resultierenden Spannungen bei Raumtemperatur und die Änderung der Oberflächenmorphologie abhängig von den thermischen Zyklen diskutiert.

7.3.1 Mikrostruktur

Sputtern bei unterschiedlichen Substrattemperaturen hatte verschiedene Mikrostrukturen zur Folge. Die Schichten, die bei 300 °C hergestellt wurden, hatten kolumnare Körner, wobei die Korngrößen ungefähr den Schichtdicken entsprachen. Letztere waren zwischen 86 und 847 nm. Die (111)-Fasertextur dieser Schichten war sehr breit und stieg von 10.9 auf 13.1° mit abnehmender Schichtdicke. Außerdem hatten die Schichten eine relativ hohe Rauhigkeit im Vergleich mit den bei Raumtemperatur hergestellten. Für die Schichten, die bei Raumtemperatur abgeschieden wurden, ergaben sich abhängig von den Schichtdicken zwei unterschiedliche Mikrostrukturen. Die Schichten zwischen 57 und 121 nm hatten ebenfalls kolumnare Körner mit Korngrößen, die ungefähr den Schichtdicken entsprachen. In den dickeren Schichten (173 bis 1738 nm) waren die Körner nicht komplett durchgängig, sondern es gab horizontale Korngrenzen. Außerdem waren die Körner mit 98 bis 181 nm sehr viel kleiner als die Schichtdicken. Die Breite der (111)-Fasertextur betrug unabhängig von der Schichtdicke 3.7°.

7.3.2 Spannungstemperaturmessungen

Die Spannungstemperaturkurven verliefen unterschiedlich für die verschiedenen Mikrostrukturen. Die nicht-kolumnaren Schichten (173 nm $\leq h_f \leq$ 1738 nm) zeigten den aus der Literatur für z.B. im UHV gesputterte Cu [4, 12] und Ag [39] Schichten bekannten Spannungstemperaturverlauf: Nach der Herstellung und Auslagerung waren die Schichten unter Zugspannung. Diese wurde gemäß einer thermoelastischen Gerade während des Aufheizens abgebaut. Zwischen 200 und 280 °C knickten die Kurve ab und es folgte ein Spannungsplateau bis die maximale Temperatur von 500 °C erreicht war. Beim Abkühlen wurde ebenfalls zuerst eine thermoelastische Gerade beobachtet, allerdings nur über einen Temperaturbereich von maximal 40 °C. Danach stieg die

Spannung sehr schwach mit abnehmender Temperatur. Zwischen 230 und 280 °C erfolgte dann der Übergang zu einem steileren Anstieg der Spannung.

Die dünneren Schichten ($h_f \leq 121$ nm), die bei Raumtemperatur hergestellt wurden, zeigten ein ähnliches Verhalten, nur dass bei höheren Temperaturen während des Aufheizens kein Spannungsplateau sondern ein kontinuierlicher Anstieg bis 500 °C beobachtet wurde. Das thermoelastische Entlasten erstreckte sich über einen größeren Temperaturbereich. Aufgrund dessen konnten beim weiteren Abkühlen die zwei unterschiedlichen plastischen Bereiche und vor allem die Übergangstemperatur zwischen ihnen nicht genau bestimmt werden.

Die bei 300 °C hergestellten Schichten hatten schließlich eine dritte Kurvenform: Während des Aufheizens war eine thermoelastische Gerade zu beobachten, auf die frühestens ab 180 °C ein Spannungsplateau folgte. Während des Abkühlens war jedoch kein thermoelastisches Verhalten zu erkennen, sondern sofort ein schwacher Anstieg der Spannung mit der Temperatur. Leung et al. [38] beobachtete diese Verhalten ebenfalls für Au-Schichten mit eine W-Zwischenschicht. Zwischen 200 und 270 °C erfolgte dann, wie für die nicht-kolumnaren Schichten, der Übergang zu einer größeren Steigung.

Der Übergang zwischen dem thermoelastischen und plastischen Bereich beim Aufheizen und den beiden plastischen Bereichen beim Abkühlen erfolgte jeweils unabhängig von der Mikrostruktur zwischen 180 und 280 °C. Dies ist der Temperaturbereich, in dem Korngrenzen- und Oberflächendiffusion ausreichend aktiviert sind. Der Bereich der Abkühlkurve mit der geringeren Steigung zeigt diffusionskontrollierte Verformung bei höheren Temperaturen. Im Bereich niedrigerer Temperaturen herrscht Versetzungsplastizität vor. Die Schichten, die bei 300 °C hergestellt wurden und die, die bei Raumtemperatur gesputtert wurden und dünner als 121 nm waren, erfüllten die Voraussetzungen für eingeengtes Diffusionskriechen, da sie eine freie Oberfläche und eine kolumnare Mikrostruktur hatten. Im TEM konnten erstmals parallele Gleitversetzungen in Au Schichten beobachtet werden. Sie sind eine unmittelbare Folge eingeengten Diffusionskriechens. Der Verlauf der Aufheizkurven konnte durch Modellieren beschrieben werden, wenn wie von Bühler et al. [33] für Cu vorgeschlagen eine Schwellspannung für das Einsetzen des Diffusionskriechens eingeführt wurde. Bei den Schichten, die bei Raumtemperatur hergestellt wurden, musste zusätzlich eine größere als die experimentell bestimmte Korngröße für die Simulation verwendet werden. Die Abkühlkurven konnten für die bei 300 °C hergestellten Schichten im

Gegensatz zu den bei Raumtemperatur hergestellten Proben nicht durch die Simulation wiedergegeben werden, da im Experiment keine thermoelastische Entlastung beobachtet wurde. An den Diskrepanzen zwischen Simulation und Experiment und an den Unterschieden zwischen den beiden Typen von kolumnaren Schichten, die bei verschiedenen Temperaturen hergestellt wurden, wird deutlich, dass außer der Mikrostruktur weitere Parameter einen Einfluss auf das Verhalten haben müssen. Es wurde vermutet, dass z.B. Texturbereite und die Rauhigkeit die Diffusion beeinflussen.

Der Vergleich mit Untersuchungen an Cu Schichten [4,25,87] zeigt, dass Au und Cu im ultra-dünnen Schichtdickenbereich unterhalb von 120 nm einen sehr ähnlichen Spannungstemperaturverlauf haben. Außerdem zeigen beide parallele Gleit-versetzungen, so dass darauf geschlossen werden kann, dass bei höheren Temperaturen eingeengtes Diffusionskriechen vorliegt.

Um die Verformung bei Raumtemperatur zu beschreiben, ist es sinnvoll, die Spannungen bei 50 °C als Funktion der reziproken Schichtdicken zu betrachten. Abb. 7.1 zeigt die Spannungen aller Schichten zusammen mit den gängigen Modellen der Dünnschichtmechanik; dem Nix-Modell [8], dem Thompson-Modell [9] für Korngrößen von 100 und 200 nm und dem Quellenmodell [101].

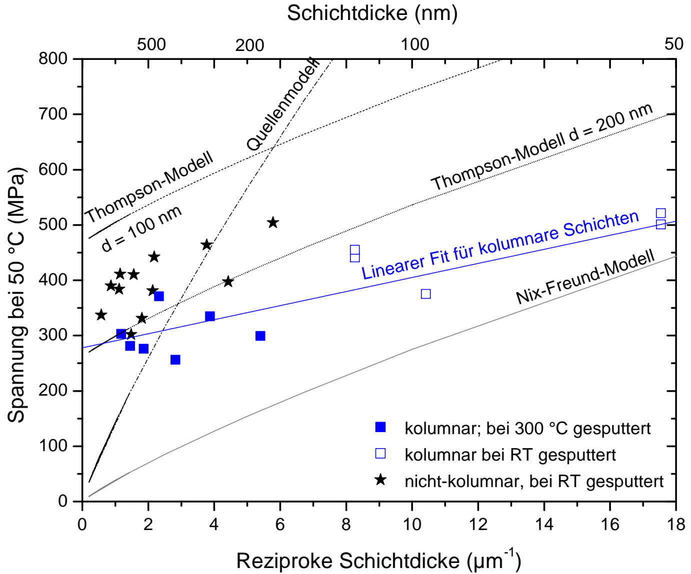

Abb. 7.1: Die Spannungen aller Schichten bei 50 °C nach thermischen Zyklen. Die Sterne sind die nicht-kolumnaren Schichten, die bei Raumtemperatur hergestellt wurden. Die bei 300 °C hergestellten, kolumnaren Schichten (Quadrate) und die bei Raumtemperatur gesputterten kolumnaren Schichten liegen auf einer Gerade. Außerdem ist das Nix-Modell und das Thompson-Modell für eine Korngröße von 100 und 200 nm eingezeichnet.

In dieser Untersuchung wurden erstmals Spannungswerte für Au in kleinen Dimensionen unterhalb von 100 nm gemessen. Wie erwartet, hatten bei gleicher Schichtdicke die Schichten mit kleineren Körnern höhere Spannungen. Die kleinste Dimension ist somit festigkeitsbestimmend. Wenn die Spannungen gegen die reziproke Korngröße aufgetragen wurden, lagen alle Proben auf einer Gerade. Dies ist bemerkenswert, da sich die Umgebung der Körner in nicht-kolumnaren und kolumnaren Schichten unterscheidet. Offensichtlich scheinen aber weniger Grenzflächen und Oberflächen als eher die Dimension an sich einen Einfluss auf die Versetzungsbewegung zu haben. Des Weiteren ist in Abb. 7.1 deutlich zu sehen, dass die Spannungswerte der nicht-kolumnaren Schichten zwischen den vom Thompson-Modell vorhergesagten Werten lagen.

Der Vergleich mit Daten für Au aus der Literatur zeigte ähnliche Werte für all Proben, unabhängig von der Untersuchungsmethode und der Probengeometrie. Für die

Proben dieser Untersuchung war jedoch nur eine relativ schwache Abhängigkeit von der Dimension über den gesamten untersuchten Bereich (57 bis 847 nm) zu beobachten. Für die meisten anderen Proben aus der Literatur begann diese schwache Abhängigkeit allerdings erst unterhalb von 500 nm.

7.3.3 Oberflächenenmorphologie

Thermisches Zyklieren hatte eine deutliche Veränderung der Oberfläche zur Folge. Es bildeten sich Korngrenzenfurchen, Poren und Hügel, wobei Korngrenzenfurchen und Poren an Tripelpunkten und entlang Korngrenzen bei allen Schichten zu beobachten waren. Alle nicht-kolumnaren Schichten, d.h. die Schichten, die bei Raumtemperatur gesputtert wurden und dicker als 173 nm waren und die zwei dicksten bei 300 °C gesputterten Schichten, zeigten zusätzlich Hügel. Abb. 7.2. zeigt den Querschnitt durch einen solchen Hügel nach sieben Zyklen in einer 1154 nm dicken Au-Schicht. Der Hügel ist nicht einkristallin, sondern besteht aus mehreren Körnern, die wesentlich größer sind als die Körner der umgebenden Schichtmatrix.

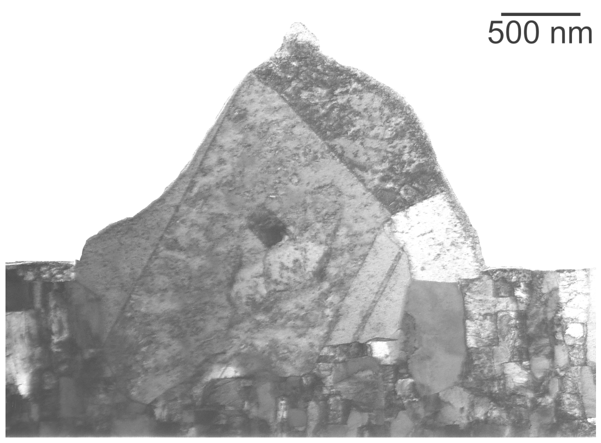

Abb. 7.2: TEM-Querschnittsprobe eines Hügels in einer 1154 nm dicken Au Schicht nach sieben thermischen Zyklen. Der Hügel besteht aus mehreren Körnern, die wesentlich größer sind als die der umgebenden Schichtmatrix.

Durch Vergleich der makroskopisch gemessenen Spannungstemperaturkurven und der direkten Beobachtung der Hügelbildung in in-situ Heizexperimenten im REM, konnte gezeigt werden, dass Diffusion aufgrund der hohen Temperaturen aktiv war, und dass die Schichten unter einer Druckspannung standen als die Hügelbildung einsetzte. Die Druckspannungen, die durch das Material in den Hügeln relaxiert wurden, konnten aus den Hügelgrundflächen und den Hügeldichten abgeschätzt werden. Das Volumen

der Hügel wurde dabei als Mittelwert zwischen einer Halbkugel und einem Kegel angenommen. Verglichen mit der makroskopischen Spannungsrelaxation waren die so relaxierten Spannungen für alle Schichtdicken niedriger. Bei der Spannungsrelaxation durch Hügelbildung handelte es sich daher um einen Mechanismus zur lokalen Spannungsrelaxation. Es konnte auch gezeigt werden, dass die Relaxation der Druckspannung bei den vorliegenden Hügeldichten immer größer ist als der Energieeintrag ins System durch die Schaffung der zusätzlichen Oberflächen der Hügel.

Aus dem Vergleich von kolumnaren und nicht-kolumnaren Schichten bei gleicher Schichtdicke, und dass sie bei höheren Temperaturen ähnlichen Druckspannungen aufwiesen, konnte geschlossen werden, dass die ungewöhnliche Mikrostruktur der nicht-kolumnaren Schichten eine wesentliche Voraussetzung für die Hügelbildung war, da kolumnare Schichten keine Hügel bildeten. Die horizontalen Korngrenzen sind ausschlaggebend. Sie bilden ein Netzwerk schneller Diffusionspfade, entlang denen das Material innerhalb der Schichtebene diffundiert und dann über eine vertikale Korngrenze mit einer hohen Diffusivität an die Oberfläche gelangt. Wenn dort eine ausreichende Flussdivergenz gegeben ist, bildet sich ein Hügel.

7.4 Schlussfolgerung

Die vorliegende Arbeit hat gezeigt, dass in dünnen Au Schichten während des thermischen Zyklierens verschiedene Verformungsmechanismen auftreten können. Diffusion spielt dabei bei höheren und Versetzungsgleiten bei niedrigeren Temperaturen eine wesentliche Rolle. Bei der Versetzungsbewegung bei Raumtemperatur war die kleinste Dimension festigkeitsbestimmend. Im Fall der nicht-kolumnaren Schichten war dies die Schichtdicke und bei den kolumnaren Schichten entsprachen sich Schichtdicke und Korngröße ungefähr. Es konnte argumentiert werden, dass in erster Linie die Korndimension und nicht die Umgebung, z.B. die Grenzflächen des Korns, ausschlaggebend sind für die Spannung. Durch die freie Oberfläche und die kolumnare Mikrostruktur war in einem Teil der Schichten, die Vorraussetzungen für eingeengtes Diffusionskriechen gegeben und es konnten auch zum ersten Mal parallele Gleit-versetzungen in Au beobachtet werden. Die nicht-kolumnaren Schichten relaxierten die Spannungen bei hohen Temperaturen ebenfalls über Diffusionskriechen. Zusätzlich bildeten sie jedoch, aufgrund der Mikrostruktur mit horizontalen Korngrenzen als weit reichende Diffusionspfade, Hügel um Druckspannungen lokal abzubauen.

8 References

[1] Spearing SM. Acta mater. 2000;48:179.

[2] Arzt E. Acta mater. 1998;46:5611.

[3] Raiteri R, Grattarola M, Butt H-J, Skladal P. Sensors and Actuators B 2001;79.

[4] Balk TJ, Dehm G, Arzt E. Acta mater. 2003;51:4471.

[5] Dehm G, Balk TJ, Edongué H, Arzt E. Microelectron. Eng. 2003;70:412.

[6] Keller R, Baker SP, Arzt E. J. Mater. Res. 1998;13:1307.

[7] Venkatraman R, Bravman JC. J. Mater. Res. 1992;7:2040.

[8] Nix WD. Metall. Trans. A 1989;20A:2217.

[9] Thompson CV. Scripta metall. mater. 1993;28:167.

[10] von Blanckenhagen B, Gumbsch P, Arzt E. Phil. Mag. Lett. 2003;83:1.

[11] Gao H, Zhang L, Nix WD, Thompson CV, Arzt E. Acta mater. 1999;47:2865.

[12] Weiss D, Gao H, Arzt E. Acta mater. 2001;49:2395.

[13] Kraft O, Freund LB, Phillips R, Arzt E. MRS Bulletin 2002;27:30.

[14] Baker SP. Mater. Sci. Eng., A 2001;A319-321:16.

[15] Freund LB. J. Appl. Mech - Trans ASME 1987;54:553.

[16] Endongue H. Dünnschichtplastizität und Wechselwirkung von Gitterversetzungen mit der Film/Substrat Grenzfläche, Institut für Metallkunde, Universität Stuttgart, 2004.

[17] Dehm G, Wagner T, Balk TJ, Arzt E. J. Mater. Sci. Technol. 2002;18:113.

[18] Inkson BJ, Dehm G, Wagner T. Acta mater. 2002;50:5033.

[19] Dehm G, Arzt E. Appl. Phys. Lett. 2000;77:1126.

[20] Thompson CV. J. Mater. Res. 1993;8:237.

[21] Nix WD. Scripta mater. 1998;39:545.

[22] Schwarz KW, Tersoff J. Appl. Phys. Lett. 1996;69:1220.

[23] Pant P, Schwarz KW, Baker SP. Acta mater. 2003;51:3243.

[24] von Blanckenhagen B. Versetzungen in dünnen Metallschichten, Institut für Metallkunde, Universität Stuttgart, 2002. p.89.

[25] Dehm G, Balk TJ, von Blanckenhagen B, Gumbsch P, Arzt E. Z. Metallkd. 2002;93:383.

[26] Coble RL. J. Appl. Phys. 1963;34:679.

[27] Thouless MD, Gupta J, Harper JME. J. Mater. Res. 1993;8:1845.

[28] Genin FY. J. Appl. Phys. 1995;77:5130.

[29] Genin FY. Acta metall. mater. 1995;43:4289.

[30] Xia ZC, Hutchinson JW. Crack patterns in thin films. J. Mech. Phys. Solids 2000;48:1107.

[31] Reprinted from Acta Mater. 49, Weiss D, Gao H, Arzt E, Constrained diffusional creep in UHV Cu thin films, pp. 2395, Copyright 2001, with permission form Elsevier.

[32] Böhm J, Gruber P, Spolenak R, Wanner A, Arzt E. In: Anderson PM, Foecke T, Misra A, Rudd RE, editors. Mat. Res. Soc. Symp. Proc. 821, Warrendale, PA. Nanoscale Materials and Modeling-Relations Among Processing, Microstructure and Mechanical Properties. 2004; p. P1.6.1.

[33] Buehler MJ, Hartmaier A, Gao H.. In: Anderson PM, Foecke T, Misra A, Rudd RE, editors, Mater. Res. Soc. Symp. Proc. 821, Warrendale, PA. Nanoscale Materials and Modeling-Relations Among Processing, Microstructure and Mechanical Properties 2004; P1.2.1

[34] Arzt E, Dehm G, Gumbsch P, Kraft O, Weiss D. Prog. Mat. Sci. 2001;46:283.

[35] Leung OS, Nix WD. In: Vinci R, Kraft O, Moody N, Besser P, Shaffer E, editors. Mater. Res. Soc. Symp. Proc. 594, Warrendale, PA. Thin Films - Stresses and Mechanical Properties VIII. 2000; p.51.

[36] Mullins WW. J. Appl. Phys. 1957;28:333.

[37] Mullins WW. Acta metall. 1958; 6:414.

[38] Leung OS, Munkholm A, Brennan S, Nix WD. J. Appl. Phys. 2000;88:1389.

[39] Kobrinsky MJ, Thompson CV. Appl. Phys. Lett. 1998;73:2429.

[40] Chaudhari P. J. Appl. Phys. 1974;45:4339.

[41] Jackson MS, Li C-Y. Acta metall. 1982;30:1993.

[42] Kim DK, Nix WD, Deal MD, Plummer JD. J. Mater. Res. 2000;15:1709.

[43] Kim DK, Nix WD, Vinci RP, Deal MD, Plummer JD. J. Appl. Phys. 2001;90:781.

[44] Ericson F, Kristensen N, Schweitz J-A. J. Vac. Sci. Tech. B 1991;9:58.

[45] Muppidi T, Kusama Y, Field DP. vol. 721: Mat. Res. Soc. Symp. Proc. Vol., 2002. p.J4.10.1.

[46] Smith U, Kristensen N, Ericson F, Schweitz J-A. J. Vac. Sci. Tech. A 1991;9:2527.

[47] Hwang S-J, Lee Y-D, Park Y-B, Lee J-H, Jeong C-O, Joo Y-C. Scripta mater. 2006;54:1841.

[48] Genin FY. Interface science 2001;9:83.

[49] Nucci JA, Keller RR, Field DP, Shacham-Diamand Y. Appl. Phys. Lett. 1997;70:1242.

[50] Weiss D, Deformation mechanisms in pure and alloyed copper films, Institut für Metallkunde, Universität Stuttgart, 2000. p.157.

[51] Park H, Hwang S-J, Joo Y-C. Acta mater. 2004;52:2435.

[52] Lahiri SK. J. Appl. Phys. 1970;41:3172.

[53] Kim DK, Heiland B, Nix WD, Arzt E, Deal MD, Plummer JD. Thin Solid Films 2000;371:278.

[54] Pennebaker WB. J. Appl. Phys. 1969;40:394.

[55] Iwamura E, Ohnishi T, Yoshikawa K. Thin Solid Films 1995;270:450.

[56] Lilleodden ET, Nix WD. Acta mater. 2006;54:1583.

[57] Legros M, Dehm G, Balk TJ, Arzt E, Bostrom JR, Gergaud P, Thomas O, Kaouache B. In: Zbib HM, Lassila DH, Levine LE, Hemker KJ, editors. Mater. Res. Soc. Symp. Proc. 779, Warrendale, PA. Multiscale Phenomena in Materials--Experiments and Modeling Related to Mechanical Behavior 2003; p. W4.2.1.

[58] Owusu-Boahen K, King AH. Acta mater. 2001;49:237.

[59] Reused with permission from O. S. Leung, A. Munkholm, S. Brennan, and W. D. Nix, Journal of Applied Physics, 88, 1389 (2000). Copyright 2000, American Institute of Physics.

[60] Emery RD, Povirk GL. Acta mater. 2003;51:2067.

[61] Emery RD, Povirk GL. Acta mater. 2003;51:2079.

[62] Haque MA, Saif TA. Proc. Natl. Acad. Sci. U.S.A. 2004;101:6335.

[63] Espinosa HD, Prorok BC, Peng B. J. Mech. Phys. Solids 2004;52:667.

[64] Uchic MD, Dimiduk DM, Florando JN, Nix WD. Science 2004;305:986.

[65] Greer JR, Oliver WC, Nix WD. Acta mater. 2005;53:1821.

[66] Greer JR, Oliver WC, Nix WD. Acta mater. 2006;54:1705.

[67] Volkert CA, Lilleodden ET. Phil. Mag. 2006;in press.

[68] Hieber H. Thin Solid Films 1976;37:335.

[69] Kim JY, Hummel RE. Phys. Satus Solidi A 1990;122:255.

[70] Miller DC, Herrmann CF, Maier HJ, George SM, Stoldt CR, Gall K. Scripta mater. 2005;52:873.

[71] Cottrell AH. Dislocations and plastic flow in crystals. Oxford: Clarendon Press, 1965.

[72] Greer JR, Nix WD. Appl. Phys. A 2005;80:1625.

[73] Petch NJ. Ion Steel Inst. 1953;174:25.

[74] Hall EO. Proc. Roy. Soc. Lon. 1951;B64:747.

[75] Meyers MA, Mishra A, Bension DJ. Prog. Mat. Sci. 2006;51:427.

[76] Vinci RP, Zielinski EM, Bravman JC. Thin Solid Films 1995;262:142.

[77] Wellner P, Dehm G, Kraft O, Arzt E. Z. Metallkd. 2004;95:769.

[78] Buehler MJ, Hartmaier A, Gao H. Modelling & Simulation in Materials Science & Engineering 2004;12.

[79] Chang YA, Himmel L. J. Appl. Phys. 1966;37:3567.

[80] Adams JH. Metals handbook. Properties and selection: non-ferrous alloys and special-purpose materials. Cleveland, Ohio: ASM International, 1990. p.1154.

[81] Krishanan RS, Srinivasan R, Devanarayanan S. Thermal Expansion of Crystals. In: Pamplin BR, editor. International Series in the Science of the Solid State, vol. 12. Oxford: Pergamon Press, 1979. p.118.

[82] Mehrer H, editor Group III: Crystal and Solid State Physics, Diffufion in Solid Metals and Alloys, 1990.

[83] Kobrinsky MJ, Thompson CV. Acta mater. 2000;48:625.

[84] Kobrinsky MJ, Dehm G, Thompson CV, Arzt E. Acta mater. 2001;49:3597.

[85] Leung OS. Studies on the strengthening mechanisms of thin polycrystalline gold films, Dissertation. Stanford University, 2001. p.94.

[86] Gibbs GB. Phil. Mag. 1966;13.

[87] Balk TJ. unpublished results.

[88] Sharma SK, Spitz J. Thin Solid Films 1980;65:339.

[89] Presland AEB, Price GL, Trimm DL. Surface Science 1972;29:424.

[90] Flinn PA, Gardner DS, Nix WD. IEEE Trans. Electr. Dev. 1987;ED-34:689.

[91] Stoney GG. Proc. Roy. Soc. 1909;A82:172.

[92] Spolenak R, Heiland B, Witt C, Keller R-M, Müllner P, Arzt E. Prakt. Metallogr. 2000;37:90.

[93] Shapiro SS, Wilk MB. Biometrika 1965;52:591.

[94] Gottstein G. Physikalische Grundlagen der Materialkunde. Berlin Heidelberg: Springer Verlag, 1998.

[95] Kaur I, Gust W. Handbool of Grain and Interphase Bounday Diffusion Data. Stuttgart: Ziegler Press, 1989.

[96] Gontier-Moya EG, Beszeda I, Moya F. Surface Science 2004;566-568:148.

[97] Spolenak R, Brown WL, Tamura N, MacDowell AA, Celestre RS, Padmore HA, Valek B, Bravman JC, Marieb T, Fujimoto H, Batterman BW, Patel JR. Phys. Rev. Lett. 2003;90:096102/1.

[98] Phillips MA, Spolenak R, Tamura N, Brown WL, MacDowell AA, Celestre RS, Padmore HA, Batterman BW, Arzt E, Patel JR. Microelectron. Eng. 2004;75:117.

[99] Nucci JA, Kramer S, Arzt E, Volkert CA. J. Mater. Res. 2005;20:1851.

[100] Miedema AR. Z. Metallkd. 1978;69:287.

[101] von Blanckenhagen B, Arzt E, Gumbsch P. Acta mater. 2004;52:773.